Origami- and Kirigami-Adapted Thick-Panel Folding

Jingyi Yang

Wolfson College

A dissertation submitted for the degree of Doctor of Philosophy

in the Department of Engineering Science

at University of Oxford

Trinity Term, 2022

To my family.

ABSTRACT

Origami- and Kirigami-Adapted Thick-Panel Folding

Jingyi Yang, Wolfson College

A thesis submitted for the degree of Doctor of Philosophy in the Department of Engineering Science, University of Oxford. Trinity Term, 2022.

This dissertation is concerned with folding rigid panels of uniform thickness into a compact volume and deploying it back to a continuous and flat surface in a predictable manner afterwards. This was achieved by either forming an assembly with a single degree-of-freedom (DoF) through special geometric designs of thick-panel kirigami or ensuring a collision-free deployment of a multiple-DoFs system through dynamics simulations. Four major findings of this dissertation were as follows.

First, kirigami patterns were investigated to enable the folding of a chessboard-like array with identical panels into two stacks without any voids. Revolute joints (also known as hinges or rotational joints) and slits are placed to connect or disconnect panels according to a Hamiltonian circuit (HC) (Hamilton, 1856) that was drawn over the array. If multiple HCs were found, a method was proposed to select the ones that could be folded into two stacks. Physical prototypes were made to validate the designs.

Secondly, simple spring-loaded hinges were used to synchronise the deployment of a multiple-DoF assembly resulting from the HC approach. An optimisation method was proposed to select the stiffness of hinges to ensure a collision-free deployment. Dynamic simulation of the deployment and collision detection method were incorporated into the optimisation process. By this approach, the trajectories of panels were sequenced to avoid collisions during the deployment, and the array was always deployed to a flat surface from packaged stacks, which were further validated by experiments.

Thirdly, through special geometric designs, interlinked regular flat rigid panels of uniform thickness were folded into compact stacks with a single DoF. Kinematically the deployable structure is an assembly of several 8R closed chains. Although such a chain with eight rigid bodies and eight revolute joints would have two DoFs in general, a single-DoF assembly was created by combining them in a particular way. The bi-directional folding concept can be extended to fold an assembly consisting of an infinite number of panels. Not only can this work be directly applied to the design of future flat arrays, but is also important in the theory of mechanisms as the proposed assemblies are rare examples where a kinematic loop consisting of linkages of multiple DoFs possesses single mobility.

Finally, a modular approach was proposed to fold arrays composing squares or the combination of squares and half-square triangles into a compact volume that is conforming to the shape of a CubeSat. The obtained arrays could possess a single DoF or a small number of DoFs.

Keywords: thick-panel kirigami, compact folding, uniform thickness, Hamiltonian circuit, spring-loaded hinges, collision-free deployment, single-DoF assembly of 8Rs.

ACKNOWLEDGEMENTS

This thesis would not be possible without the ongoing personal and professional support from my family, friends, colleagues, and the financial support from National Science Scholarship, A*STAR, Singapore.

First and foremost, I would like to express my sincere gratitude to my supervisor, Professor Zhong You, who introduced me to the field of origami and deployable structures. I have benefited enormously not only from his unique views but also from his sharp observations of daily life, which inspired me and led my work into exciting fields. My special appreciation goes to my collaborator Professor Manolis. N. Chatzis, who shared his broad knowledge in dynamics with me without any reservation; Professor Yan Chen and Dr Xiao Zhang, who helped me greatly with the kinematics analysis of spatial linkages.

I would like to thank the members of my dissertation committee, Professor Larry Howell and Professor Chris Martin for giving me an intellectually stimulating and enjoyable viva. Their valuable edits and comments improved the presentation of this thesis.

My thanks also go to Professor Sinan Acikgoz, for the intriguing questions he raised and the discussions we had during my transfer of status at Oxford; to Professor Clive Siviour and Thomas Commins, for borrowing their high-speed camera and helping me with the settings; to Dr Peter Walters, Clive Baker, Cleveland Williams, Duncan Constable, for their help in manufacturing the test specimens; and also to my peers and graduates from the department of engineering science, especially to Dr Yang Li, Dr Yunfang Yang, Dr Yunlan Zhang, Dr Mateusz Portka, Leo De Waal, David Xing and Chenying Liu from the special structures group, for their ideas and discussions.

I appreciate deeply the companionship of my boyfriend Hong-Po Hsieh, my friend Xiaotian Yu, my fellow college mates, and my bandmates. The time that we spent together, travelling, chatting, playing music, and drinking, without which I might have finished this thesis half a year in advance, but I could never experience such a fantastic life of now.

Last but not least, I am grateful for the unconditional love and support from my family, making me the happiest kid in this world. Mom and dad, I love you.

CONTENTS

LIST OF FIGURES

LIST OF TABLES

NOMENCLATURE

a	The thickness of a panel
$a_1, a_2, \ldots,$ $b_1, b_2, \ldots$	Revolute joints that are connecting panels in 8R element A or B
$a_{i(i+1)}$	Link length between joint i and joint i+1
$\mathbf{a}_i$	Linear accelerations of the origin of frame $\{i\}$ with respect to its frame
$\mathbf{a}_i^0$	Linear acceleration of frame $\{i\}$ expressed in frame $\{0\}$
c_a	Tested damping coefficient of the elastic hinge with spring stiffness k_a
c_c	Critical damping coefficient of the mass-spring system
c_{ch}	Damping coefficient at the cut hinge
c_i	Damping coefficient of the spring at hinge h_i
c_s	Damping coefficient to model the contact at the side facets of the panels
d	The equal side length of an isosceles triangle
d_c	Distance between the block and the carriage for measuring spring stiffness
d_p	The smallest proximal distance of panel pairs throughout a simulation
d_i	The offset of joint i
e_j, e_j^-, e_j^+	An edge in an array of polygons
$\mathbf{e}_s$	A vector collecting of non-zero elements of the error matrix $\bar{\mathbf{E}}_s$
f	The vibrational frequency of the mass-spring system.
f_i	Degree-of-freedom of joint i
$f(K)$	The objective function in terms of spring stiffnesses K
$\mathbf{f}_M, \mathbf{f}_N$	Force at the cut hinge MN
h_i	A hinge in an array

$\{i\}$	A body-attached frame on panel i
j	Number of joints of an assembly
$\vec{k}$	A vector of the axis of rotation along hinge h_i, expressed in frame $\{i-1\}$
k_a, k_b	Measured stiffnesses of torsional springs
k_{ch}	Translational spring stiffness at the cut hinge
k_i	Torsional spring stiffness at hinge h_i
k_s	Spring stiffness to model the contact at the side facets of the panels
m_i	Mass of panel i
n, n_r, n_c	Number of links
p	Slit distance of an 8R element in skew-symmetric motion
$\mathbf{p}$	The displacement mode that leads to a finite mechanism of unit II
$\mathbf{p}_i^0$	Translation vector between the origin of body-attached frames $\{i\}$ and $\{0\}$
$\mathbf{p}_{hi}^0$	A vector from the fixed frame$\{0\}$ to the mid-point of the rotational hinge h_i
r_s, $r_{n,s}$	Rank of matrices
$\mathbf{r}_{i-1,\,hi}$	A vector from the origin of the body-attached frame $\{i-1\}$ to the mid-point of h_i, expressed in frame $\{0\}$
$\mathbf{r}_{i-1,\,hi}^{i-1}$	A vector from the origin of the body-attached frame $\{i-1\}$ to the mid-point of h_i, expressed in its frame
s	A predictor step in the numerical kinematic analysis for the 8R element
t_j, t_J	A time instance in a dynamic simulation
u, w	Point in the convex polytopes U and W
$\mathbf{u}_{1s}$, $\mathbf{u}_{2s}$, …,$\mathbf{u}_{12s}$	Left singular vectors of Jacobian matrix $\mathbf{M}_s$
$\mathbf{u}_{n,1s}$, $\mathbf{u}_{n,2s}$, …,$\mathbf{u}_{n,12s}$	Left singular vectors of Jacobian matrix $\mathbf{N}_s$
$v_{n,is}$	The diagonal entry on the i^{th} column and i^{th} row of $\mathbf{V}_{n,s}$

$\mathbf{v}_{diag}$	A vector collecting all the diagonal entries of $\mathbf{V}_{II}$
v_a	The largest approaching speed between two panels in a simulation
$\mathbf{w}_{1s}$, $\mathbf{w}_{2s}$, …, $\mathbf{w}_{8s}$	Right singular vectors of Jacobian matrix $\mathbf{M}_s$
$\mathbf{w}_{n,1s}$, $\mathbf{w}_{n,2s}$, …,$\mathbf{w}_{n,8s}$	Right singular vectors of Jacobian matrix $\mathbf{N}_s$
x_i, y_i, z_i	x, y, z axes of coordinate system $\{i\}$
$\mathbf{A}$	The adjacency matrix of a grid graph
A, B, C, D, F, G, H	8R elements
A_1, A_2,…, B_1, B_2, …	Panels in 8R element A or B
$\mathbf{C}_{1s}$, $\mathbf{C}_{2s}$, …, $\mathbf{C}_{8s}$	Constant matrices at step s
$\mathbf{D}$	A dataset of proximal distances at every time instance
$\mathbf{D}_j$, $\mathbf{D}_J$	The proximal distance of panel pairs
E	A collection of all the edges in a topological graph
$\bar{\mathbf{E}}_s$	Error matrix at step s
$\mathcal{G}$	Undirected grid graph
I_i	Moment of inertia of panel i with respect to its body-attached frame $\{i\}$
I_m	Moment of inertia of the aluminium mass block rotating about the hinges
J	The time step of the first collision in a dynamic simulation
$\mathbf{I}_4$	A 4×4 identity matrix
K	An array of spring stiffnesses at all hinges
$L_{1,1}$, $L_{1,2}$, …	A link in a rectangular array

$\mathbf{M}_s$, $\mathbf{M}_s^{\mathrm{II}}$	Jacobian matrices at step s
$\mathbf{N}_s$	Jacobian matrix of the higher8R element at step s
$P_1, P_2, \ldots, P_n$	Panels or polygons in an array
$\mathbf{R}_i^{i-1}$	A 3×3 rotation matrix from the body-attached frame $\{i-1\}$ to $\{i\}$, expressed in frame $\{i-1\}$
$\mathbf{T}_{i(i+1)}$	A 4×4 transformation matrix between coordinate systems at joint i and $i+1$
$\mathbf{T}_{21,s}$, $\mathbf{T}_{32,s}$, … $\bar{\mathbf{T}}_{21,s+1}$, $\bar{\mathbf{T}}_{32,s+1}$	Transformation matrix between coordinate systems
$\mathbf{T}'_{21,s}$, $\mathbf{T}'_{32,s}$,…	Derivative of transformation matrices at step s
S	The total number of time steps in a dynamic simulation
U, W	Convex polytopes
$\mathbf{U}_s$, $\mathbf{U}_{n,s}$, $\mathbf{U}_{\mathrm{II}}$	Collection of left singular vectors
V	A collection of all the vertices in a topological graph
$\mathbf{V}_J$	Approaching speed of all panel pairs except the connected ones at t_J
$\mathbf{V}_s$, $\mathbf{V}_{n,s}$, $\mathbf{V}_{\mathrm{II}}$	A rectangular matrix of singular values on its diagonal
$\mathbf{W}_s$, $\mathbf{W}_{n,s}$, $\mathbf{W}_{\mathrm{II}}$	Collection of right singular vectors
$\mathbf{W}_4$	The last four columns of $\mathbf{W}_{\mathrm{II}}$
α	The base angle of an isosceles triangle
$\alpha_{i(i+1)}$	Twist angle from axes z_i to z_{i+1} positively about x_{i+1}
$\boldsymbol{\alpha}_i$	Angular accelerations of the origin of frame $\{i\}$ with respect to its frame
$\Delta\mathbf{p}_{\mathrm{MM}'}$	A translation vector between frames {M} and {M'} at the cut hinge
$\Delta\dot{\mathbf{p}}_{\mathrm{MM}'}$	The time rate of change of $\Delta\mathbf{p}_{\mathrm{MM}'}$
$\Delta\theta_{1s}$, $\Delta\theta_{2s}$, …, $\Delta\theta_{8s}$	Small-angle increment of each revolute joint at step s

$\Delta\boldsymbol{\theta}_s,\ \Delta\boldsymbol{\theta}_s^{\mathrm{II}}$	A vector collecting all the small-angle increments at step s
$\Delta\theta_1^*, \Delta\theta_2^*, ...$	The angle corrections of the revolute joint
$\Delta\boldsymbol{\theta}_s^*$	The collection of angle corrections
φ_i	The dihedral angle between adjacent facets with a common axis z_i
φ_{ai}, φ_{bi}, φ_{ci}, φ_{di}	Dihedral angles in 8R elements A, B, C, D
$\mathcal{G}$	Topological graph
ζ	The damping ratio of the mass-spring system
ϑ_i	The angle of rotation of the hinge h_i
$\dot{\vartheta}_i$	Angular velocity induced by the rotation of hinge h_i
$\ddot{\vartheta}_i$	Angular acceleration induced by the rotation of hinge h_i
θ_i	The kinematic variable of joint i
θ_{1t}, θ_{2t}	Target configurations of the input angles θ_1 and θ_2
$\boldsymbol{\theta}_t$	A target configuration of the input angles for 8R element
θ_{1s}, θ_{2s}, ...	Kinematic variables of revolute joints at incremental step s
$\boldsymbol{\theta}_s$	A vector collecting the kinematic variables of the 8R element at step s
$\bar{\boldsymbol{\theta}}_{s+1}$	Kinematic variables at step s+1 before the corrector step
$\boldsymbol{\omega}_i$	Angular velocity of frame $\{i\}$ expressed in frame $\{i\}$
$\boldsymbol{\omega}_i^0$	Angular velocity of frame $\{i\}$ expressed in frame $\{0\}$
$\dot{\boldsymbol{\omega}}_i^0$	Angular acceleration of frame $\{i\}$ with respect to frame $\{0\}$
ω_n	Natural frequencies of the mass-spring system
τ_i	The magnitude of torque at hinge h_i due to the torsional spring
$\tau_i(\dot{\theta})$	The magnitude of torque resulting from viscous damping along h_i

$\mathbf{v}_i^0$	Linear velocity of frame $\{i\}$ expressed in frame $\{0\}$
$\sum \mathbf{f}^i$	Total force applied on the panel i expressed in frame $\{i\}$
$\sum \boldsymbol{\tau}^i$	Total torque applied on the panel i expressed in frame $\{i\}$

CHAPTER 1

INTRODUCTION

1.1 Folding and deployment of flat arrays

Flat arrays with a finite thickness are widely used in aerospace applications such as solar panels and reflectarray antennas. They need to be compactly packaged into small volumes for launch and subsequently deployed to flat surfaces once in the orbit. The most common mechanism to fold and deploy rigid panels is unidirectional. Hinges are placed on the top and bottom surfaces of solar panels consecutively to form z-folds (alternatively known as zigzag or accordion folds) (Schenk et al., 2014). It is designed for simplicity and high packaging efficiency. However, a limited number of panels can be connected because the panels extend to form a long cantilever beam in the deployed state, making it rather flexible when the number of panels is large. Moreover, a synchronising mechanism needs to be incorporated because it is not a single degree-of-freedom (DoF) system. If more panels are required to span a larger area, engineers could either append several deployable arrays that are independent of each other structurally (Blackwell et al., 2012; Dawson et al., 2012) or opt for a single deployable array with bi-directional deployment features.

Most bi-directional folding concepts can trace their origin to origami because of its advantage in transforming large thin sheets into compact volumes. Some origami folding patterns that have been adapted to fold flat aerospace structures (Morgan et al., 2016) include the Miura-ori (Nishiyama, 2012), the coiling mechanism (Arya et al., 2015) and the wrapping mechanism (Guest & Pellegrino, 1992). They offer a large deployment ratio with single mobility. However, these origami concepts are only directly applicable to thin panels of negligible thickness. For rigid panels of finite thickness, which is the case for most solar arrays and reflectarray antennas, various amendments must be made (Lang et al., 2018).

Several techniques can be adopted to fold thick panels, including the offset panel technique (Edmondson et al., 2015), the double hinged technique (Ku & Demaine, 2016), the rolling contacts joints (Lang et al., 2016), and the membrane technique (Zirbel et al., 2013), etc. The thickness of panels is accommodated in the folding process. However, these techniques yield either protruding hinge housings in the deployed state or inevitable voids amongst panels and along the hinges in the fully folded package. A structurally simpler approach that involves placing the revolute joints on either top or bottom surface of thick panels was proposed, which is known as the hinge shift technique (Hoberman, 2010). However, only origami patterns containing a distribution of symmetric vertices, e.g., the bird's foot vertex, were accommodated (Hoberman, 1988). A more general approach, referred to as the thick-panel origami, was proposed recently (Chen et al., 2015; Wang et al., 2018) where the vertices in a pattern need not be completely symmetric. Only revolute joints mounted on the surface of panels are used. Kinematically the thick-panel origami are a combination of 4R, 5R, or 6R overconstrained spatial linkages, where a 4R/ 5R/ 6R spatial linkage has four/ five/ six revolute joints that are arranged neither in parallel nor concurrent. The carefully planned tessellations of mechanisms ensure that the resulting assemblies have a single DoF. Despite its advantage in terms of motion control, the assemblies obtained using this approach do not naturally end up with a compactly

folded state that has no voids. Moreover, the deployed surface may not have a completely flat profile due to the necessary variation of panel thickness dictated by kinematic constraints.

Other folding schemes will result in a greater number of DoFs than that of their zero-thickness origami counterparts. As a result, the folding and subsequent deployment of the arrays require multiple actuations, making the control process rather complex.

1.2 Aim, scope and layout

Given the shortcomings of the existing approaches, this research aims to develop new approaches to folding an array of rigid panels with a uniform thickness into compact stacks without any voids.

This dissertation is structured into seven chapters. Apart from this introductory chapter and a conclusion chapter, the others are outlined as follows.

Chapter 2 is a literature review encompassing the past research efforts in deployable space structures and the methods to analyse them. Numerous designs are firstly revisited, in which most bi-directional folding concepts originate from origami due to its advantage in transforming large thin sheets into compact volumes. To pack engineering materials with a finite thickness, several techniques are then introduced to accommodate the thickness of materials when folding an origami pattern. After that, the thick-panel origami is shown to be kinematically equivalent to closed-loop spatial linkages. Methods are detailed for the kinematic analysis if it is a single-DoF assembly. If not, multi-body dynamic analysis is presented for a collision-free deployment process.

Chapter 3 presents a Hamiltonian circuit (HC) approach to folding an array of rigid panels with uniform thickness into a compact volume. By placing revolute joints on the top and bottom

facets of the thick panels consecutively according to an HC planned within the array, a chessboard-like array of identical rectangular panels can be folded into two stacks without any voids. The HC approach can also be applied to arrays of other regular geometries, such as equilateral triangles and regular hexagons. Physical prototypes are made to validate the designs. However, the HC approach usually results in a multiple-DoF assembly, creating difficulties in synchronising the deployment process.

Chapter 4 explores the collision-free deployment for a multiple-DoF assembly that results from the HC approach. Spring-loaded hinges are strained at the stowed configuration to drive the deployment process for an array of identical rectangular panels. Since there is no control mechanism once the deployment starts, the stiffness of spring-loaded hinges must be chosen carefully to avoid any collision among panels. Therefore, an optimisation process, including both multi-body dynamic modelling of the deployment process and collision detection, is carried out to obtain suitable spring stiffnesses at various hinge locations. Finally, experiments on a thick-panel prototype are presented to demonstrate the feasibility of this approach. The deployment process of the prototype is captured by a high-speed camera and it is benchmarked against the simulations.

Chapter 5 unveils a solution to fold a single-DoF array of interlinked flat rigid panels of uniform thickness into compact stacks without any voids. It starts from forming an 8R mechanism element by placing simple and robust revolute joints on the top or bottom facets of isosceles triangular panels according to the HC approach. The geometry of the element is detailed, and its equivalent linkage is introduced. After that, the kinematic formulation is outlined through a numerical approach. Methods of connecting 8R elements are introduced leading to the formation of two types of units, both with a single DoF. Kinematic analysis is then detailed to demonstrate the motion profile of unit I through the analytical method and that of unit II through the numerical approach. The geometric constraints of the units are discussed due to

the physical interference of panels. Finally, some possibilities are presented to combine these two types of units to form a larger array. Though a single-DoF flat surface can be folded into a compact volume, the folded stacks are not conforming to the shape of a cuboid.

Finally, Chapter 6 proposes several arrays that can be folded from a flat surface to a compact volume that is conforming to the shape of a cuboid. Foldable modules are firstly constructed with squares or the combination of squares and half-square triangles, followed by investigating how the modules can be tessellated to form large arrays, with either a small number of DoFs or a single DoF. However, only a limited number of panels can be connected in an array due to the physical interference of panels.

1.3 Associated publications

The following publications are related to the work presented in this dissertation.

Yang, J. & You, Z., 2019. Compactly folding rigid panels with uniform thickness through origami and kirigami. In *Proc. of the ASME IDETC/CIE,* Anaheim, CA,18–21 August. (**Chapter 3**)

Yang, J., Chatzis, M. N., & You, Z., 2021. Collision-free deployments of compact stacks with spring-loaded hinges. In *AIAA Scitech 2021 Forum.* (**Chapter 4**)

Yang, J., Zhang, Y., Chatzis, M.N., & You, Z., 2022. Folding and deploying identical thick panels with spring-loaded hinges. *Extreme Mechanics Letters*, *52*, p.101637. (**Chapter 4**)

Yang, J., Zhang, Y., Chatzis, M. N., and You, Z., 2022. Data for "folding and deploying identical thick panels with spring-loaded hinges". *Data in Brief*, p.108388. (**Chapter 4**)

Yang, J., Zhang, X., Chen, Y., & You, Z., 2022. Folding arrays of uniform-thickness panels to compact bundles with a single degree of freedom. *Proc. R. Soc. A.* 478. (**Chapter 5**)

CHAPTER 2

LITERATURE REVIEW

2.1 Deployable space structures

Many large flat rigid surface structures exist in aerospace applications, e. g., solar panels and reflectarray antennas (Guest & Pellegrino, 1996). They commonly consist of many interlinked panels that fold into a small package before launching and subsequently deploy to a completely flat surface once reaching orbit.

2.1.1 Arrays with unidirectional deployments

The most widely used mechanism to fold rigid surface structures is z-folding, which expands and retracts unidirectionally (Santoni et al., 2014). Its simplicity and high packaging efficiency make it a preferred choice for many missions. One example is shown in Figure 2.1(a), in which each row of solar panels that are attached to the main body of the Juno spacecraft is folded into a bundle for launch. Figure 2.1(b) is another example where each set of fan-shaped rigid panels is packaged together along the circumferential direction (Murphy, 2012).

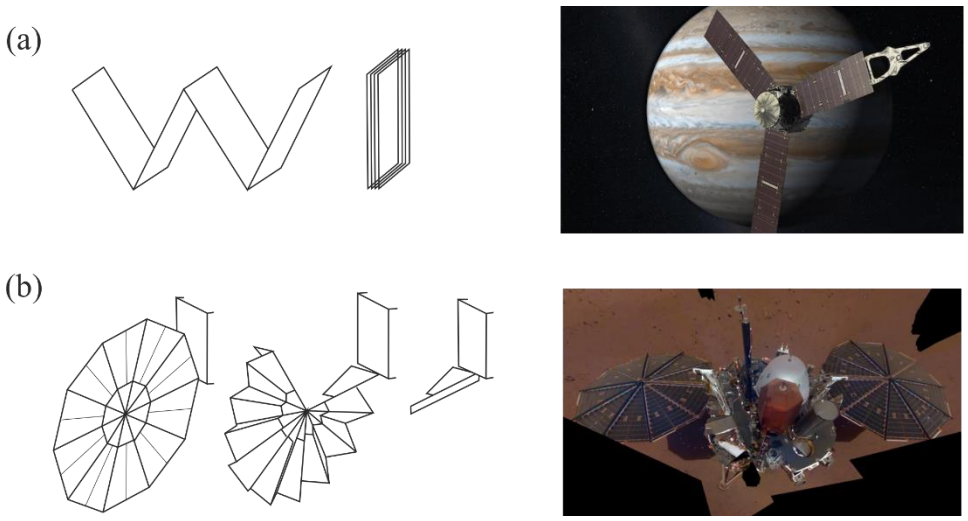

Figure 2.1 Unidirectional deployed solar panels. (a) Z-folded panels on the Juno spacecraft (Dawson et al., 2012), and (b) fan-folded panels on the Insight Mars rover (Wall, 2018).

Both solutions provide excellent compactness in the stowed configuration, but the number of panels that can be connected is limited. Since the panels deploy to a rather long cantilever beam, the overall structure could become rather flexible when the number of panels is large. Also, a synchronisation mechanism needs to be used to deploy the packaged stack as the z-folding is not a single-DoF system if the number of panels is greater than two. Considering these issues, engineers resorted to using multiple stacks of panels when a larger surface is required (Blackwell et al., 2012; Dawson et al., 2012). However, doing so further increases the difficulty in synchronising the deployment process. To solve this problem, deployable flat arrays with bi-directional deployment features become necessary.

2.1.2 Origami-adapted designs for bi-directional deployments

Most bi-directional folding concepts in space applications can trace their origins to origami because of their advantage in transforming large thin sheets into compact volumes. Origami patterns with such a characteristic include the Miura-ori (Nishiyama, 2012), the

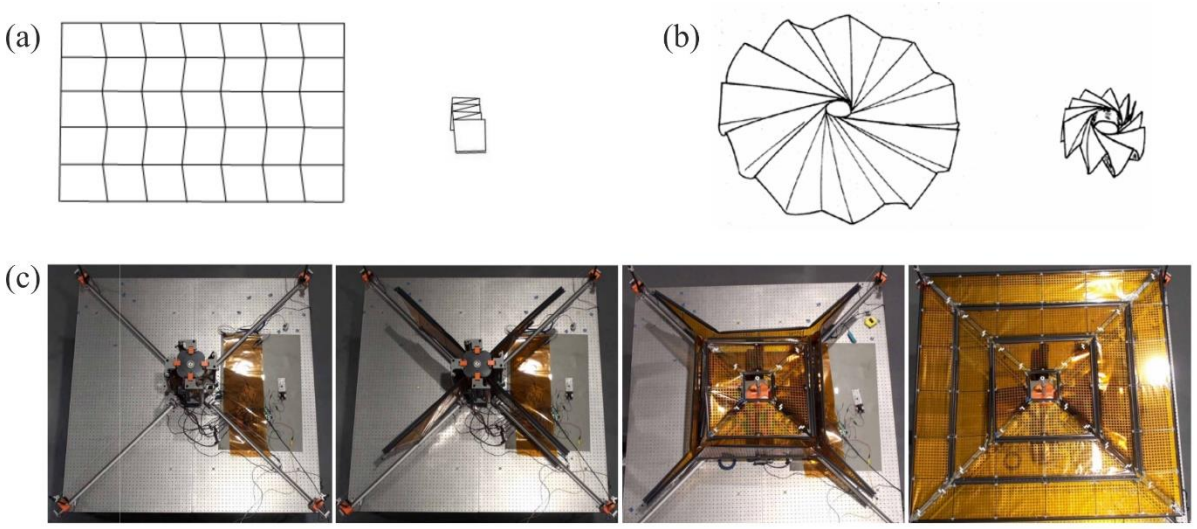

Figure 2.2 Origami-adapted bi-directional deployments for thin sheets. (a) The Miura-ori pattern (Nishiyama, 2012), (b) the wrapping mechanism (Guest & Pellegrino, 1992), and (c) the coiling mechanism from folded to the deployed configuration (Gdoutos et al., 2020).

Wrapping (Guest & Pellegrino, 1992), and the coiling pattern (Arya et al., 2015; Gdoutos et al., 2020), as shown in Figure 2.2. They have demonstrated bi-directional folding with a large deployment ratio, which is defined as the ratio between the surface footprints of expanded and folded configurations. However, they are primarily applicable to pack surfaces made from thin sheets or flexible membranes with negligible thickness. A different approach is necessary for packaging arrays consisting of thick panels, which will be reviewed in Section 2.2.4 after the introduction of some fundamental concepts of origami engineering.

2.2 Concepts for design and modelling of origami models

2.2.1 Rigid origami

An origami pattern consists of creases and vertices where creases meet. The simplest origami pattern consists of a single-vertex origami with four creases as shown in Figure 2.3. The creases are characterised by two types, the mountain and valley creases, marked by the blue

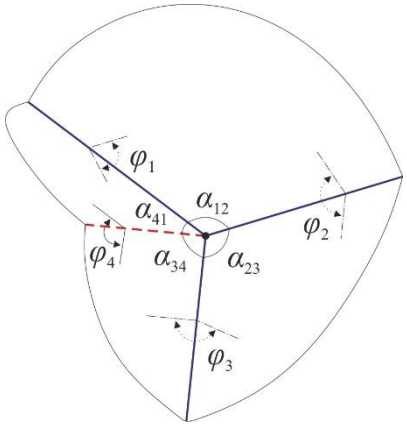

Figure 2.3 A partially folded single-vertex rigid origami model with four creases.

solid lines and the red dash line, respectively. They divide a sheet into four facets, with sector angles α_{12}, α_{23}, α_{34}, and α_{41}. The sum of these sector angles equals 2π. Between any two consecutive facets, a dihedral angle φ_i is defined along their shared crease.

If the facets are assumed to be rigid and can rotate with respect to each other along the creases, the origami is known as rigid origami. Rigid origami ensures no stretching or bending on any facets during the folding process, which is crucial when designing an origami-adapted folding scheme for solar arrays or reflectarray antennas as the on-board electronics are, in general, expensive and sensitive to deformations. To achieve rigid foldability, the geometric features of an origami pattern shall be carefully designed such that the facets around a vertex are geometrically compatible with each other during deployment. Furthermore, if an origami pattern is rigidly foldable, the kinematics of the pattern can be predicted using the theory of mechanisms. The kinematics modelling is reviewed in Section 2.3.

2.2.2 Tessellation origami

Mathematically tessellation, also known as planar tiling, is a way to cover a surface with a set of repetitive patterns without overlaps or gaps (Conway et al., 2016). For instance, two types of polygons, squares and equilateral triangles, are spanning a plane as shown in Figure 2.4(a).

Besides, the Miura-ori pattern in Figure 2.2(a) is a tessellation of parallelograms. This type of origami pattern is known as tessellation origami. As the solar arrays and reflectarray antennas are commonly made from identical panels, it is important to study the tessellation origami constructed by one type of polygon as demonstrated in Figure 2.4(b)-(f).

In tiling, an edge is a bordering line between two shapes and a vertex is the point of intersection of three or more edges. In any tessellation, the angles around a vertex shall always sum to 2π. Among all the tessellations, a regular tessellation involves only one type of regular polygon to create a periodically repeating pattern (Coxeter, 1973). Only three regular polygons, equilateral triangles, squares, and regular hexagons, can form regular tessellations, which are illustrated in Figure 2.4(d)-(f) (Grünbaum & Shephard, 1986).

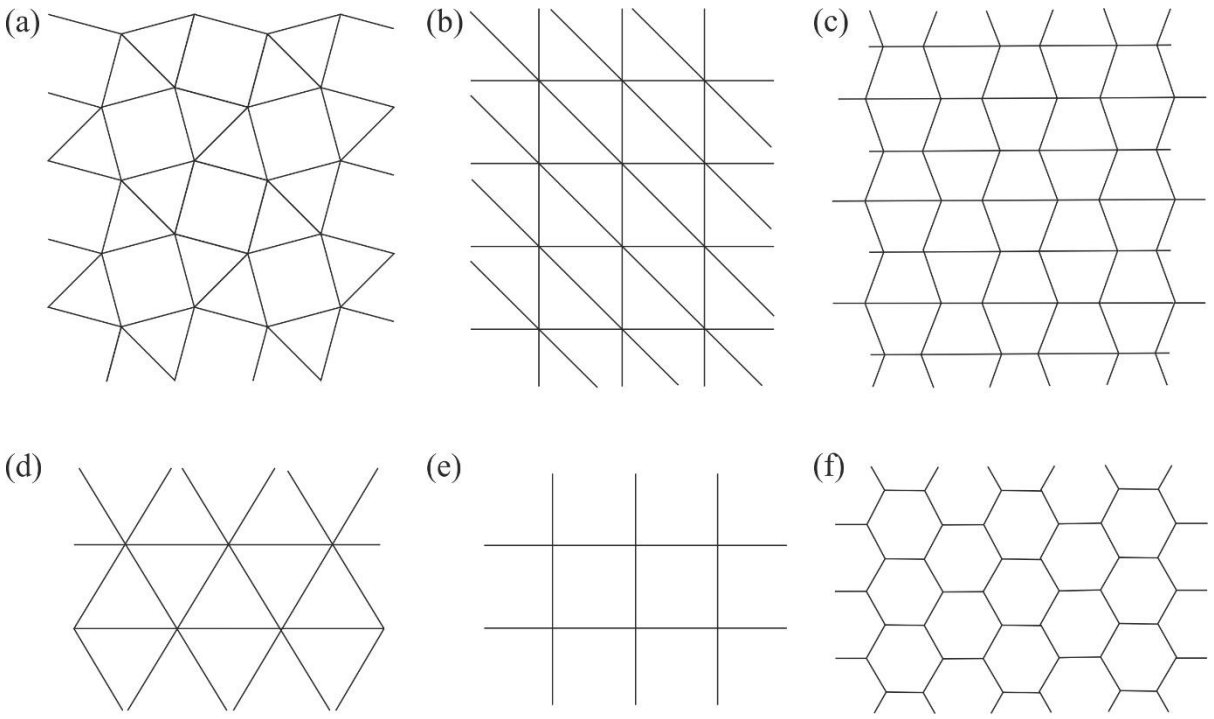

Figure 2.4 Tessellating a plane with polygons. Tessellations of (a) squares and equilateral triangles, (b) half-square triangles, (c) trapezoids, (d) equilateral triangles, (e) squares, and (f) regular hexagons.

2.2.3 Hamiltonian circuit in a grid graph

Selecting an area in a tessellation, an array is formed with a finite number of polygons. A grid graph G can then be created if the polygons in an array are treated as nodes and the connectivity of the polygons is considered as lines (Itai et al., 1982). Three examples of grid graphs are shown in Figure 2.5(a)-(c), where the polygonal tiles are plotted in light grey, and the grid graphs are in black. It is worth noticing that the connectivity of equilateral triangles is a hexagonal grid graph, whereas a triangular grid graph is embedded in the array of regular hexagons.

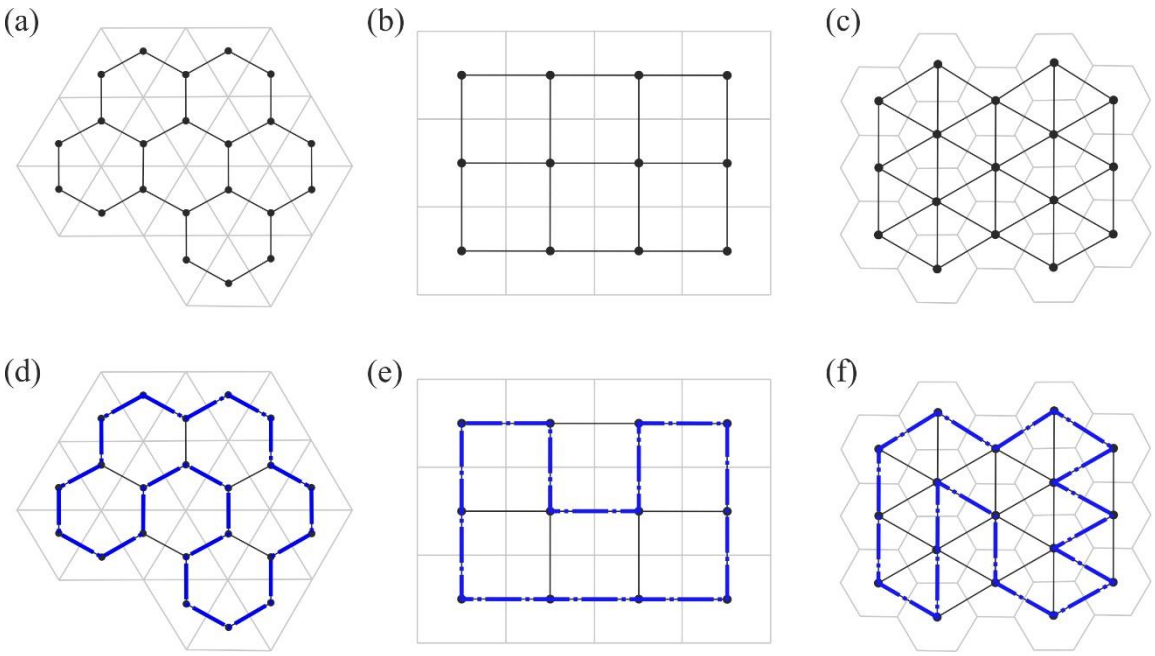

Figure 2.5 Grid graphs in the arrays of (a) equilateral triangles, (b) squares, and (c) regular hexagons. (d)-(f) A Hamiltonian circuit is plotted in blue dotted dash lines within each grid graph.

In a grid graph, a Hamiltonian circuit (HC) is a closed path that visits every node only once and returns to its starting node. Figure 2.5(d)-(f) show examples of HC, which are plotted in blue dotted dash lines. Finding all HCs within a grid graph is mathematically NP-complete (Garey & Johnson, 1979). In simple words, it means that a solution is not guaranteed to be found, but if there is any, it can be verified quickly (in polynomial time). Therefore, the most common technique to identify HCs within a given graph is through an exhaustive search (Danielson, 1968).

In an array of equilateral triangles, in which a hexagonal grid graph can be plotted, HC does not always exist (Islam et al., 2007). However, in the arrays of rectangles and regular hexagons, in which square and triangular grid graphs can be plotted, respectively, HC can always be found when the number of nodes in the graphs is even (Afrati, 1994; Gordon et al., 2008).

2.2.4 Thick-panel origami

Thick-panel origami is a subset of rigid origami. When limited types of panel shapes are used, it is also a subset of tessellation origami. Various thick-panel accommodating techniques have been proposed to pack arrays composed of rigid panels of a finite thickness (Lang et al., 2018). The six most prominent ones are summarised in Figure 2.6.

Figure 2.6(a) illustrates the offset panel technique (Edmondson et al., 2015). It positions the thick panels away from the zero-thickness surface while keeping the kinematic behaviour of the entire structure the same as its zero-thickness counterpart. However, voids are found amongst panels and along the hinges in the fully folded state while applying the technique to the Miura-ori. In Figure 2.6(b), the hinge shift technique places the simple revolute joints on either the top or bottom surface of thick panels (De Temmerman et al., 2007; Hoberman, 2010). However, only origami patterns with a symmetric distribution of vertices were demonstrated such as the bird's foot (Hoberman, 1988) and the Miura-ori. Chen et al. (2015) proposed a general scheme to model origami patterns by mechanisms. Origami patterns with zero-thickness can be modelled by spherical linkages, where the fold lines (axes of revolution) meet at a single point, whereas thick-panel origami can be modelled by spatial linkages such that the revolute joints are neither concurrent nor parallel. The approach, known as the thick-panel origami, required the thickness of each panel to be carefully designed so that the motion of their zero-thickness counterparts can be preserved. The approach yielded several very interesting results, one of which is shown in Figure 2.6(c), and was extended to thick-panel kirigami (Wang et al., 2018). However, the drawback of this approach is that it does not ensure that the overall surface in the deployed state is completely flat. In Figure 2.6(d), the double-hinged technique (Ku & Demaine, 2016) modifies a zero-thickness model by splitting one fold line into two. The modified zero-thickness model remains as the centre line of its thick-panel counterpart and the material in the corner of the thick panels is trimmed away to avoid physical

interference in the folded state. In Figure 2.6(e), the membrane technique (Zirbel et al., 2013) backs the thick panels with thin membranes. By increasing the separation between valley folds, the membranes accommodate the panel thickness and allow folding. However, the kinematics of the panels are difficult to predict due to the flexible membranes. The last technique folds an assembly of panels with uniform thickness using rolling contact joints (Lang et al., 2016), which is sketched in Figure 2.6(f). Although the scheme has only one DoF, the voids remain in the fully folded state of the thick-panel assembly. Besides, a joint with rolling contacts is far more complicated to manufacture than a revolute joint.

As each technique has its advantages and disadvantages, we use four metrics to characterise them in Table 2.1. More specifically, they are rigid foldability – whether the thick-panel counterparts are rigidly foldable, kinematics equivalence – if their kinematics are identical to those of the zero-thickness origami, flat surface – checks if the thick panels have a flat profile in the deployed state, and manufacturing simplicity.

Table 2.1 A comparison of thick-panel accommodation techniques

	Rigid foldability	Kinematics equivalence	Flat surface	Manufacturing simplicity
Offset panel technique	✓	✓	x	x
Hinge shift technique	✓	x	x*	✓
Thick panel origami	✓	x	x	✓
Double hinged technique	✓	x	x	x
Rolling contacts technique	✓	x	x	x
Membrane technique	x	x	x	✓

* Exception for special cases

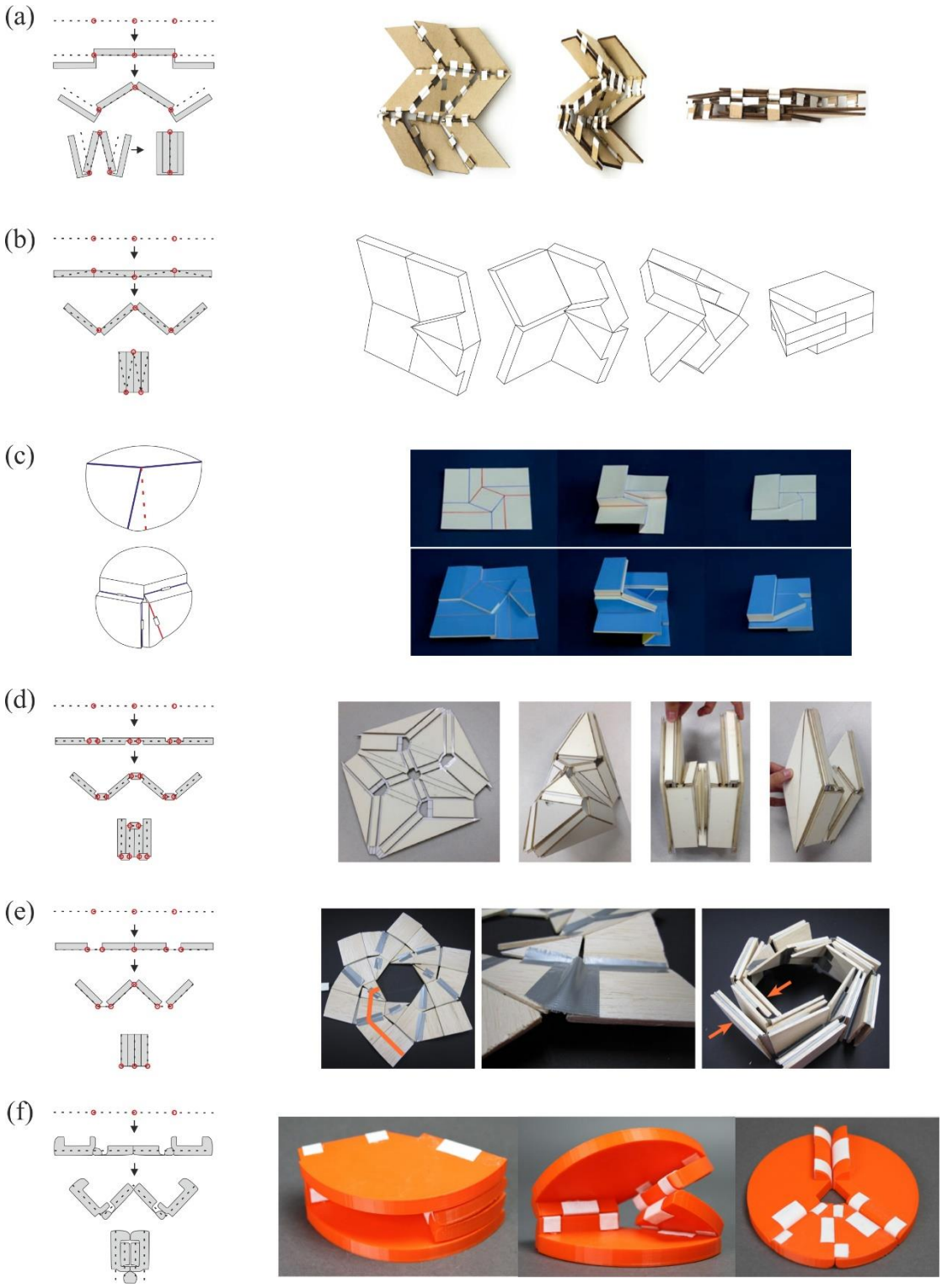

Figure 2.6 Some techniques for accommodating thick panels in origami designs. (a) Offset panel technique and its application on Miura-ori (Edmondson et al., 2015); (b) Hinge shift technique and its implementation on Miura-ori vertex (Hoberman, 2010); (c) Thick-panel origami and its implementation on the square-twist pattern (Chen et al., 2015); (d) Double hinged technique and its application on the bird-base pattern (Ku & Demaine, 2016); (e) Membrane technique and its implementation on a six-sided flasher (Zirbel et al., 2013); and (f) Rolling contact technique and its implementation on bird's foot vertex (Lang et al., 2016).

2.3 Kinematics of thick-panel origami

Kinematics studies the motion of a mechanism by considering its geometric properties. It is important for the design of deployable solar arrays once a folding scheme is devised. Several kinematic modelling methods have been developed and they are summarised in (You & Chen, 2011), including the widely used matrix method with the D-H notations (Beggs, 1966; Denavit & Hartenberg, 1955), quaternion and dual quaternion methods (Altmann, 1986; McCarthy, 1990), screw theory (Ball, 1876), etc. Some methods are more advantageous than others when modelling certain groups of mechanisms. For designing deployable structures based on thick-panel origami and kirigami, where many such assemblies involve only revolute joints, it is more significant to understand the position and angular position of the panels whereas the other physical properties are of less interest. Therefore, the matrix method with D-H notations is preferred and adopted in this research.

2.3.1 The matrix method

Figure 2.7 shows a portion of interlinked links where the important geometric parameters are labelled. The links, presented in thickened black lines, are connected by three revolute joints $i-1$, i, and $i+1$. At each joint, a coordinate system is set up such that the axis z_i is along the axis of joint i and axis x_i is along the common normal line from z_{i-1} to z_i. Axis y_i is not shown in the figure, but it can be obtained by the right-hand rule. Link length $a_{(i-1)i}$ measures the distance between axes z_{i-1} and z_i, positively along x_i. $\alpha_{i(i+1)}$ is the twist angle from axes z_{i-1} to z_i positively about x_i. Offset d_i is the distance between x_i to x_{i+1}, positively along z_i. Finally, the kinematic variable θ_i is the angle of rotation from x_i to x_{i+1}, positively about the z_i axis.

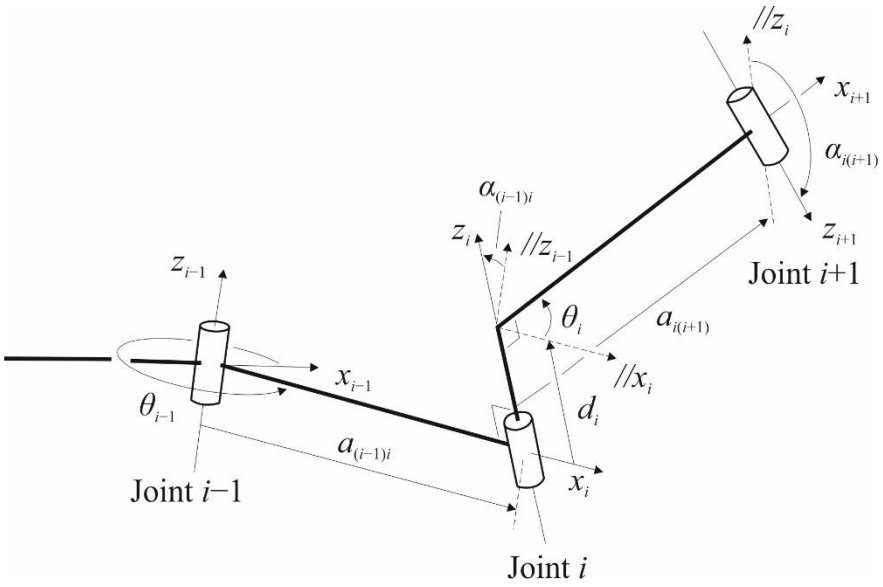

Figure 2.7 Coordinate systems set up in D-H notations for links connected by revolute joints.

Denavit & Hartenberg define $\mathbf{T}_{i(i+1)}$ as a 4×4 homogenous transformation matrix between the coordinate systems at joints i and $i + 1$:

$$\mathbf{T}_{i(i+1)} = \begin{bmatrix} \cos\theta_i & \sin\theta_i & 0 & -a_i \\ -\sin\theta_i \cos\alpha_{i(i+1)} & \cos\theta_i \cos\alpha_{i(i+1)} & \sin\alpha_{i(i+1)} & -d_i \sin\alpha_{i(i+1)} \\ \sin\theta_i \sin\alpha_{i(i+1)} & -\cos\theta_i \sin\alpha_{i(i+1)} & \cos\alpha_{i(i+1)} & -d_i \cos\alpha_{i(i+1)} \\ 0 & 0 & 0 & 1 \end{bmatrix} \tag{2.1}$$

The inverse of $\mathbf{T}_{i(i+1)}$ turns out to be

$$\mathbf{T}_{i(i+1)}^{-1} = \mathbf{T}_{(i+1)i} = \begin{bmatrix} \cos\theta_i & -\cos\alpha_{i(i+1)} \sin\theta_i & \sin\alpha_{i(i+1)} \sin\theta_i & a_i \cos\theta_i \\ \sin\theta_i & \cos\alpha_{i(i+1)} \cos\theta_i & -\sin\alpha_{i(i+1)} \cos\theta_i & a_i \sin\theta_i \\ 0 & \sin\alpha_{i(i+1)} & \cos\alpha_{i(i+1)} & d_i \\ 0 & 0 & 0 & 1 \end{bmatrix} \tag{2.2}$$

For a linkage consisting of n links forming a loop, the product of all transformation matrices equals a 4×4 identity matrix $\mathbf{I}_4$, which is known as the loop closure equation for the assembly:

$$\mathbf{T}_{21}\mathbf{T}_{32}\mathbf{T}_{43}\ldots\mathbf{T}_{n(n-1)}\mathbf{T}_{1n} = \mathbf{I}_4 \tag{2.3}$$

Based on the loop closure equation, the motion of a spatial linkage can be devised.

2.3.2 Modelling thick-panel origami and kirigami as spatial linkages

Transforming an origami pattern from zero-thickness to a thick-panel model, fold lines replace creases, and are placed either on the top or bottom edges of the thick panels. In zero-thickness origami, a set of creases meet at each vertex. However, this is no longer true in thick-panel origami as the axes of fold lines (or revolute joints as they are known in the theory of mechanisms) no longer intersect at one concurrent point. Demonstrated by a comparison, Figure 2.8(a) is a 4-crease single vertex zero-thickness origami, and Figure 2.8(b) is its thick-panel counterpart where a revolute joint along the dotted red line is placed on the top surface of the panels whereas the other three revolute joints in solid blue lines are placed on the bottom. When rigid panels are treated as links, the thick-panel counterpart is effectively a spatial loop linkage where links of finite lengths are connected by a set of revolute joints (Chen et al., 2015). φ_i is the dihedral angle between a pair of adjacent panels with a common joint along z_i. If it is foldable, the 4-crease thick-panel origami must be a Bennett linkage, the only spatial 4*R* linkage. Similarly, foldable 5-crease and 6-crease thick-panel origami must be one of the well-studied spatial linkages, e.g., a Myard linkage or a Bricard linkage, etc. The offsets between adjacent links are zero for a thick-panel origami since their *x*-axes are connected end-to-end.

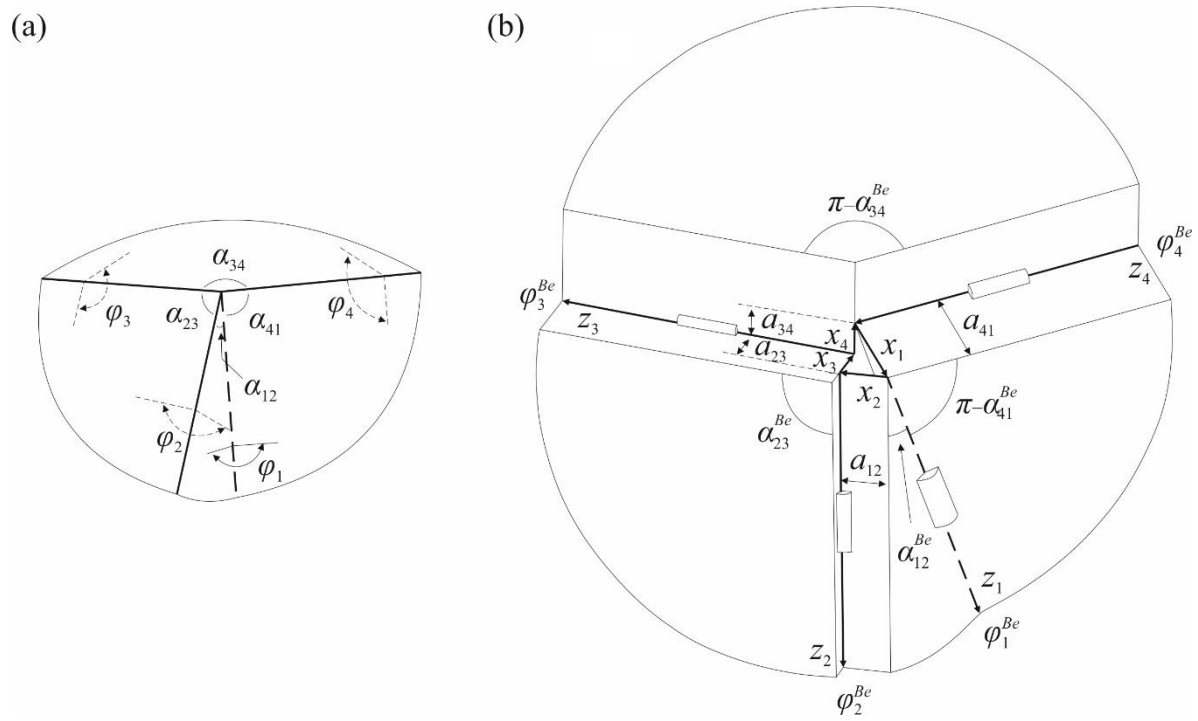

Figure 2.8 (a) A 4-crease rigid origami model and (b) its thick-panel counterpart (Chen et al., 2015).

If an origami pattern contains more than one vertex, it is treated as an assembly of linkages. For instance, Figure 2.9 shows a pattern with two 4-crease vertices. When the sheet has zero thickness, it can be regarded as two spherical linkages where they share a common dihedral angle about AB. Its thick-panel counterpart must be kinematically equivalent to an assembly of two Bennett linkages.

When a slit is made along crease AB, the origami model becomes a kirigami model, as demonstrated by the partially folded example in Figure 2.10(a). The thick-panel counterpart of the kirigami model is shown in Figure 2.10(b). It has non-zero offsets (Wang et al., 2018) as some of the *x*-axes for adjacent links are a distance apart. It must be equivalent to a spatial 6*R* linkage if it can fold up.

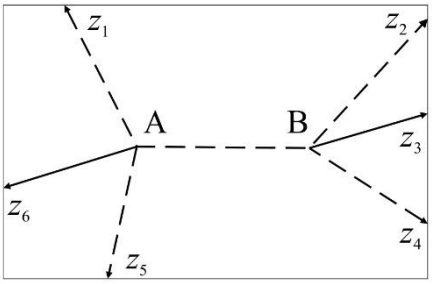

Figure 2.9 An origami pattern with two vertices where dotted lines represent valley creases and solid lines represent mountain creases.

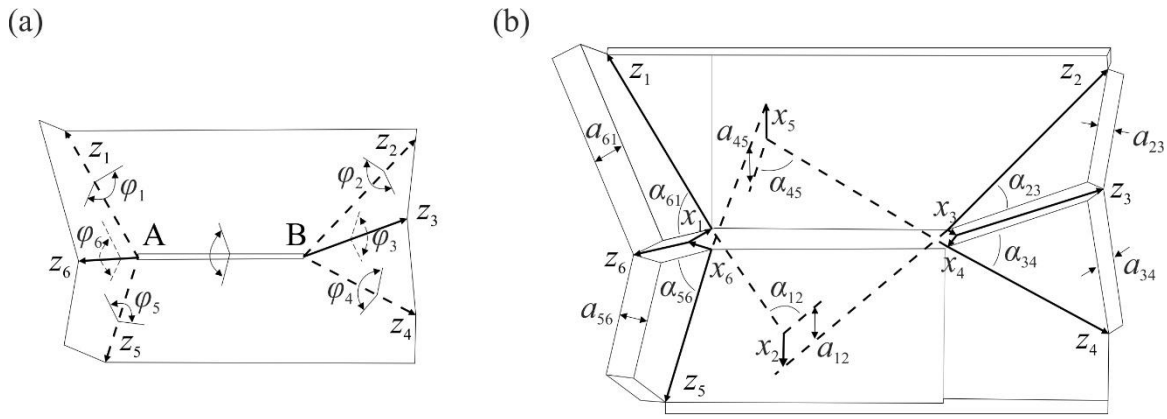

Figure 2.10 (a) A zero-thickness kirigami model and (b) its thick-panel counterpart (Wang et al., 2018).

A general thick-panel origami model with multiple vertices can be regarded as a mobile assembly of spatial linkages consisting of multiple closed loops (Zhang & Chen, 2018). It always has zero offsets in its equivalent linkage, whereas a thick-panel kirigami model with many vertices is also kinematically equivalent to a mobile assembly of spatial linkages but with non-zero offsets due to the slits.

2.3.3 Number of DoF of the thick-panel origami

An important feature to characterise any mechanism is the number of DoF, also known as the mobility of a mechanism. It is the number of independent inputs required to fully define the

configuration of a mechanism (Ionescu et al., 2003). In the three-dimensional space, the number of DoF of an assembly, *m*, can be calculated using the Grübler–Kutzbach mobility criterion (Hunt, 1978), hereinafter referred to as the Kutzbach criterion:

$$m = 6(n-1) - \sum_{i=1}^{j} (6 - f_i) \tag{2.4}$$

where n is the number of links, j is the number of joints, and f_i is the number of DoF of the joint i (i = 1, 2,…, j).

A mechanism is identified with $m > 0$. When $m \leq 0$, the assembly could be a structure, but it may still be a mechanism. This is because the Kutzbach criterion does not consider the geometry of an assembly and thus cannot provide correct mobility in some cases. The mechanism where the Kutzbach criterion yields $m \leq 0$ is known as an overconstrained (or redundant) mechanism. The Bennett, Myard and Bricard linkages are all overconstrained mechanisms because the m of these linkages is less than zero according to the Kutzbach criterion, yet they possess a single DoF. The true mobility of an overconstrained mechanism can be determined by solving the loop closure equation (2.3).

Note that sometimes, it is impossible to find the analytical solutions from the loop closure equations. A numerical approach can then be adopted. A Jacobian matrix of the assembly is constructed that is not only based on the loop closure equations of every linkage (Gan & Pellegrino, 2006; Kumar & Pellegrino, 2000), but also on the global constraints that are imposed due to the topology of linkages in the assembly (Müller, 2018). The rank-deficiency of the Jacobian matrix provides instantaneous mobility of the assembly. For instance, if a Jacobian matrix is rank deficient with nullity of two, the assembly is a mechanism with two DoFs.

The mobility of a mechanism can be finite, or infinitesimal. The former indicates a full range of motion whereas the latter is only a trivial motion that occurs at a particular configuration (Calladine & Pellegrino, 1991). Finite and infinitesimal mechanisms can be distinguished numerically by a nudge away from the configuration (Calladine & Pellegrino, 1991; Pellegrino, 1986; Pellegrino & Calladane, 1986). A finite mechanism preserves its rigid-body motion even if a larger displacement is applied, whereas materials have to deform to reach the target configuration for infinitesimal mechanisms.

2.4 Revolute joints in deployable structures

The expansion of deployable structures such as solar arrays is commonly driven by actuators. For a multi-DoF assembly, the number of actuators must be equal to or greater than the number of DoF. Multiple actuators bring extra weight and complexity to the system, making the synchronisation rather challenging and reducing its reliability. Many methods have been proposed to avoid this complication.

One of the simplest approaches is to use spring-loaded hinges whose rest positions coincide with the fully deployed configuration of an assembly. When the assembly is packaged, the springs store elastic energy, and the deployment is passively driven by releasing the elastic energy. In most research for aerospace deployable structures, tape springs are employed to connect rigid bodies (Kwak et al., 2008; Seffen & Pellegrino, 1999) due to their ability to form a localised elastic fold. A tape spring can be seen as a cut-off section from a steel measuring tape. It is bent 180 degrees and the package of panels is held by a latch in the stowed configuration. Once the latch is released, the deployment of the package is initiated because the tape springs will recover to their unstrained configurations.

Seffen and Pellegrino defined a positive moment when the bending moment was applied such that the tape spring was forming a longitudinal radius of curvature that was on the opposite side of its initial transverse radius of curvature, and a negative moment when they were on the same side, shown in Figure 2.11(a). The behaviour of the tape spring is illustrated by the moment-rotation schematic diagram in Figure 2.11(b). The zero-strain configuration is denoted by the point O. If a positive moment is applied, the required moment increases to obtain a larger rotation until the tape spring suddenly buckles and forms a localised deformation. In the M-θ curve, the buckling corresponds to the sudden jump from point A to point B. As M decreases, it does not follow the same path back. Instead, it snaps back at a smaller rotational angle. If a negative moment is applied, the buckle occurs even closer to the equilibrium state, at point C. Therefore, the tape spring has the advantage of locking itself to the strain-free state because the two energy peaks at points A and C are very close to its strain-free state O. Once the latch is released, the elastic energy stored in the tape spring is dissipated via several loading and unloading cycles until the fold angle θ is sufficiently small that the tape locks into the straight configuration (Seffen & Pellegrino, 1999).

Apart from tape springs, torsional springs are used to deploy solar panels on some CubeSats or nano-spacecraft (Santoni et al., 2014; Santoni, 2015). An example is given in Figure 2.11(c). The deployment process is also driven by stored elastic energy, and it is terminated due to a built-in stopper. As a result, the strain energy remains in the final deployed state. The panels that form the structure may swing back and forth before resting at their final configurations. The past research work for both types of elastic hinges has only demonstrated unidirectional deployments.

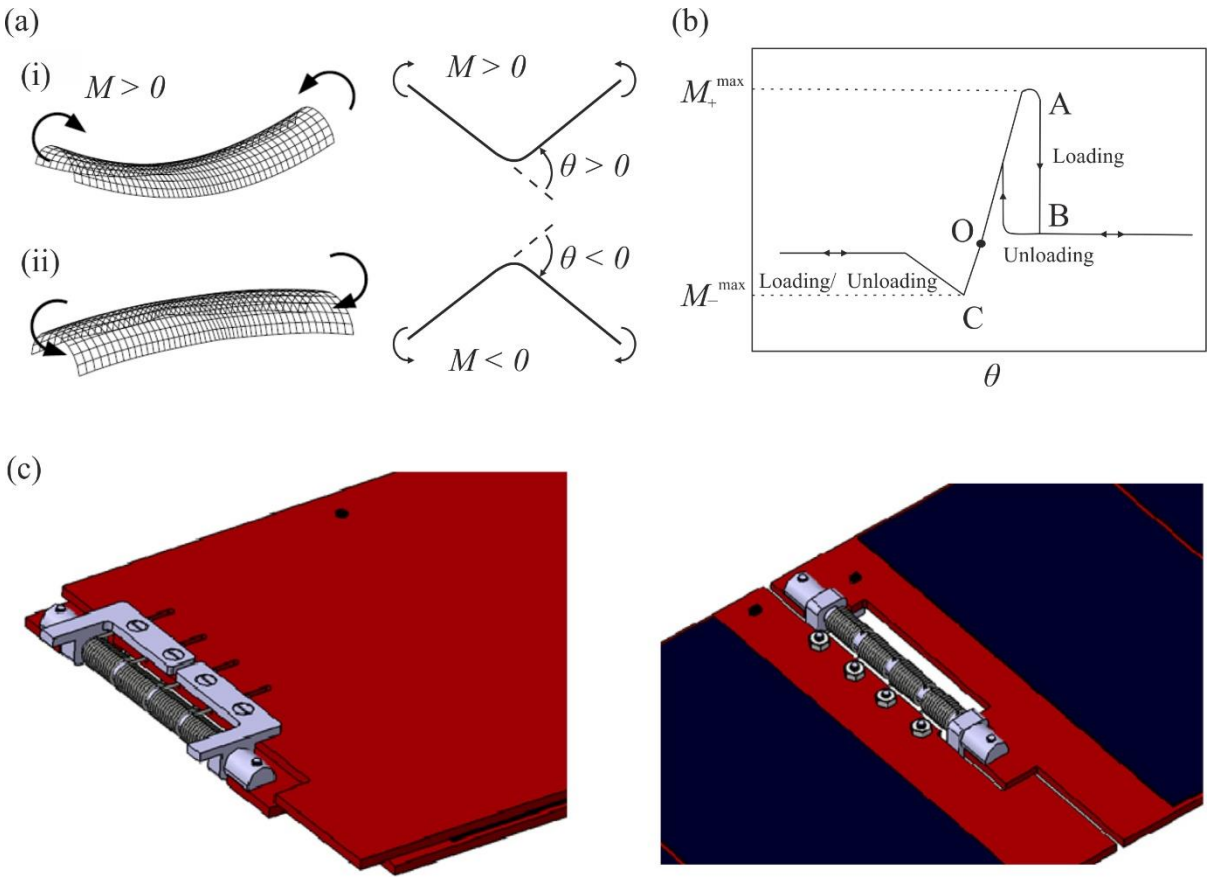

Figure 2.11 An assembly of multiple DoFs can be deployed by spring-loaded hinges. (a) Positive and negative moments are applied on a tape spring and (b) its schematic $M-\theta$ diagram (Seffen & Pellegrino, 1999). (c) Linear torsional springs are used in the stowed and deployed states (Santoni, 2015).

2.5 Multibody dynamics

A deployable solar panel or reflectarray must have a collision-free deployment when spring-loaded hinges are used. Hence, a detailed dynamic analysis is required, using the equations of motion, which are the relationship between forces and the motion of rigid bodies.

There are many methods to formulate the equations of motion of a system. The most widely used methods are the Newton-Euler formulation and Lagrangian formulation (Craig, 1986; Goldstein, 1951; Shabana, 2013). In the former, the equations of motion are derived from Newton's law, which states the relationship between the motion of a point mass and the force

acting on it. Fifty years after Issac Newton formulated his law of motion, Leonhard Euler extended the theory to describe the motion of a rigid body upon external moments or force (McGill & King, 1995). The resulting equations include constraint forces acting between adjacent rigid bodies. In the latter, generalised coordinates are employed to describe the dynamics of a system using an energy approach. All workless forces and constraint forces are not included in this formulation. In this thesis, the forward dynamics of multiple-DoF systems were calculated via MATLAB Simscape, which uses a force-based Newton-Euler formulation (Miller, 2020), and thus, it is reviewed in detail next.

2.5.1 Newton-Euler formulation for an open-loop chain

An open-loop multibody system starts from the ground (also referred to as a base link), moving to a rigid body via a joint, then to another body until the last one in the chain.

In an open-loop chain of n rigid bodies that are connected by revolute joints, a body-attached frame $\{i\}$ is fixed on the centroid of body i ($i = 0, 1, \ldots, n-1$) with its origin being the centroid of the body. The position and orientation of frame $\{i\}$ describe the posture of body i. A joint coordinate ϑ_i is introduced along each joint h_i, allowing only the rotational DoF of the body i with respect to its predecessor $i-1$ about the axis of the joint. This can be better illustrated by an open-loop chain of four rigid bodies that are connected by three revolute joints as shown in Figure 2.12.

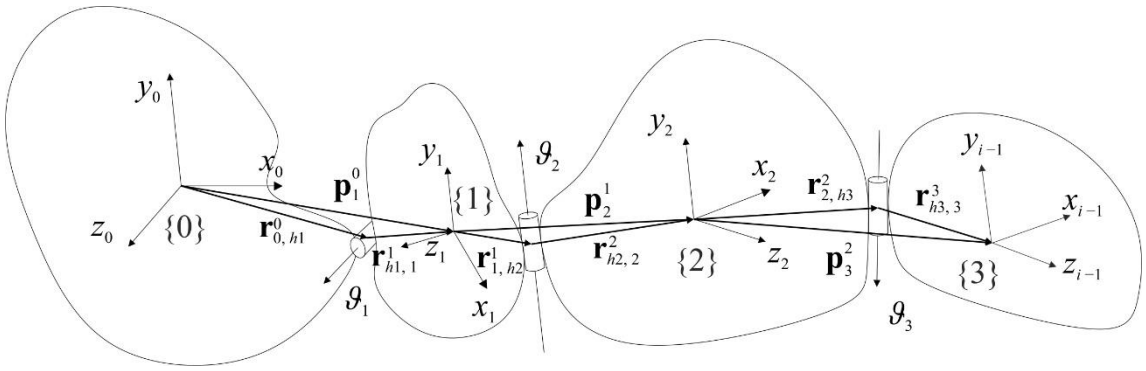

Figure 2.12 An open-loop chain of four rigid bodies that are connected by revolute joints.

Considering the first body 0 is grounded such that its body-attached frame {0} coincides with the fixed world frame. The orientation of frame {1} is defined by a 3 × 3 rotation matrix $\mathbf{R}_1^0$, which is due to the angle of rotation ϑ_1 along joint h_1. The position of the body-attached frame {1} with respect to the world frame {0} can be described by a 3 × 1 translational vector $\mathbf{p}_1^0$. It can be obtained by adding $\mathbf{r}_{0,h1}^0$ and $\mathbf{r}_{h1,1}^0$, being the translation vectors from the origin of {0} to the mid-point of joint 1, and from the mid-point of joint 1 to the origin of frame {1}, respectively, with both vectors expressed in the world frame {0}. Since the vector $\mathbf{r}_{h1,1}^0$ is changing with respect to the change of the angle of the joint ϑ_1, $\mathbf{p}_1^0$ can be re-written as $\mathbf{p}_1^0 = \mathbf{r}_{0,h1}^0 + \mathbf{R}_1^0 \mathbf{r}_{h1,1}^1$, where $\mathbf{r}_{h1,1}^1$ is a configuration-independent vector from the mid-point of joint h_1 to the origin of {1}, expressed in frame {1}.

Similarly, the orientation of frame {2} with respect to {1} due to the rotation of joint h_2 is denoted as $\mathbf{R}_2^1$. The absolute orientation of frame {2} in the frame {0} can be obtained via the dot product of the two rotations, $\mathbf{R}_2^0 = \mathbf{R}_1^0 \cdot \mathbf{R}_2^1$. The coordinate of frame {2} with respect to frame {1} can be expressed as $\mathbf{p}_2^1 = \mathbf{R}_1^0 \mathbf{r}_{1,h2}^1 + \mathbf{R}_2^0 \mathbf{r}_{h2,2}^2$. Its position in frame {0} can thus be computed as $\mathbf{p}_2^0 = \mathbf{p}_1^0 + \mathbf{p}_2^1$. Moving on to the next body in the kinematic chain, the orientation

of frame {3} in the world frame {0} is $\mathbf{R}_3^0 = \mathbf{R}_1^0 \cdot \mathbf{R}_2^1 \cdot \mathbf{R}_3^2$, and its position can be obtained as $\mathbf{p}_3^0 = \mathbf{p}_1^0 + \mathbf{p}_2^1 + \mathbf{p}_3^2$.

Therefore, in an open-loop chain of *n* bodies, the orientation of the body-attached frame $\{i\}$, $\mathbf{R}_i^0$, and its position, $\mathbf{p}_i^0$, can be obtained.

Taking the time derivative and the second time derivative of the translational vector $\mathbf{p}_i^0$, the linear velocity $\mathbf{v}_i^0$ and the linear acceleration $\mathbf{a}_i^0$ of the centroid of the rigid body *i* can be obtained, respectively. The same applies to the angular velocity and the angular acceleration of rigid bodies. For instance, $\boldsymbol{\omega}_i$, the angular velocity of body *i* expressed in its own frame, can be derived based on the angular velocity of its predecessor $i-1$, $\boldsymbol{\omega}_{i-1}$, and the angular velocity of joint h_i, $\dot{\vartheta}_i$, i.e., $\boldsymbol{\omega}_i = \mathbf{R}_{i-1}^i \boldsymbol{\omega}_{i-1} + \dot{\vartheta}_i$; whereas $\boldsymbol{\alpha}_i$, the angular acceleration of body *i* expressed in its own frame, is based on the angular velocity and acceleration of its predecessor, and the angular velocity and acceleration due to the rotation of joint h_i.

The equations of motion (EOM) of a rigid body state that the net force acting on the body equals the rate of change of the body's momentum. Separating the linear and angular velocity terms, the EOM of the rigid body *i* reads

$$\sum \mathbf{f}^i = m_i \mathbf{a}_i \tag{2.5}$$

$$\sum \boldsymbol{\tau}^i = I_i \boldsymbol{\alpha}_i + \boldsymbol{\omega}_i \times (I_i \boldsymbol{\omega}_i) \tag{2.6}$$

where $\sum \mathbf{f}^i$ and $\sum \boldsymbol{\tau}^i$ denote the total force and the total torque applied on the body *i*; m_i and I_i are the mass and the constant moment of inertia of body *i*. Note that all the terms here are expressed in the body-attached frame $\{i\}$. The derivation of the EOM can be found in many dynamics books (Featherstone, 2008; Shabana, 2013; Spong et al., 2004).

2.5.2 Multibody dynamics for a closed-loop chain

One approach to computing the dynamics of such a closed-loop system is through solving the equations of motion under some extra constraints brought together by the Lagrange multipliers, which would lead to a set of differential-algebraic equations (DAEs) (Fuhrer & Leimkuhler, 1991). However, solving DAEs would pose challenges computationally. The other way to tackle the dynamics of a closed chain is to replace some of the constraints with penalty springs (Wang et al., 2002), which is the method adopted in this thesis. To make a closed-loop chain into an equivalent open-loop system, the closed-loop can be cut open along a joint. The constraints along the joint are enforced by translational springs of high stiffness and dampers connecting the two open ends. Theoretically, when the spring is infinitely stiff, it can function equivalent to a revolute joint. All DoFs now become independent because the occurring system corresponds to two open-loop chains. Therefore, the equations of motion of the system can be written as a set of ordinary differential equations (ODEs) that can be integrated numerically in a more straightforward manner. Yet, the penalty springs formulation ensures that the obtained motion of this equivalent open-loop chain system is practically compatible with that of the original closed-loop chain.

CHAPTER 3

COMPACT FOLDING OF ARRAYS WITH REGULAR SHAPES OF UNIFORM THICKNESS

This chapter investigates the design of bi-directionally deployable arrays consisting of flat rigid panels with regular shapes of uniform thickness that can be folded into compact stacks without any voids. In all arrays, the rigid panels are connected by only revolute joints, placed at either the top or bottom common edges of two panels.

3.1 Locations of revolute joints

3.1.1 Placing revolute joints in an array of rectangular panels

Let us first consider an array consisting of identical rectangular panels of a finite thickness as shown in Figure 3.1. It cannot be stored in one stack if the array is to be deployed bi-directionally, but in two stacks instead. Therefore, the objective is to fold an array consisting of $n_r \times n_c$ rectangular panels (n_r or n_c must be even) into two stacks, each of which contains k panels where $k = \frac{n_r \times n_c}{2}$.

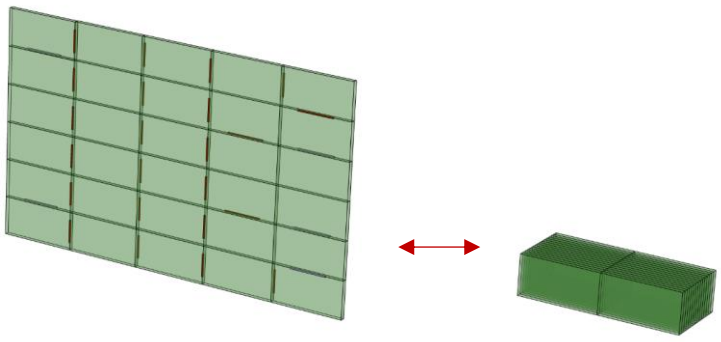

Figure 3.1 An array of identical rectangular panels in deployed and folded configurations.

Folding such an array is analogous to an origami model where each panel is a facet that is connected to its neighbours by revolute joints. These joints are connecting the panels on the top or bottom facet depending on if it is a mountain or valley crease in an origami model.

Now examine an interior facet. It has four neighbouring facets. To package the array compactly, only two neighbouring facets are allowed to be folded over it, one to its top and the other to its bottom surfaces. Hence, this interior facet can only be connected to two out of four neighbouring facets via creases. In other words, no more than two connections (creases) are allowed for each facet. The above argument implies the removal of some creases in an origami

model to free a facet from its other neighbours, which is done by the introduction of slits. The origami then becomes kirigami.

Based on the reason given above, a method can be devised to identify locations for creases. The method is best illustrated graphically with an example array shown in Figure 3.2(a), where $P_{i,j}$ (i = 1, 2, …, n_r and j = 1, 2, …, n_c) represents a facet on the i-th row and j-th column.

Since each facet is only allowed to have two connections, two lines that are perpendicular to the creases can be drawn to indicate their connections with the two neighbouring facets. Bearing this in mind, we can start from $P_{1,1}$ and draw a line connecting $P_{1,1}$ with one of its neighbours, say $P_{1,2}$. From $P_{1,2}$ we extend the line to one of its neighbours, say $P_{1,3}$. This process continues until all facets are linked and the line returns to $P_{1,1}$. All lines form a closed circuit shown in the blue dotted dash lines in Figure 3.2(b). The circuit visits each rectangular facet once and only once and returns to the first rectangular facet at the end. Creases remain if they are perpendicular to the circuit; otherwise, they are replaced by slits. The remaining creases could either be a mountain or a valley, depending on if a neighbour folds over or underneath the facet (Yang & You, 2019).

If an array consists of thick panels, the creases are replaced by revolute joints. Whether a joint is placed at the top or bottom edges depends on if the crease is a mountain or a valley.

Mathematically, the $n_r \times n_c$ rectangles in an array form a group with elements $\{P_{1,1}, P_{1,2}, \ldots, P_{nr,nc}\}$. Elements in the group are re-arranged such that the new order of elements forms a circuit. The circuit must pass through each element once and only once and join back to the first element in the group. Such a circuit is known as a Hamiltonian circuit (HC) (Hamilton, 1856). The placement of revolute joints can then be determined by an HC.

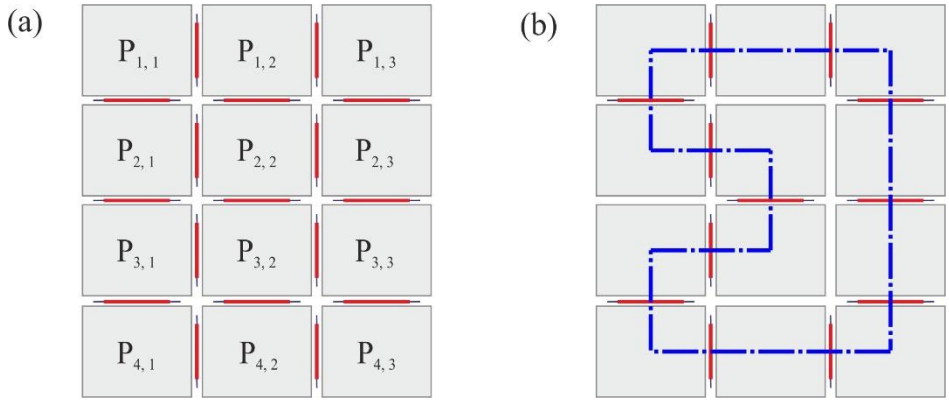

Figure 3.2 Drawing a closed loop within a 4 × 3 rectangular array. (a) Every crease connects two facets. (b) A closed loop is drawn in dotted dash lines within the array. Creases are removed where the path of the loop is not connecting the adjacent facets.

3.1.2 HCs in an array

It is possible to sketch an HC within a small array of identical rectangles, but it becomes more difficult when the array gets larger. Since no theory allows an instant judgement of whether an HC exists or not, the most common technique to search for HC within a given array is through exhaustive search (Danielson, 1968), also known as the brute force algorithm.

First, an undirected grid graph $G = (V, E)$ can be created based on the connectivity of panels in an array. V is a finite set of elements called vertices or nodes in G, with each element representing one panel in the array. The connectivity of the panels is encoded in E, which is a set of unordered pairs of elements in V that are called edges. After that, the grid graph is represented by an adjacency matrix. In a grid graph with n vertices, where $n = n_r \times n_c$, the adjacency matrix $\mathbf{A}$ is an $n \times n$ square matrix such that $A_{ik} = 1$ if there is an edge connecting vertices v_i and v_k, and $A_{ik} = 0$ if there is not.

The grid graph of a 6 × 5 rectangular array is shown in Figure 3.3(a), where the dots represent vertices and the black lines represent edges. The possible connections of panels are enumerated and examined if they are parts of the solutions of an HC through an exhaustive search algorithm

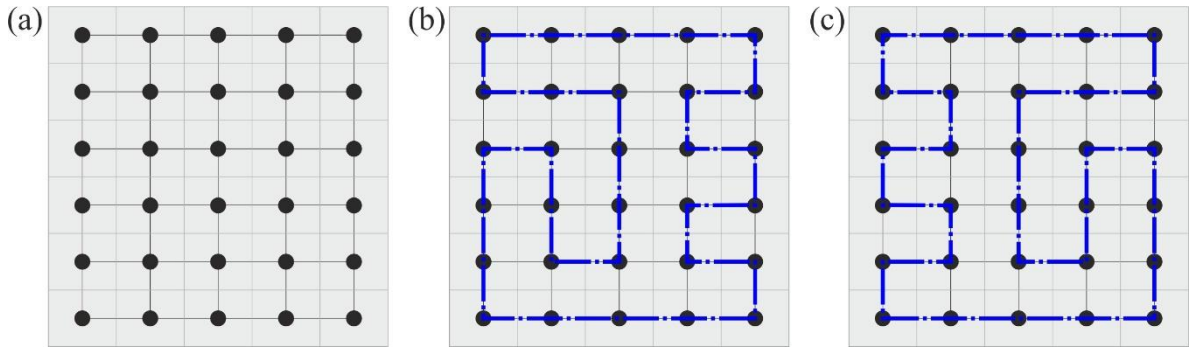

Figure 3.3 (a) A grid graph of a 6 × 5 rectangular array. (b) An HC is plotted in the grid graph and named as graph G_1. (c) Graph G_2 that is isomorphic to G_1.

that can be realised in python (Sharma, 2021). Within the grid graph, an example of the HC is plotted in Figure 3.3(b) by blue dotted dash lines that connect every vertex in the graph, named G_1. Using the program written by Sharma, we can find many HCs but some of them are isomorphic to each other. Two graphs are considered to be isomorphic (Fowler et al., 2016; Sareh & Guest, 2015) if they can be obtained via symmetry operations, such as rotations and reflections. For instance, G_2 in Figure 3.3(c) can be obtained from G_1 via a reflection operation. Here we are only interested in finding the non-isomorphic HC patterns.

There are usually many non-isomorphic HCs within a grid graph. For example, more HCs are found through the exhaustive search in the 6 × 5 array, and six of them are shown by the blue dotted dash lines in Figure 3.4. If an edge is crossed by the path of an HC, a revolute joint is placed on either the top or bottom surface of the panel; if not, a slit is placed, as highlighted in the figure. Although there are many possible ways to arrange the slits, it is not obvious if the slit arrangement can always result in a two-stack foldable configuration, which is discussed next.

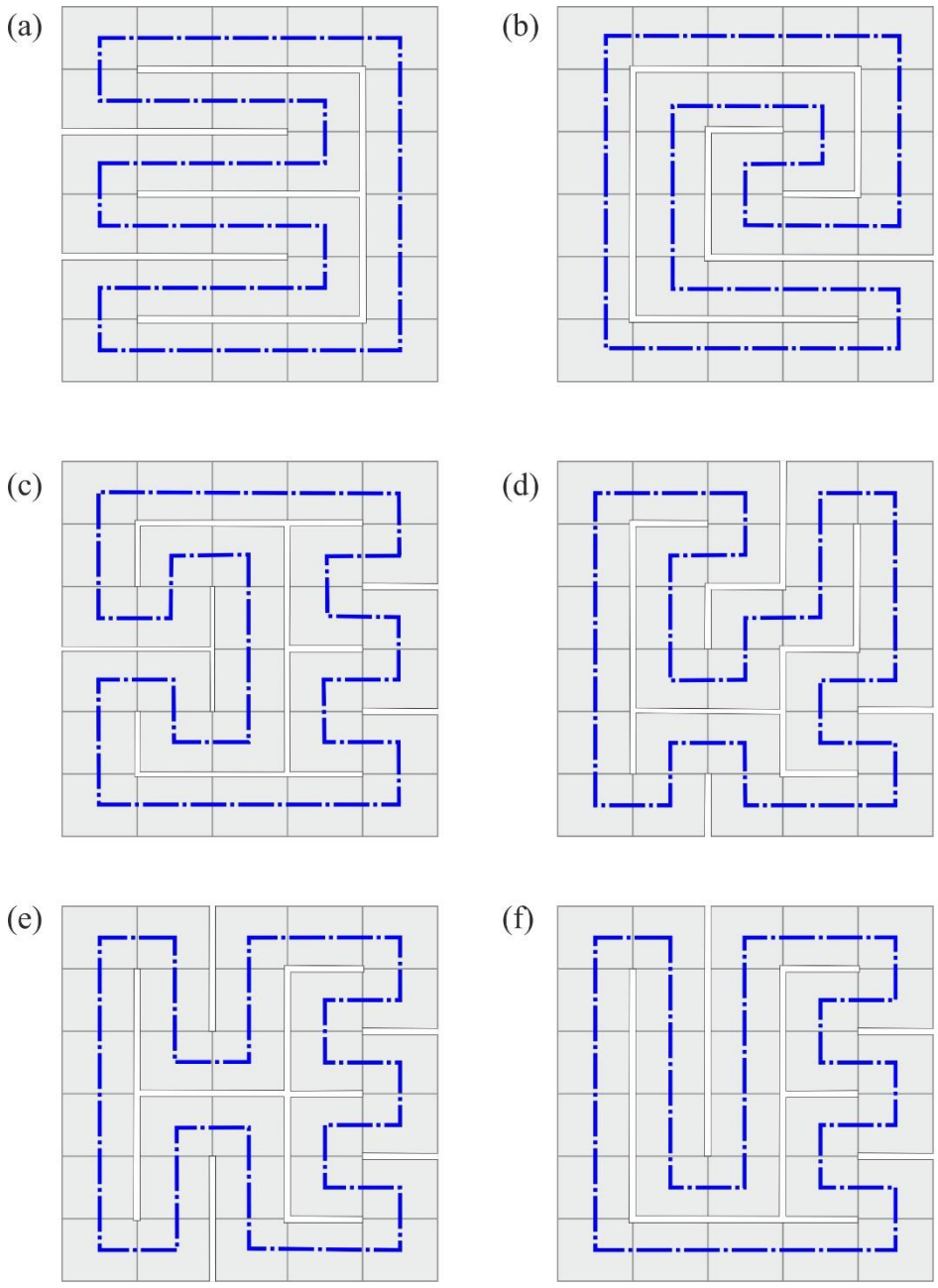

Figure 3.4 Six non-isomorphic HCs are enumerated in a 6 × 5 rectangular array. Slits are made accordingly.

3.2 Selecting the useful HC for two-stack foldable configuration

Placing creases and slits according to the configuration of an HC, an array is turned into a loop of rectangles. Again, representing the panels by dots and the creases by lines, an example of a configuration consisting of 16 rectangles is plotted in Figure 3.5, which can be folded into two

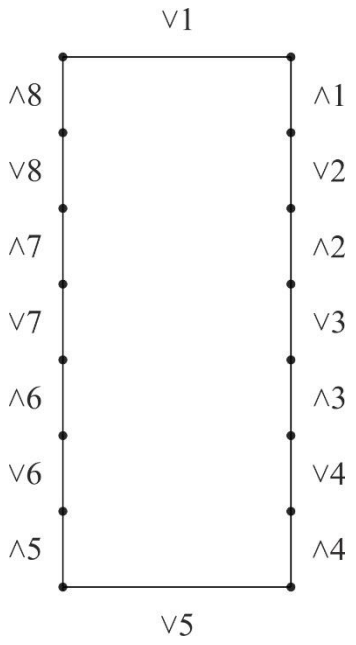

Figure 3.5 A schematic diagram of the folded stacks where dots and lines represent panels and creases, respectively.

stacks with eight layers in each stack. Connecting the panels, mountain creases are labelled as ∧1, ∧2, etc., and valley creases are labelled as ∨1, ∨2, etc. The creases on the top and bottom layers, namely, ∨1 and ∨5, are not required as they will never fold over each other. In other words, the creases between these pairs need not be activated, and thus, they can be removed. Therefore, the resulting number of mountain creases in a two-stack foldable configuration is always different from the number of valley creases by two.

Note that the creases are not always parallel in the folded configuration. They can be orthogonal depending on the connectivity of the rectangles in the array. However, there is an exception with the removed pair of creases, which is on the top and bottom layers of the stacks, in this case, ∨1 and ∨5. The two creases must be parallel as they are connecting the two stacks of the same geometry. Because of this property, we should always identify two pairs of rectangular panels on the top and bottom layers of the folded stacks first if an HC can lead to a two-stack foldable configuration.

3.2.1 Searching for the creases on the top and bottom layers

In a loop of n (n is even) regular polygons, there are n creases. Selecting one crease, marking it in red and cutting it open as shown in the schematic diagram in Figure 3.6(a), the loop is turned into an open chain of rectangles and the crease becomes two edges attaching to both ends of the chain.

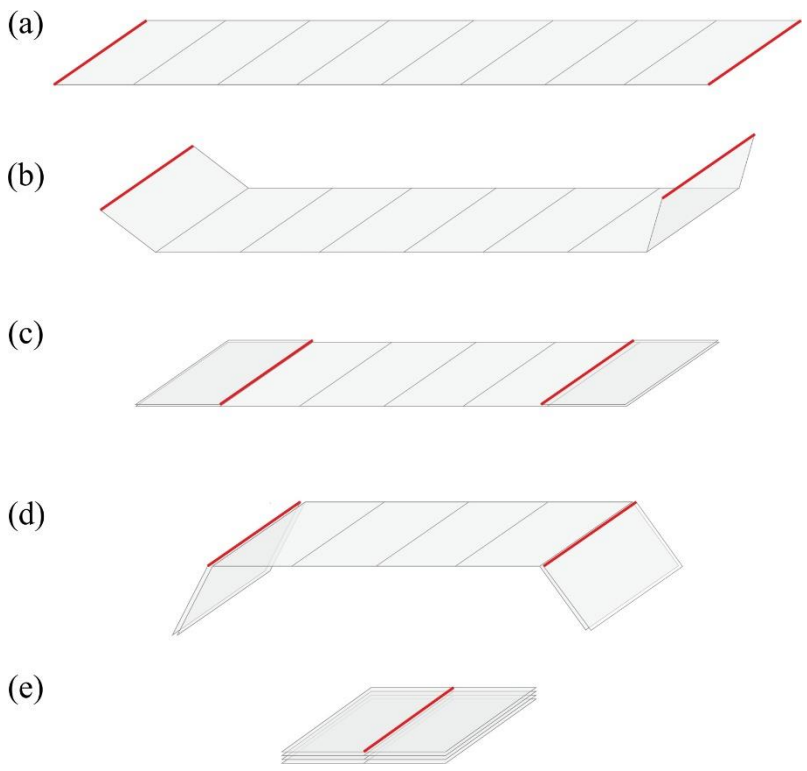

Figure 3.6 The procedure of folding polygons along the creases in an open chain of rectangles. The cut crease is labelled in red.

Taking the rectangle at one end of the chain and folding it over about the crease that it connects, the red crease now overlaps with the edge of the second last rectangle in the chain as shown in Figure 3.6(c). Continuing to fold along the remaining creases in the chain one up and one down for (n/2−1) times, and applying the same procedure to the rectangle at the other end of the chain, the rectangles are now folded into two stacks, with an equal number of rectangles in each stack. If the red edges that are attached on both ends of the loop coincide as shown in Figure 3.6(e),

the selected crease may lie on the top or bottom layer of the folded stacks and coincide with each other. If not, the selected red crease must not be on the outer layers of the stacks. Again, note that the creases in the open chain are not always in parallel if a cut is made in a chessboard-like array.

Let us now apply this method to a 6 × 5 array, in which slits have been made according to the HC plotted in Figure 3.4(f). There are 30 panels in this array and all rectangular panels are labelled in Figure 3.7(a).

If a cut is made along the crease that is connecting $P_{1,1}$ and $P_{1,2}$, the closed loop becomes an open chain, with the red edges being on both ends of the chain as illustrated in Figure 3.7(b). Next, panel $P_{1,1}$ folds about the creases sequentially, and so does $P_{1,2}$. All panels are now folded onto two panels, $P_{3,4}$ and $P_{3,5}$. As demonstrated by Figure 3.7(c), it turns out that the cut edges do not coincide at the end, suggesting that the red crease must not lie on the outer layer.

If we choose the red crease that connects panels $P_{1,2}$ and $P_{2,2}$ as shown in Figure 3.7(d), $P_{1,2}$ and $P_{2,2}$ are folded onto $P_{3,5}$ and $P_{4,5}$, respectively, after a series of z-folding. Now the red edges coincide in the folded stacks, demonstrating that the array can be folded into two stacks in parity and the crease that is connecting panels $P_{1,2}$ and $P_{2,2}$ lies on the outer layer of the folded stacks.

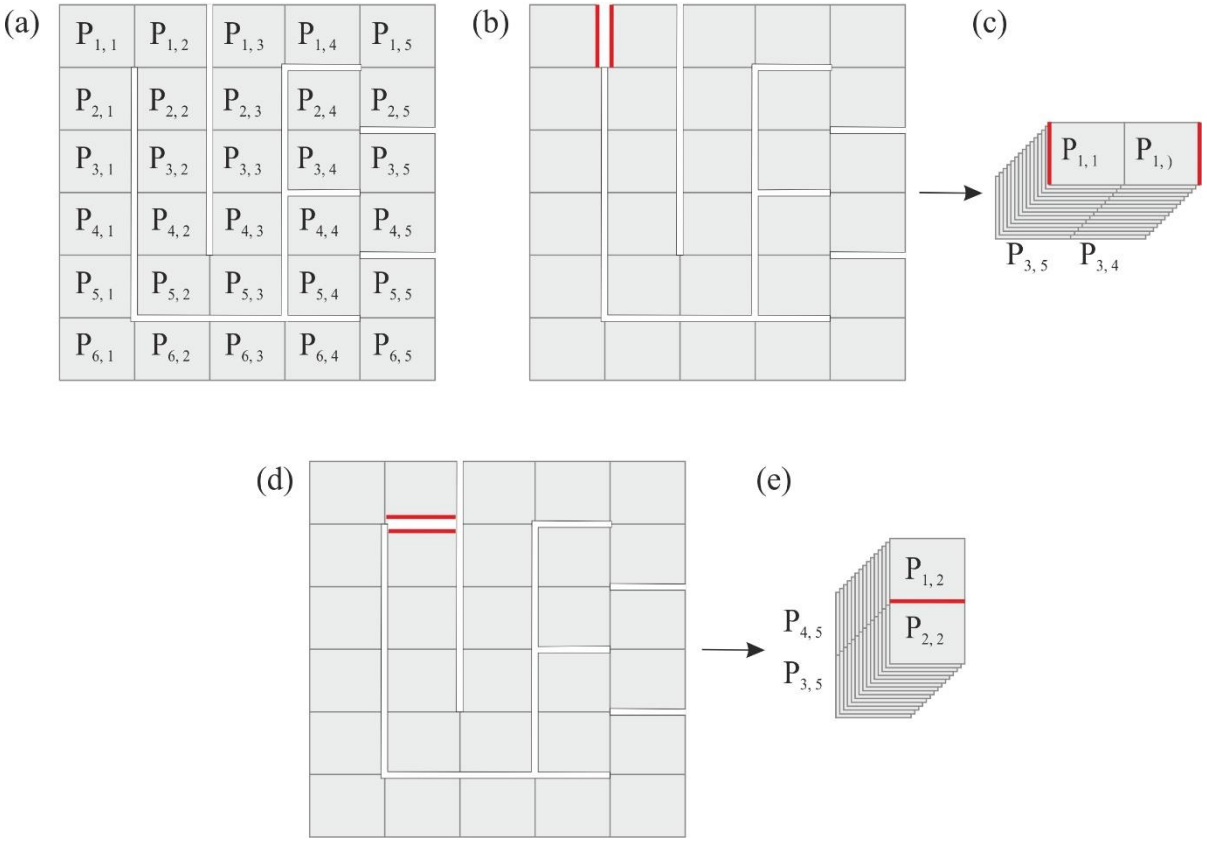

Figure 3.7 Folding a 6 × 5 rectangular array into two stacks. (a) Panels are labelled in the array. (b) - (c) A crease that does not satisfy, and (d) - (e) a crease that satisfies the two-stack foldable criterion.

Mathematically, z-foldings of panels can be regarded as reflection operations about their common creases on a two-dimensional surface. Let us name all creases as e_i (i = 1, 2, …, n) as shown in Figure 3.8(a). If e_1 is chosen as the red crease, as shown in Figure 3.8(b), two identical vectors, $\mathbf{e}_1^+$ and $\mathbf{e}_1^-$ are denoted at the two ends of the open chain, respectively. The vector $\mathbf{e}_1^+$ is reflected about the edges e_2, e_3, …, e_{15} in sequential order, with each operation being tracked by black arrows. Likewise for the vector $\mathbf{e}_1^-$, which is reflected about the creases e_{30}, e_{29}, …, e_{17} in succession. Each after 14 operations, $\mathbf{e}_1^+$ and $\mathbf{e}_1^-$ do not coincide, indicating that the crease e_1 must not be on the top layer of the folded stacks.

If e_2 is selected to be the red crease instead, the vectors $\mathbf{e}_2^+$ and $\mathbf{e}_2^-$ are reflected sequentially as shown in Figure 3.8(c). They coincide at crease e_{17} each after 14 operations, indicating that the

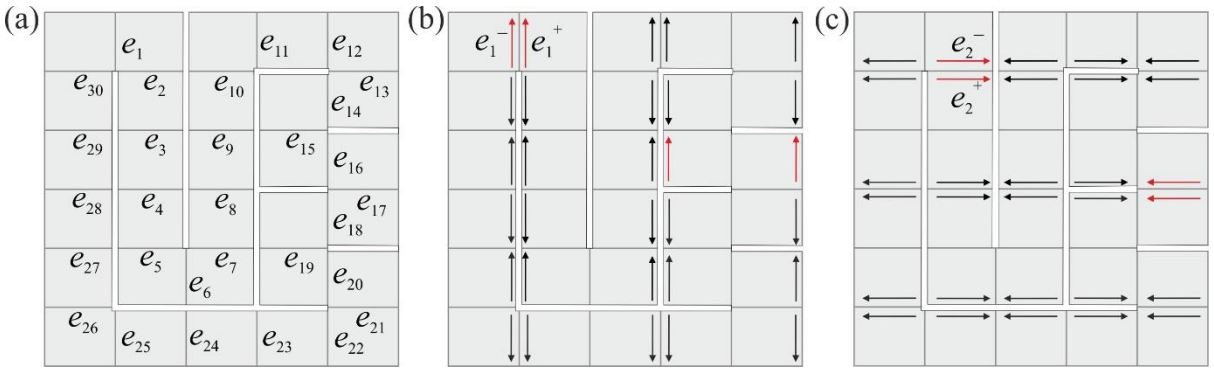

Figure 3.8 Z-foldings can be regarded as reflection operations mathematically. (a) Creases are labelled in a 6 × 5 rectangular array. (b) Vectors $\mathbf{e}_1^+$ and $\mathbf{e}_1^-$ do not coincide, and (c) vectors $\mathbf{e}_2^+$ and $\mathbf{e}_2^-$ coincide, each after 14 reflection operations.

array can be folded in two stacks with the top and bottom layers being $P_{3,5}$, $P_{4,5}$ and $P_{1,2}$, $P_{2,2}$, respectively.

It was tested that all of the HCs plotted in the 6 × 5 arrays in Figure 3.4 lead to two-stack foldable configurations by applying this method, with each stack containing 15 panels. A physical model was made based on the symmetric HC of Figure 3.4(a), which is reproduced in Figure 3.9(a). In the fully folded configuration, the pair of panels at the centre-left appear at the top of the stacks whereas the pair of panels at the centre-right are at the bottom. Both pairs of panels are shaded in darker grey. It can also be noted that the above-mentioned panel pairs never fold over each other. In other words, the revolute joints between the pairs need not be activated. Moreover, due to the symmetrical geometry, the slits along the plane of symmetry are also unnecessary. The five pairs of panels on the two rows of the array can be merged to form five larger panels that are twice the size of the original rectangular panels. The folding sequence of the physical model is given in Figure 3.9(b). Although the slits are present to facilitate the folding process, they are fully closed in the deployed state and the folded state. A completely flat surface is folded to a compact volume without voids.

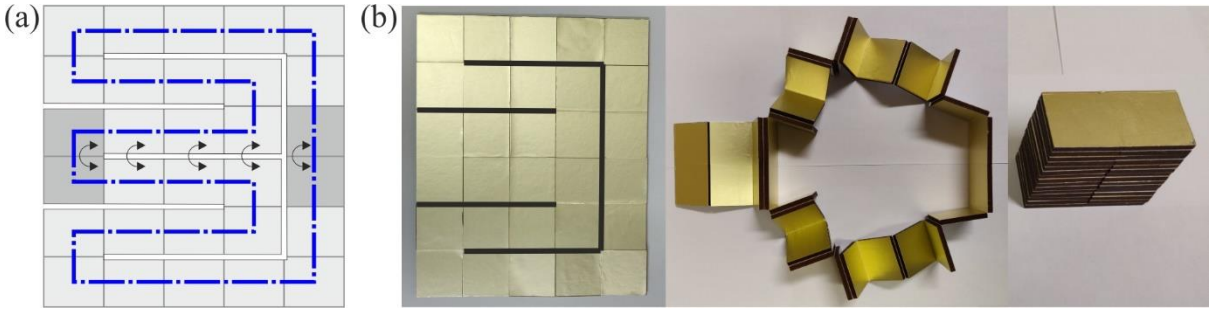

Figure 3.9 A 6 × 5 rectangular array with symmetry. (a) Panels are merged along the plane of symmetry. (b) Folding process of a physical prototype where the thickened black lines in the deployed configuration denote the slits.

3.2.2 DoF of the array

Using the Kutzbach criterion for a spatial closed-loop linkage with revolute joints, the number of DoF is $6(n-1)-5j$ where $n = n_r \times n_c$ is the number of links and j is the number of revolute joints. For the 6 × 5 array, $n = 30$ and $j = 30$ after slits have been made, resulting in a 24-DoF assembly. The large number of DoFs is not preferred in aerospace applications since many actuators may be required to control the deployment process.

For symmetric HCs, some panels along the plane of symmetry could be merged. Therefore, the DoF of the 6 × 5 array is reduced from 24 to 19 for the design.

Although merging some panels reduces the DoFs of an assembly, the number of DoFs remains high. The deployment of a multi-DoF assembly may be tackled by using spring-loaded hinges in which strain energy is stored while the array is stowed, and its subsequent deployment is driven by releasing the strain energy in the hinges. The design of actuation devices will be detailed in Chapter 4.

3.3 HCs in arrays of regular polygons

3.3.1 HCs in arrays of regular polygons

The use of HC to design arrays consisting of rectangular facets that can be folded compactly prompts us to explore HCs in arrays made of regular polygons. Here we examine the compact foldability of these arrays.

In Euclidean geometry, regular polygons are two-dimensional facets with equal side lengths and equal interior angles (Coxeter, 1973). There are many types of regular polygons. However, only three of them, namely, equilateral triangles, squares, and regular hexagons can tessellate a plane if only one shape is allowed in one tessellation, also known as the regular tessellations (Grünbaum & Shephard, 1986). When regular polygons are used to construct an array, they can always achieve reflection symmetry about their common creases because they are equilateral and equiangular by definition.

Having explored rectangular arrays, in which the square array is a special case, HCs are drawn within several other arrays made from equilateral triangles and regular hexagons as shown in Figure 3.10. The facets on the top and bottom layers of the stacks are shaded in dark grey if the HC leads to a two-stack folded configuration, for instance, the arrays in Figure 3.10(b), (d) and (e). The method to search for the top and bottom layer configuration that is introduced in Section 3.2.1 is also applicable to regular polygons.

Taking the array of ten regular hexagons in Figure 3.10(e) as an example, two HCs can be found as shown in Figure 3.11. A flat surface becomes a loop of hexagons when placing slits and creases according to the path of the HCs, respectively.

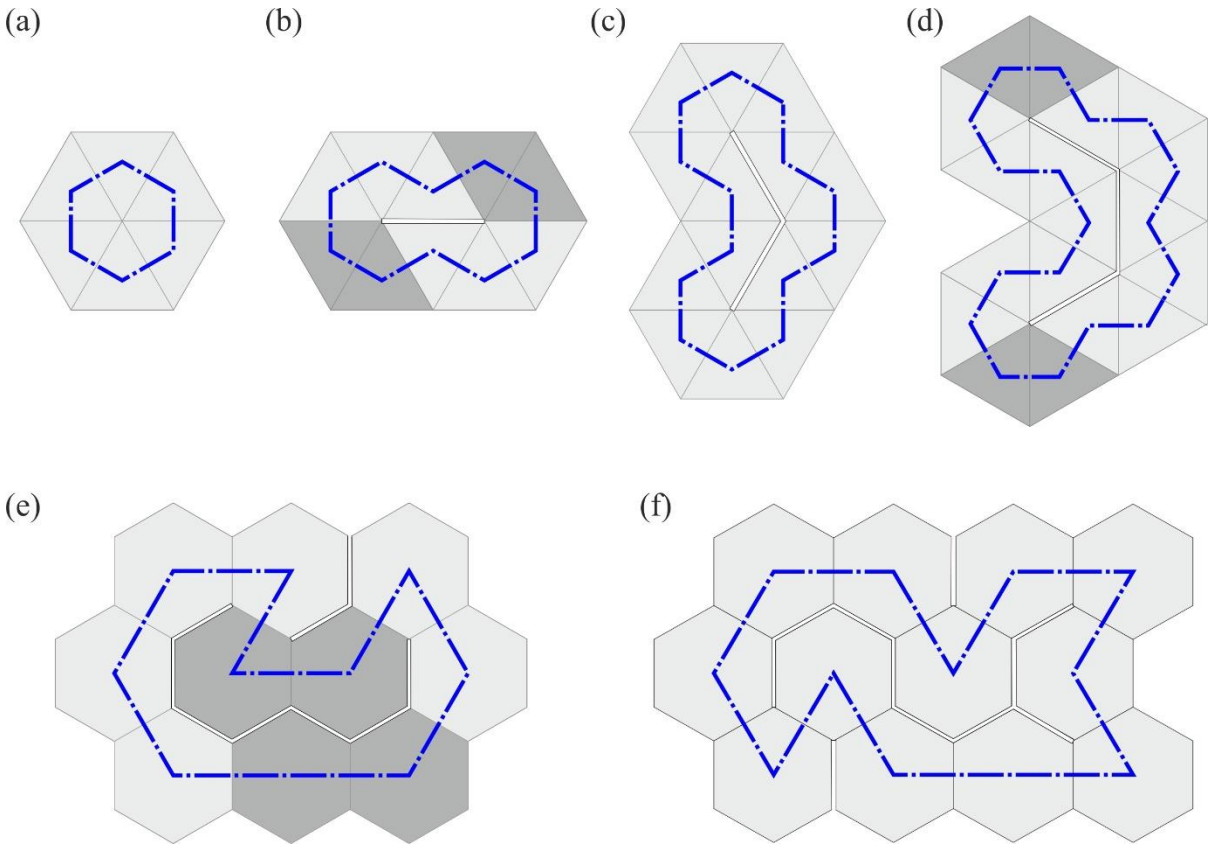

Figure 3.10 HCs are plotted in blue dotted dash lines in arrays of (a)-(d) equilateral triangles, and (e)-(f) regular hexagons. Facets of the top and bottom layers of the stacks are shaded in dark grey if the kirigami pattern can be folded.

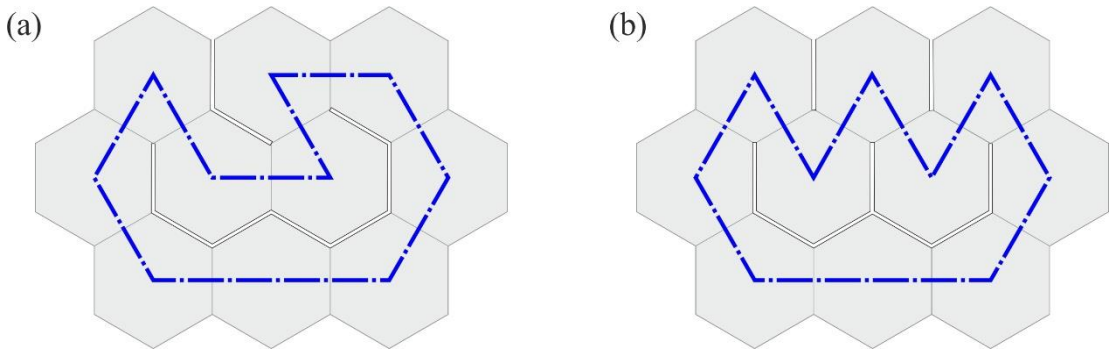

Figure 3.11 Two HCs can be found in an array of ten regular hexagons.

In the first array, the regular hexagons can be labelled as P_i (i = 1, 2, …, n where n = 10), with the one at the top right corner labelled as P_1. The creases that are connecting the hexagons are labelled as e_i in Figure 3.12(a).

We start searching for the crease that is on the outer layer of the folded stacks from the edge e_1. The cut edges that are attached to the two ends of the open chain are denoted as two identical vectors, $\mathbf{e}_1^+$ and $\mathbf{e}_1^-$, which are marked in red in Figure 3.12(b). Vector $\mathbf{e}_1^+$ is reflected about the edges e_2, e_3, e_4 and e_5 in sequential order, with each operation being traced in black arrows. Likewise for the vector $\mathbf{e}_1^-$, the reflection operations are traced by black arrows about the creases e_{10}, e_9, e_8 and e_7 in succession. After four operations, the red vectors do not coincide, indicating that the crease e_1 is on the top layer of the folded stack.

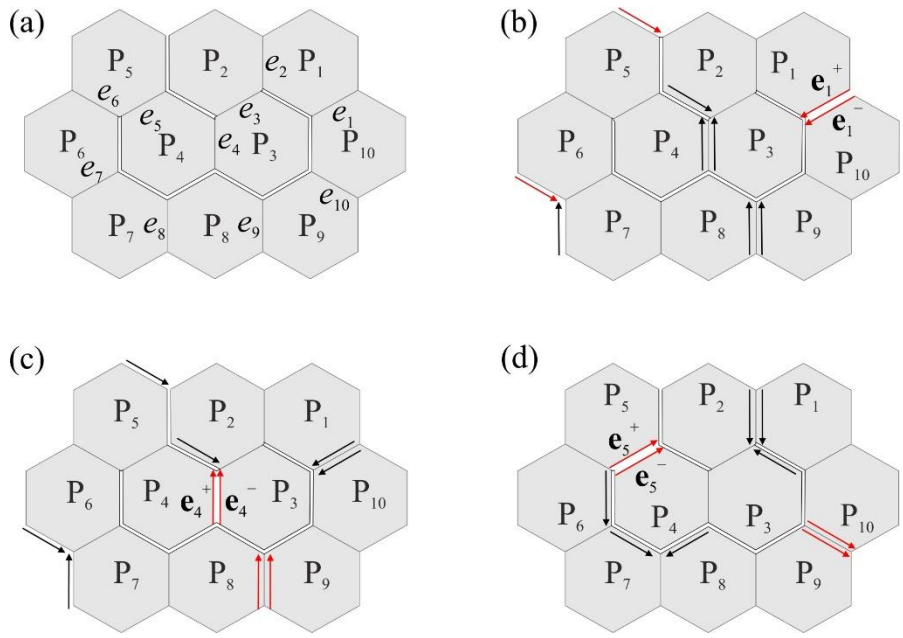

Figure 3.12 Searching for the crease on the outer layer of folded stacks in an array of hexagons. (a) Panels and edges are labelled in the array. (b) The edges $\mathbf{e}_1^+$ and $\mathbf{e}_1^-$ do not satisfy the two-stack foldable criterion. (c) – (d) The edges, $\mathbf{e}_4^+$, $\mathbf{e}_4^-$ and $\mathbf{e}_5^+$, $\mathbf{e}_5^-$ satisfy the two-stacks foldable criterion.

When two vectors $\mathbf{e}_4^+$ and $\mathbf{e}_4^-$ are attached to P_4 and P_3, respectively, they are again marked in red in Figure 3.12(c). After a series of reflection operations, the two red vectors coincide at crease e_9, indicating that the array can be folded in two stacks with the top and bottom layers being polygons P_4, P_3 and P_8, P_9. Likewise, when two vectors $\mathbf{e}_5^+$ and $\mathbf{e}_5^-$ are attached on P_5 and P_4, respectively, the two red vectors coincide at crease e_{10} after a series of reflection operations as shown in Figure 3.12(d). Therefore, two folding sequences are possible for the array of ten regular hexagons. All panels can be folded onto either P_4, P_3 or P_5, P_4. The same method is applied to test the creases in Figure 3.11(b), but no other two-stack foldable configuration can be obtained.

A thick-panel prototype was then made and the two-stack foldability of the array following the folding sequences of Figure 3.12(c) and (d) was validated. In Figure 3.13(a), panels P_3 and P_4 were folded onto P_9 and P_8; and in Figure 3.13(b), panels P_{10} and P_9 were folded onto P_4 and P_5, respectively, with all the other panels sandwiched in-between.

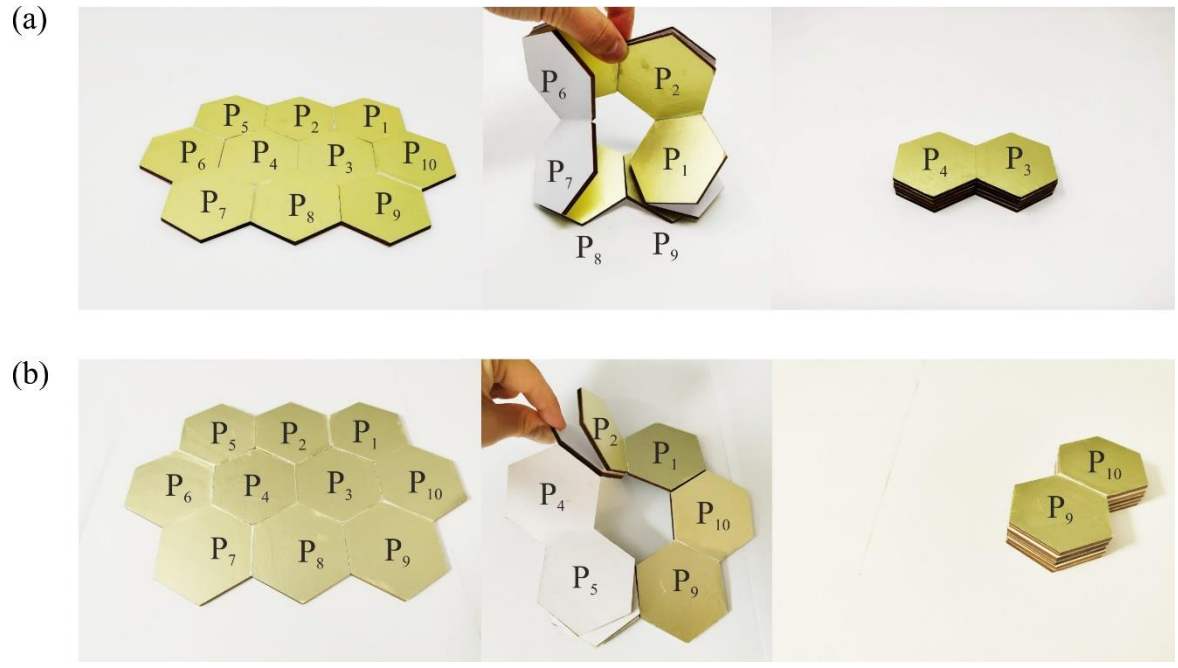

Figure 3.13 A thick-panel prototype demonstrating two folding sequences of the array made from ten hexagons.

3.3.2 The twist of the loop while folding

It was observed that the approach given above may lead to a loop with a twist. To properly design the folding scheme, information on the twist is required.

Having an open chain and connecting the two ends of it with vectors of the same direction, a cylinder can be obtained in Figure 3.14(a). Having the same open chain but connecting its two ends with the vectors of opposite directions, a Möbius strip is obtained, which is a band of half-twist as shown in Figure 3.14(b). Topologically, a cylinder and a Möbius strip are different, but a band with a full twist is homeomorphic to a band with zero twists (Armstrong, 2013). This is because in higher dimensions mathematically, one can cut the band, undo the whole twist, and glue the cut edge back, as long as the two edges are identified in the same direction. However, such homeomorphism cannot be applied to $\mathbb{R}^3$, where a cut cannot be made.

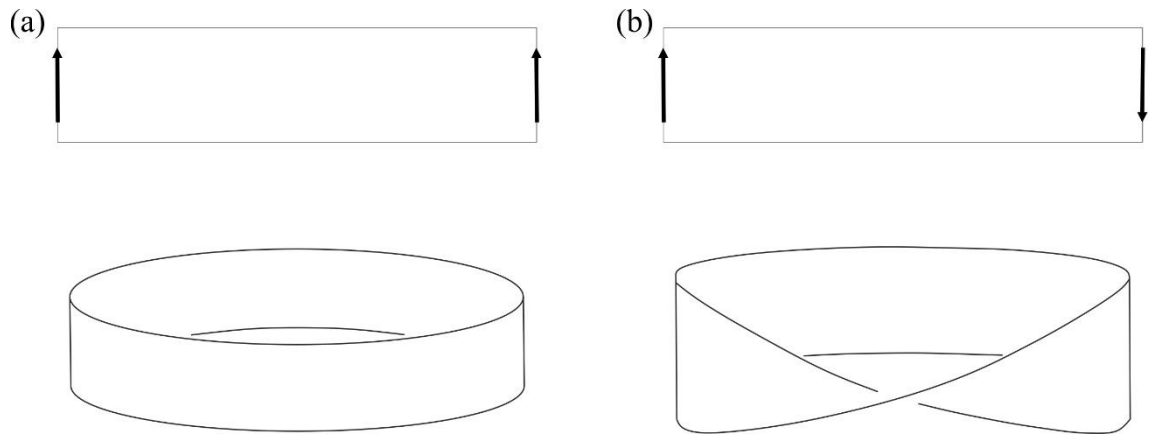

Figure 3.14 (a) A cylinder versus (b) a Möbius strip. The arrows represent the direction of joining the two edges.

All the odd numbers of half-twist can be identified through the reflection operations of the vectors. If, after a series of reflection operations, the cut edges $\mathbf{e}_j^+$ and $\mathbf{e}_j^-$ are of opposite directions, an odd number of half-twist has resulted. However, the geometry of spatial vectors alone is insufficient to express the difference between full twists.

Let us take an array of 12 regular hexagons as an example. Two HCs are plotted in blue dotted dash lines in Figure 3.15, in which Figure 3.15(a) is a replica of Figure 3.10(f). Slits are made accordingly.

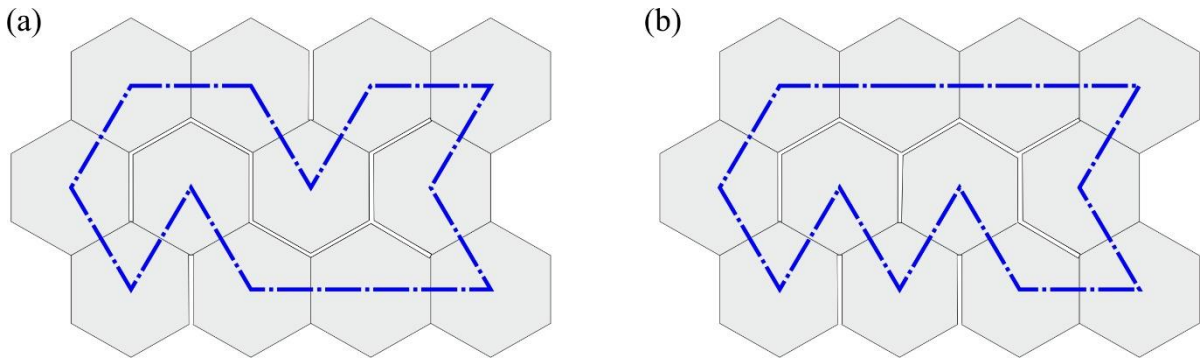

Figure 3.15 Two HCs are drawn in an array of 12 hexagons, marked by dotted dash lines.

Starting from the polygon on the top right corner of the array, the polygons are labelled along the loop. So are the creases, as detailed in Figure 3.16(a). Applying the method that is introduced in the previous sections, the vectors $\mathbf{e}_6^+$ and $\mathbf{e}_6^-$ coincide after five reflection operations, as traced by the black arrows in Figure 3.16(b). By the method, the polygons P_5 and P_6 should be able to fold onto P_{12} and P_{11}, respectively.

However, when the design was validated by a physical model as shown in Figure 3.16(c)-(d), a full twist of 2π is found and cannot be resolved. As a result, a two-stack foldable configuration cannot be achieved. In this example, the prototype was made with thin cards instead of thick panels to better demonstrate the twist in the folding process. If a twist in the card model is inevitable, it is also not resolvable in the thick-panel model as more constraints will be imposed for a loop of rigid panels than flexible paper. So far, it is not clear whether a twist is embedded in a kirigami pattern unless the pattern is verified by making a card model or a thick-panel model. It is therefore necessary to experimentally validate the results obtained by reflection operations.

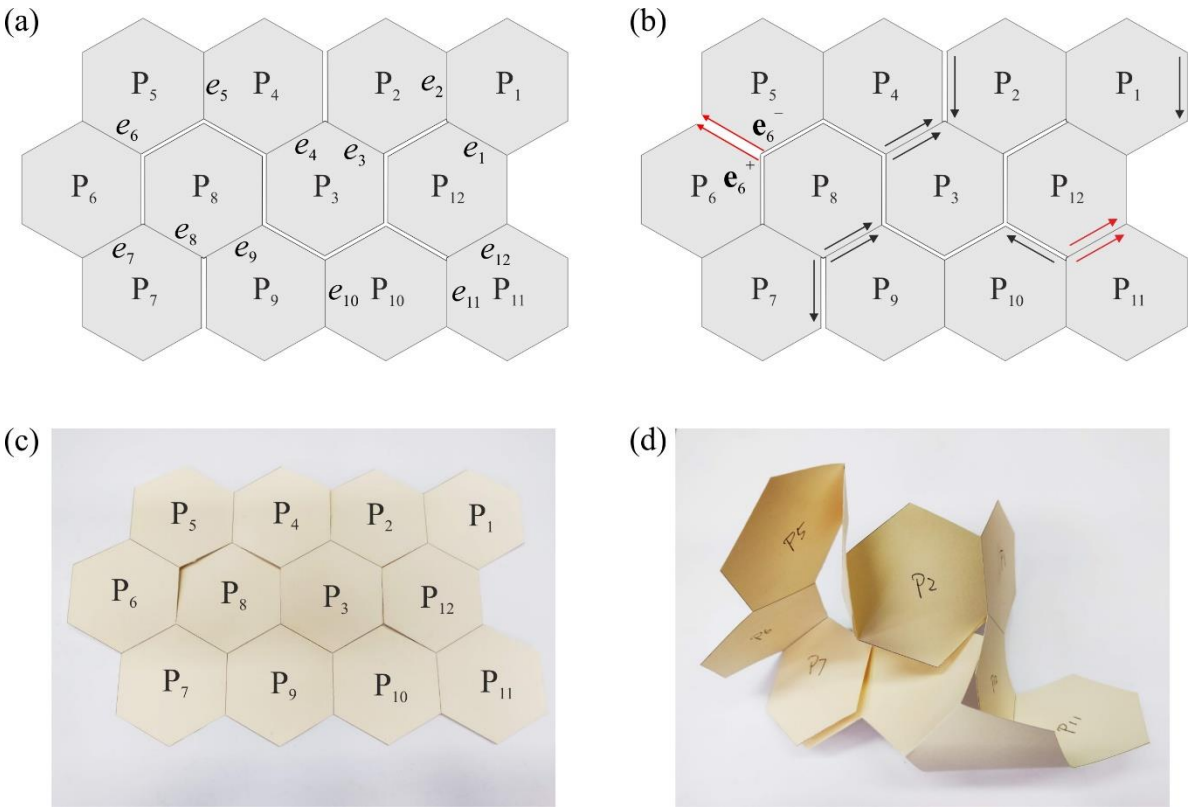

Figure 3.16 A twist cannot be resolved in the folding process of an array of 12 hexagons. (a) Polygons and creases are labelled. (b) $\mathbf{e}_6^+$ and $\mathbf{e}_6^-$ coincide after reflection operations. (c) A thin card model when it is flattened. (d) A twist is found during the folding process.

No other creases in Figure 3.16(a) satisfy the two-stack foldable criterion through reflection operations, and neither do any creases as shown in Figure 3.15(b). Therefore, the array of 12 regular hexagons cannot be folded into two stacks.

3.4 Conclusion

The Hamiltonian Circuit approach introduced in this chapter enables a flat surface of finite thickness to be folded into stacks without any voids. In an array of identical polygons, slits are made to facilitate compact folding. The approach is successfully validated through physical prototypes.

For arrays consisting of *n* identical regular polygons, HCs are drawn to identify the placements of revolute joints and slits. A slit is introduced along an edge if the edge is not crossed by the path of the HC, and a revolute joint is placed to connect two panels otherwise.

It is sometimes not obvious if the slit arrangements can result in two-stack foldable configurations. A method was then introduced to select the useful HCs by searching the creases on the top and bottom layers of the folded stacks. By cutting the loop of polygons open, the problem of folding a two-dimensional flat sheet is transformed into the z-folding of a one-dimensional chain of polygons. Although the axes of the creases are not necessarily arranged in parallel, deciding if an open chain can be folded into two stacks in parity is easier than folding a loop. However, the information about the twist of the loop will be missing if the loop is cut open and re-joined afterwards. It is still an open problem to identify the 3D twist from the 2D kirigami pattern without cutting the loop open. Card models need to be made to validate the design.

Given the non-uniqueness of HCs in some arrays, a multiple-DoF assembly is usually obtained when a feasible stacking strategy can be found. Sometimes, the number of DoFs can be slightly reduced by merging plates along the plane of symmetry of an array if folding along a symmetric HC.

CHAPTER 4

COLLISION-FREE DEPLOYMENT OF AN ASSEMBLY WITH MULTIPLE DOFS

A folding scheme based on the Hamiltonian circuit was devised in Chapter 3 to fold a chessboard-like array into a compact package without any voids. Since this approach leads to a multiple-DoF assembly, many deployment paths have resulted and some of them lead to collisions. Spring-loaded hinges can be used to synchronise the deployment with their zero-strain positions coinciding with the fully deployable configuration of the array. The deployment is passively driven by releasing the elastic energy stored within the springs during folding. Since there is no controlling mechanism once the deployment starts, the stiffness of spring-loaded hinges must be chosen carefully to avoid any collision amongst panels during the deployment. Linear torsional springs with various stiffnesses are employed at different hinge locations, which provide great potential in realising a collision-free bi-directional deployment. This is ensured by carrying out an optimisation process that includes both dynamic modelling of the deployment process and collision detection. Finally, the collision-free deployment is validated by experiments. Though the deployment of an array of rectangular panels is demonstrated, this approach can be extended to deployable arrays of any regular geometries.

4.1 Dynamics modelling of a multi-DoF assembly

4.1.1 Forming a kinematic chain

A closed-loop kinematic chain has resulted when placing revolute joints according to an HC that is planned within a rectangular array. An example of a 4 × 4 array is considered, with all the panels represented by green rectangles and labelled in Figure 4.1(a). A symmetrical HC is drawn within the array, and the revolute joints are placed on the edges where the path of the HC crosses from one panel to another in Figure 4.1(b). The panels along the plane of symmetry of the HC can be merged into bigger ones to reduce the overall number of DoFs in the assembly as demonstrated in Figure 4.1(c). Meanwhile, the closed-loop kinematic chain turns into a combination of a closed chain and an open chain.

The number of the DoFs for this spatial linkage is six according to the Kutzbach criterion. Conventionally, at least six actuators are required to control the deployment of such a system. It is however possible to synchronise the motions of the panels using spring-loaded torsional hinges that are strain-free when the array is fully deployed.

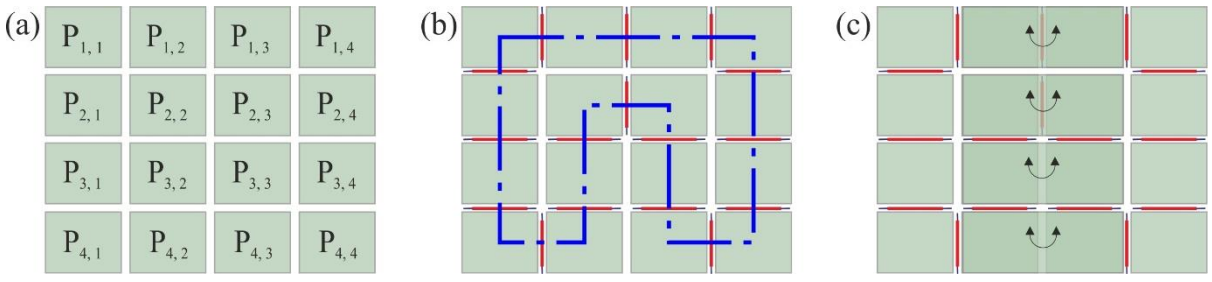

Figure 4.1 Formation of a 4 × 4 rectangular array. (a) Panels are labelled in the array. (b) An HC is plotted by blue dotted dash lines and revolute joints are denoted by red lines. (c) Panels on the middle two columns of the array can be merged to form four larger panels that are twice the size of the original ones.

4.1.2 Topology of the multibody assembly

The topological graph of such an assembly can be represented as a closed loop with an open chain attached as shown in Figure 4.2(a), where a black dot represents a panel and a line represents a revolute joint with a single DoF.

First, the panels are labelled in the topological graph. Starting from the one that is fixed to a rigid support such as the main body of a satellite, labelled as panel 0, the numbering increases clockwise until it reaches panel 5, where there are two paths ahead. Selecting the one that results in the longest open chain in the assembly, the numbering continues until the last panel in the open chain is reached, in this case, panel 7. After that, the second path is visited and the numbering continues until all the panels in the assembly are labelled.

Secondly, the revolute joints that are used to connect the panels are labelled. The joint that is connecting panel i to the assembly is labelled as joint ⓘ. For instance, the one that is connecting panel 1 to the assembly is labelled as joint ①.

When a closed chain exists in the system, the number of DoF is less than the number of hinges, indicating that the motion of panel i is not only a superposition of its previous panels but also its next panel in the closed chain. In this chapter, the penalty spring method (Wang et al., 2002) is adopted to replace some of the constraints in a closed chain. For instance, the joint between panels 5 and 8 is superficially removed in Figure 4.2(b), turning the topological representation into two open chains. Originating from panel 0, the numbering of the panels and joints in one chain increases clockwise as before; whereas in the second open chain, the panels are re-labelled as c1, c2, c3 and c4 as the chain goes counter-clockwise, and the joints that are connecting the panels are labelled as ⓒ①, ⓒ②, ⓒ③ and ⓒ④, respectively.

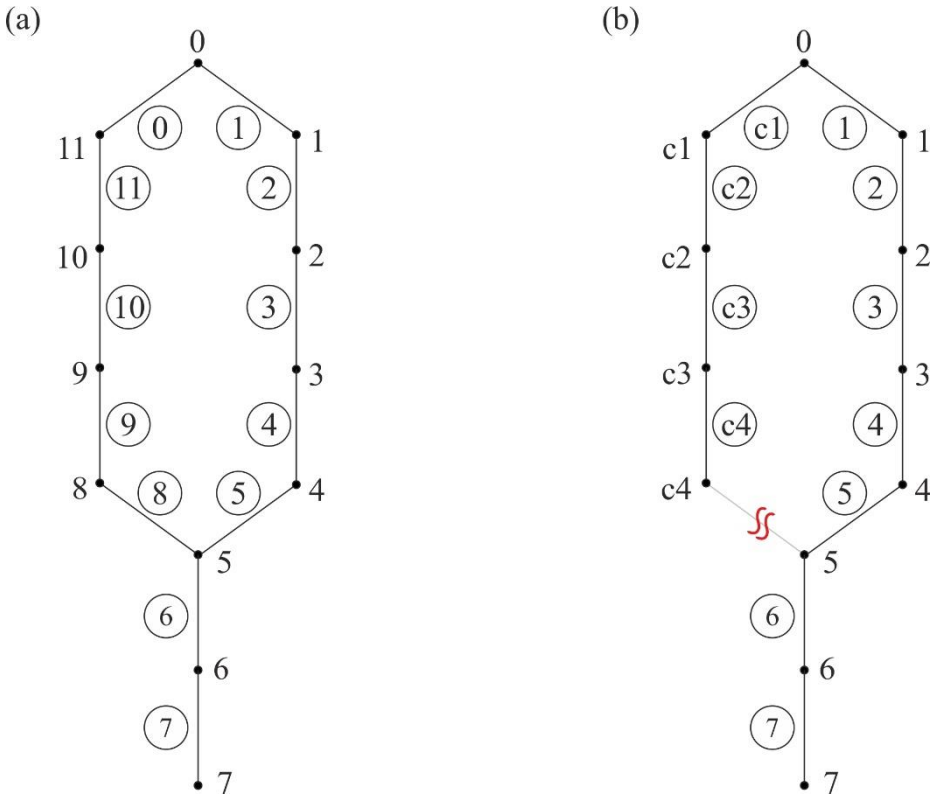

Figure 4.2 A topological representation of the 4 × 4 array. (a) Topological graph of a closed chain with an open chain attached. (b) A hinge is removed as denoted by the red double curves, resulting in two open chains.

The removed hinge is referred to as the cut hinge hereafter. To make the open chains equivalent to the original one, translational springs with very high stiffness are placed at the cut hinge. The modelling of a cut hinge will be detailed in Section 4.2.2.

4.1.3 Defining body-attached frames

The deployment of the multibody assembly must be modelled using rigid-body dynamics. According to the topological graph described in Figure 4.2(b), a partially deployed assembly consisting of 12 rectangular panels and 11 joints is shown in Figure 4.3.

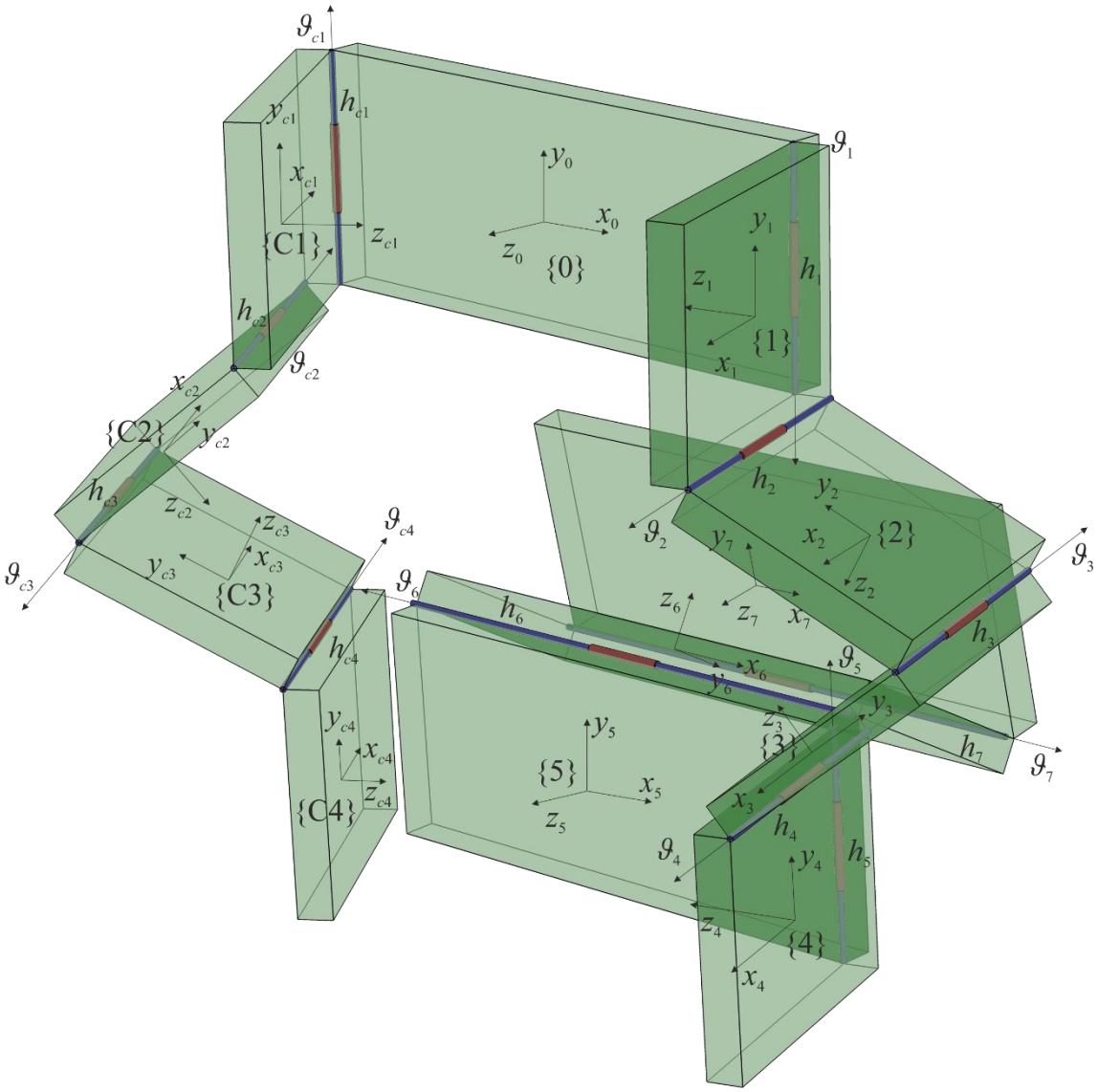

Figure 4.3 Body-attached frames and joint coordinates are labelled on a partially folded system.

A body-attached frame $\{i\}$ is fixed on panel i with its origin being the centroid of the panel and its axes x_i, y_i and z_i being oriented along the length, width and thickness direction of the panel, respectively. In the fully deployed configuration, the z_i axes of all body-attached frames will point in the same direction.

Connecting the panels, joints are placed on either the top or the bottom facets of the panels constraining the motion between two consecutive body-attached frames. A rotational

coordinate ϑ_i is introduced along each joint h_i, allowing only the rotational DoF of panel i with respect to its predecessor panel $i-1$. Note that $0 \leq \vartheta_i \leq \pi$, with $\vartheta_i = 0$ and π representing the fully deployed and fully folded configurations, respectively.

Likewise, a body-attached frame {Ci} is attached on the centroid of panel ci, and a rotational coordinate ϑ_{ci} is placed along the joint h_{ci}.

4.1.4 Configurations of the body-attached frames

Since panel 0 is fixed onto a satellite that is floating in space, it can be assumed to be connected to the fixed world frame via a floating joint – a joint that allows six DoFs (Nikravesh, 2008). The dynamics simulation can be made more realistic if the action-reaction force between the solar panels and the main body of the satellite is known. However, the prerequisite of setting up a floating joint is knowing the dimensions and the weight of the satellite. To demonstrate the deployment of solar panels from stacks to a flat surface as a stand-alone system, it is conveniently assumed that panel 0 is grounded.

The posture of the panel i can be described by a 3 × 1 translational vector $\mathbf{p}_i^0$ and a 3 × 3 rotation matrix $\mathbf{R}_i^0$, which represent the position of the origin and the orientation of its body-attached frame $\{i\}$, with respect to the fixed frame $\{0\}$, respectively.

The rotation matrix $\mathbf{R}_i^0$ can be obtained via the dot product of a series of rotations,

$$\mathbf{R}_i^0 = \mathbf{R}_1^0 \mathbf{R}_2^1 ... \mathbf{R}_i^{i-1} \tag{4.1}$$

where $\mathbf{R}_i^{i-1}$ is the rotation matrix from the body-attached frame $\{i-1\}$ to $\{i\}$, expressed in frame $\{i-1\}$, which is due to the angle of rotation ϑ_i along hinge h_i. In an assembly of rectangular panels, rotational hinges are placed along the length or the width direction of a panel. When

the rotating axis h_i is parallel to the length direction, it is parallel to $\pm x_{i-1}$ of the predecessor's body-attached frame. Furthermore, if the hinge is placed on the bottom facet of two panels $i-1$ and i, the rotation of frame $\{i\}$ is along x_{i-1} axis, hence the positive angle of rotation ϑ_i is used for the calculation of the rotation matrix. If on the other hand, the hinge is placed on the top facet, a negative angle of rotation $-\vartheta_i$ will be used. To summarise, the rotation matrix $\mathbf{R}_i^{i-1}$ is calculated as $\mathbf{R}_x$ in Eqn. (4.2a) when the hinge is placed parallel to the length direction of the panel. Likewise, $\mathbf{R}_i^{i-1} = \mathbf{R}_y$ as shown in Eqn. (4.2b) if h_i is parallel to the width direction of its predecessor panel.

$$\mathbf{R}_x = \mathrm{Rot}(x_{i-1},\, y_{i-1},\, z_{i-1},\, \pm\vartheta_i,\, 0,\, 0) = \begin{bmatrix} 1 & 0 & 0 \\ 0 & \cos(\pm\vartheta_i) & -\sin(\pm\vartheta_i) \\ 0 & \sin(\pm\vartheta_i) & \cos(\pm\vartheta_i) \end{bmatrix} \tag{4.2a}$$

$$\mathbf{R}_y = \mathrm{Rot}(x_{i-1},\, y_{i-1},\, z_{i-1},\, 0,\, \pm\vartheta_i,\, 0) = \begin{bmatrix} \cos(\pm\vartheta_i) & 0 & \sin(\pm\vartheta_i) \\ 0 & 1 & 0 \\ -\sin(\pm\vartheta_i) & 0 & \cos(\pm\vartheta_i) \end{bmatrix} \tag{4.2b}$$

The translational vector $\mathbf{p}_i^0$ can be obtained by adding a series of translational vectors. According to a graphical vector representation in Figure 4.4,

$$\mathbf{p}_i^0 = \mathbf{p}_{i-1}^0 + \mathbf{p}_{hi}^0 \tag{4.3}$$

$$\text{and} \quad \mathbf{p}_{hi}^0 = \mathbf{p}_{i-1}^0 + \mathbf{r}_{i-1,\,hi}^0 \tag{4.4}$$

where $\mathbf{p}_{hi}^0$ is a vector from the fixed frame $\{0\}$ to the mid-point of the rotational hinge h_i, $\mathbf{r}_{i-1,\,hi}^0$ is a vector from the origin of the body-attached frame $\{i-1\}$ to the mid-point of h_i, and $\mathbf{r}_{hi,\,i}^0$ is a vector from the mid-point of h_i to the origin of the body-attached frame $\{i\}$. All vectors are expressed in the fixed frame $\{0\}$.

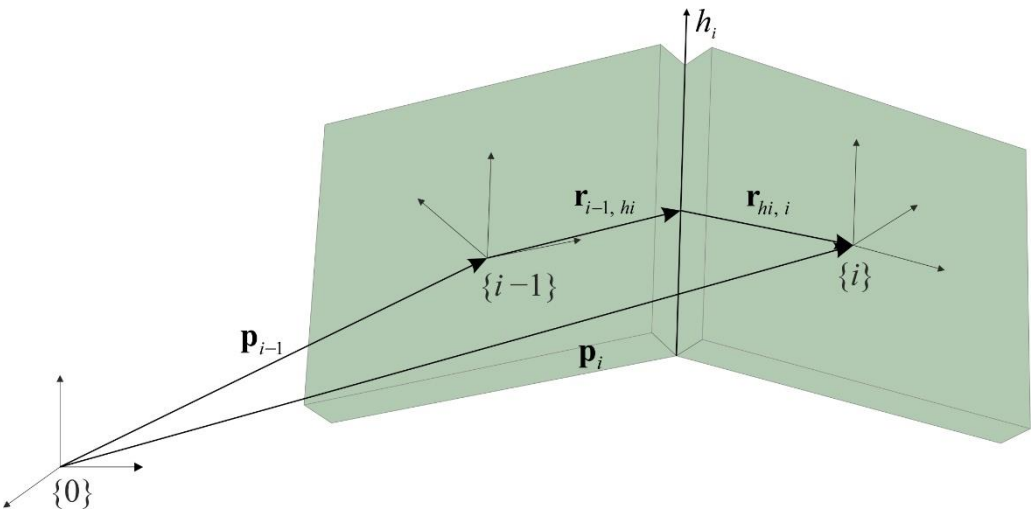

Figure 4.4 Locating the body-attached frames in the world frame.

The vectors $\mathbf{r}^0_{i-1,\,hi}$ and $\mathbf{r}^0_{hi,\,i}$ are changing with respect to the change of ϑ_i (i = 1, 2, …, n) in the assembly when expressing in the fixed frame {0}. Expressing the two vectors in their corresponding body-attached frames, $\mathbf{r}^{i-1}_{i-1,\,hi}$ and $\mathbf{r}^{i}_{hi,\,i}$ become two vectors that only depend on the geometry of a panel regardless of its orientation and position in space. Eqn. (4.3) and (4.4) can be re-written as

$$\mathbf{p}^0_i = \mathbf{p}^0_{hi} + \mathbf{R}^0_i \mathbf{r}^i_{hi,\,i} \tag{4.5}$$

$$\text{and } \mathbf{p}^0_{hi} = \mathbf{p}^0_{i-1} + \mathbf{R}^0_{i-1} \mathbf{r}^{i-1}_{i-1,\,hi} \tag{4.6}$$

4.1.5 Velocities and accelerations

Let $\boldsymbol{\omega}^0_i$ and $\boldsymbol{\omega}^0_{i-1}$ denote the angular velocity of the body-attached frame $\{i\}$ and that of $\{i-1\}$, expressed in the fixed frame {0}, respectively. Furthermore, let $\boldsymbol{\omega}^{i-1}_i$ represent the angular velocity of body i due to the rotation of hinge i, expressed relative to frame $\{i-1\}$. The angular velocity of body-attached frame $\{i\}$ equals that of $\{i-1\}$ plus the rotation induced along the hinge line h_i.

$$\boldsymbol{\omega}_i^0 = \boldsymbol{\omega}_{i-1}^0 + \mathbf{R}_{i-1}^0 \boldsymbol{\omega}_i^{i-1} \tag{4.7}$$

where the angular velocity induced along the hinge h_i is

$$\boldsymbol{\omega}_i^{i-1} = \dot{\vartheta}_i \vec{k} \tag{4.8}$$

with $\vec{k}$ being a vector representing the axis of rotation along hinge h_i, expressed in frame $\{i-1\}$.

If expressing the angular velocity in its own frame $\{i\}$, and taking care to account for the fact that the angular velocities are expressed in different frames.

$$\boldsymbol{\omega}_i = (\mathbf{R}_{(i-1)i})^{\mathrm{T}} \boldsymbol{\omega}_{i-1} + (\mathbf{R}_{(i-1)i})^{\mathrm{T}} \dot{\vartheta}_i \vec{k} \tag{4.9}$$

where $\boldsymbol{\omega}_i$ and $\boldsymbol{\omega}_{i-1}$ denoting angular velocities of frames $\{i\}$ and $\{i-1\}$, expressed in their own frames, respectively.

Further, the angular acceleration of body-attached frame $\{i\}$ with respect to the fixed frame $\{0\}$ can be obtained via time differentiation of Eqn. (4.9), which gives

$$\dot{\boldsymbol{\omega}}_i^0 = \dot{\boldsymbol{\omega}}_{i-1}^0 + \mathbf{R}_{i-1}^0 \ddot{\vartheta}_i \vec{k} + \boldsymbol{\omega}_{i-1}^0 \times \dot{\vartheta}_i \vec{k} \tag{4.10}$$

Similarly, let $\boldsymbol{\alpha}_i$ and $\boldsymbol{\alpha}_{i-1}$ denote the time derivatives of the angular velocity of frames $\{i\}$ and $\{i-1\}$, expressed in their own frame, respectively.

$$\boldsymbol{\alpha}_i = (\mathbf{R}_i^0)^{\mathrm{T}} \dot{\boldsymbol{\omega}}_i^0 \tag{4.11}$$

It is not true that $\boldsymbol{\alpha}_i = \dot{\boldsymbol{\omega}}_i$ because both frames $\{i\}$ and $\{i-1\}$ are rotating frames. Eqn. (4.11) can be expressed in the body-attached frame $\{i\}$,

$$\boldsymbol{\alpha}_i = (\mathbf{R}_i^{i-1})^{\mathrm{T}} (\boldsymbol{\alpha}_{i-1} + \ddot{\vartheta}_i \vec{k} + \dot{\vartheta}_i \boldsymbol{\omega}_{i-1} \times \vec{k}) \tag{4.12}$$

Furthermore, let $\mathbf{v}_i^0$, $\mathbf{v}_{hi}^0$ and $\mathbf{a}_i^0$, $\mathbf{a}_{hi}^0$ denote the linear velocity and linear acceleration of the origin of frame $\{i\}$ and the mid-point of hinge h_i, respectively. All vectors are expressed in the fixed

frame $\{0\}$. The linear velocity $\mathbf{v}_i^0$ is obtained by taking the time differentiation of Eqn. (4.3), knowing that $\mathbf{r}_{i-1,\,hi}^0 = \mathbf{R}_{i-1}^0 \mathbf{r}_{i-1,\,hi}^{i-1}$ and $\mathbf{r}_{hi,\,i}^0 = \mathbf{R}_i^0 \mathbf{r}_{hi,\,i}^i$.

$$\mathbf{v}_i^0 = \dot{\mathbf{p}}_i^0 = \mathbf{v}_{i-1}^0 + \boldsymbol{\omega}_{i-1}^0 \times \mathbf{r}_{i-1,\,hi}^0 + \boldsymbol{\omega}_i^0 \times \mathbf{r}_{hi,\,i}^0 \tag{4.13}$$

Further, by taking the time derivative of linear velocities, one can obtain

$$\mathbf{a}_i^0 = \dot{\mathbf{v}}_i^0 = \mathbf{a}_{hi}^0 + \dot{\boldsymbol{\omega}}_i^0 \times \mathbf{r}_{hi,\,i}^0 + \boldsymbol{\omega}_i^0 \times (\boldsymbol{\omega}_i^0 \times \mathbf{r}_{hi,\,i}^0) \tag{4.14}$$

$$\text{and } \mathbf{a}_{hi}^0 = \dot{\mathbf{v}}_{hi}^0 = \mathbf{a}_{i-1}^0 + \dot{\boldsymbol{\omega}}_{i-1}^0 \times \mathbf{r}_{i-1,\,hi}^0 + \boldsymbol{\omega}_{i-1}^0 \times (\boldsymbol{\omega}_{i-1}^0 \times \mathbf{r}_{i-1,\,hi}^0) \tag{4.15}$$

If again, the linear acceleration is expressed in its own body-attached frames, with $\mathbf{a}_i$ denoting linear acceleration of the origin of frames $\{i\}$ with respect to its own frame, and $\mathbf{a}_{hi}^{i-1}$ denoting the linear acceleration of the mid-point of hinge h_i with respect to frame $\{i-1\}$.

$$\mathbf{a}_i = (\mathbf{R}_{(i-1)i})^{\mathrm{T}} \mathbf{a}_{hi}^{i-1} + \dot{\boldsymbol{\omega}}_i \times \mathbf{r}_{hi,\,i}^i + \boldsymbol{\omega}_i \times (\boldsymbol{\omega}_i \times \mathbf{r}_{hi,\,i}^i) \tag{4.16}$$

$$\text{and } \mathbf{a}_{hi}^{i-1} = \mathbf{a}_{i-1} + \dot{\boldsymbol{\omega}}_{i-1} \times \mathbf{r}_{i-1,\,hi}^{i-1} + \boldsymbol{\omega}_{i-1} \times (\boldsymbol{\omega}_{i-1} \times \mathbf{r}_{i-1,\,hi}^{i-1}) \tag{4.17}$$

4.1.6 Equations of motion

Now, if torsional springs are placed along the revolute joints, elastic force and torque stored in the springs will be applied to the rigid bodies. The Newton-Euler mechanics states that the rate of change of the linear momentum equals the total force applied to the body, and the rate of change of the angular momentum equals the torque applied to the body, from which comes the famous relationship

$$\sum \mathbf{f}^i = m_i \mathbf{a}_i\,, \tag{4.18}$$

$$\sum \boldsymbol{\tau}^i = I_i \boldsymbol{\alpha}_i + \boldsymbol{\omega}_i \times (I_i \boldsymbol{\omega}_i) \tag{4.19}$$

where $\sum \mathbf{f}^i$ and $\sum \boldsymbol{\tau}^i$ denote the total force and the total torque applied on the panel i; m_i and I_i are the mass of panel i and its constant moment of inertia with respect to its body-attached frame $\{i\}$, respectively. $\boldsymbol{\omega}_i$ denotes the angular velocity of frame $\{i\}$. The linear and angular accelerations of the origin of frame $\{i\}$ with respect to its own frame are denoted as $\mathbf{a}_i$ and $\boldsymbol{\alpha}_i$, respectively. All terms are expressed in the body-attached frame $\{i\}$ (Featherstone, 2008; Spong et al., 2004).

4.2 Modelling the hinge elements

4.2.1 Torque at the elastic hinges

Along each joint h_i, a torsional spring with constant stiffness k_i is placed to resist the angle of rotation ϑ_i. In the stowed configuration, each spring is pre-stressed with $\vartheta_i = \pi$, driving the deployment of the assembly, indicating a non-zero initial torque along each hinge.

Within the permissible range of motion $0 \leq \vartheta_i \leq \pi$, the resultant magnitude of torque due to the torsional spring at the hinge h_i can be written as

$$\tau_i = -k_i \vartheta_i + \tau_i(\dot{\vartheta}) \tag{4.20}$$

where $\tau_i(\dot{\vartheta})$ is the magnitude of torque resulting from viscous damping along h_i.

The energy loss along a hinge depends on many factors such as the spring chosen, how the spring is connected to the panels, etc. It can be non-linear (Li et al., 2013; Li et al., 2021) if a clearance joint is used. However, in an elastic-hinge setup that was similar to that of this paper (Santoni, 2015), it was verified that the viscous damping effect was a predominant source of energy dissipation. Thus, it is conveniently assumed that $\tau_i(\dot{\vartheta})$ is linearly proportional to and opposing the angular velocity $\dot{\vartheta}_i$ at the hinge.

$$\tau_i(\dot{\vartheta}) = -c_i \dot{\vartheta}_i \tag{4.21}$$

where c_i and $\dot{\vartheta}_i$ are the damping coefficient and the magnitude of the angular velocity of the spring along hinge h_i.

Hence, the torsional spring and the damper contribute to modelling the toque along each hinge. When ϑ_i goes beyond the permissible range of motion, contact occurs between the side facets of the neighbouring panels i and $i-1$, illustrated by the orange facets in Figure 4.5.

To avoid penetration, the contact between the two side facets is modelled by a stiff torsional spring with spring stiffness k_s, which is much greater than k_i, and a damping coefficient c_s. The overall magnitude of torque τ_i is summarised as

$$\tau_i = \begin{cases} -k_s(\vartheta_i - \pi) - c_s\omega_i - c_i\omega_i & \text{if } \vartheta_i > \pi \\ -k_i\vartheta_i - c_i\omega_i & \text{if } 0 \le \vartheta_i \le \pi \\ -k_s\vartheta_i - c_s\omega_i - c_i\omega_i & \text{if } \vartheta_i < 0 \end{cases} \tag{4.22}$$

It is apparent that the contact spring and dampers k_s, c_s are only active when contact amongst panels i and i – 1 occurs, i.e., $\vartheta_i > \pi$ or $\vartheta_i < 0$. More specifically, we set k_s to only allow penetrations of panels of no more than 0.1% of their length, while c_s is set based on the material properties of the panels, shear modulus, and density in particular. When ϑ_i goes beyond the permissible range, the contact elements act in parallel with the torsional spring, which provides a nominal torque as elaborated in Eqn. (4.22). However, while the contact is engaged within the aforementioned penetration range, it dominates the response.

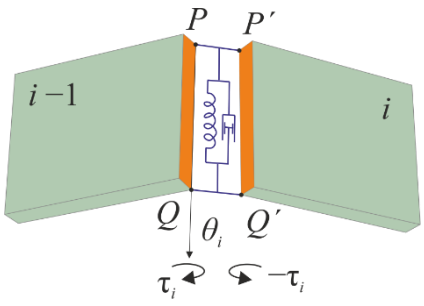

Figure 4.5 Modelling an elastic hinge that connects consecutive panels.

4.2.2 Force at the cut hinge

In Section 4.1.2, a hinge is superficially removed from the closed chain between panels i and $i+m+1$, turning the topological representation into two open branches rooted in panel 0. The last body in each branch is, therefore, free to move in the space. Additional constraints must be applied to the cut hinge to eliminate the extra degrees of freedom in this assembly and to make the open branches equivalent to the behaviour of a closed loop before the cut is made.

As demonstrated in Figure 4.6, MN and M′N′ denote two edges of the cut hinge on the left and right rigid panels. A reference frame {M} originates at M, with x_M, y_M and z_M along the length, width and thickness direction of the panel, respectively. Another reference frame {N} with the same orientation is set at point N. Likewise, reference frames {M'} and {N'} are set up at M' and N'. Five sets of virtual translational elastic springs with zero rest length and dampers are used to connect M with M′ and N with N′ along x_M, y_M, z_M, x_N and z_N, respectively. Each set of spring and damper at the cut hinge has the same spring stiffness k_{ch} and damping coefficient c_{ch}. The stiffness of these virtual springs k_{ch} is sufficiently large so that once a small distance between M and M′, or N and N′, appears, large restoring forces will be generated by the translational springs, bringing the distance back to zero. The restoring force between M and M′ can be calculated as

$$\mathbf{f}_{\mathrm{M}} = -k_{ch}\Delta\mathbf{p}_{\mathrm{MM'}} - c_{ch}\Delta\dot{\mathbf{p}}_{\mathrm{MM'}} \tag{4.23}$$

where $\Delta\mathbf{p}_{\mathrm{MM'}}$ is a vector between the origin of frames {M} and {M'}, $\Delta\dot{\mathbf{p}}_{\mathrm{MM'}}$ is the time rate of change of the origin of the two frames. The stiffness k_{ch} is pre-defined to ensure that the separation between M with M′ is negligible in comparison to the motion-of-interest during the deployment process, yet the system is not too stiff to cause integration errors. A sufficient damping coefficient c_{M} is chosen so that the oscillations of the translational springs are attenuated. Likewise for points N with N′. As such, five DoFs are practically constrained along the axis of the cut hinge, three translational DoFs and two rotational DoFs, left with the only rotational DoF about the hinge MN. Along the active rotational DoF, a pre-stressed torsional spring and a damper with properties as described in Eqn. (4.22) are modelled to rotate about MN.

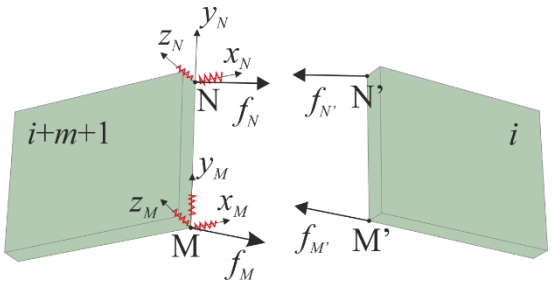

Figure 4.6 Elements at the cut hinge (dampers are not shown).

This system is implemented in Simscape, which uses a force-based Newtonian formulation (MathWorks, R2019b; Miller, 2020). The time integration of the equation of motion is achieved via an explicit variable time-stepping Runge-Kutta (2, 3) pair (Bogacki & Shampine, 1989). A smaller increment in the time step is applied if the configuration is close to the singularity of the system. A Runge-Kutta (2, 3) pair is chosen instead of Runge-Kutta (4, 5) pair for it is more computationally efficient at a given tolerance (Shampine & Reichelt, 1997).

4.3 Collision detection

At this point, one should separate the "contacts" occurring when the values of ϑ_i across 0 or π, from all the other collisions. The former category of contact is not referred to as collision, and it is inevitable in this system. The latter is referred to as collisions, which is the focus of this section. Such collisions are more critical than the "contacts" because they can occur between the edges of a panel and any point on the surface of another panel leading to damage to the structure. It is important to point out that in this work, the dynamic model outlined earlier allows penetration amongst panels that are not connected by hinges. A collision detection method is therefore implemented to detect whether collisions take place and further, it discards the dynamic modelling results after the first collision.

As rigid panels are convex polytopes, the configurations of any two panels can be represented by two sets U and W containing their corresponding coordinates of vertices. The relative translations between the two convex polytopes can then be calculated. The set of translations that could cause interference between the two polytopes forms a new convex polytope, which is known as the Minkowski Difference (MD) of the two convex polytopes U and W (Ericson, 2005; Gilbert et al., 1988). MD is a binary operation that subtracts all the points in W from those in U. The operation is detailed as follows.

$$U \oplus (-W) = \{u - w | u \in U, w \in W\} \tag{4.24}$$

Figure 4.7 provides a visualisation of this operation in 2D. Two convex polygons, a rectangle and a triangle are in Euclidean space. They are not touching each other in Figure 4.7(a). The MD is calculated as the region swept by the rectangle translated to every point negated in the triangle. Figure 4.7(b) shows the obtained geometry, which does not contain the origin.

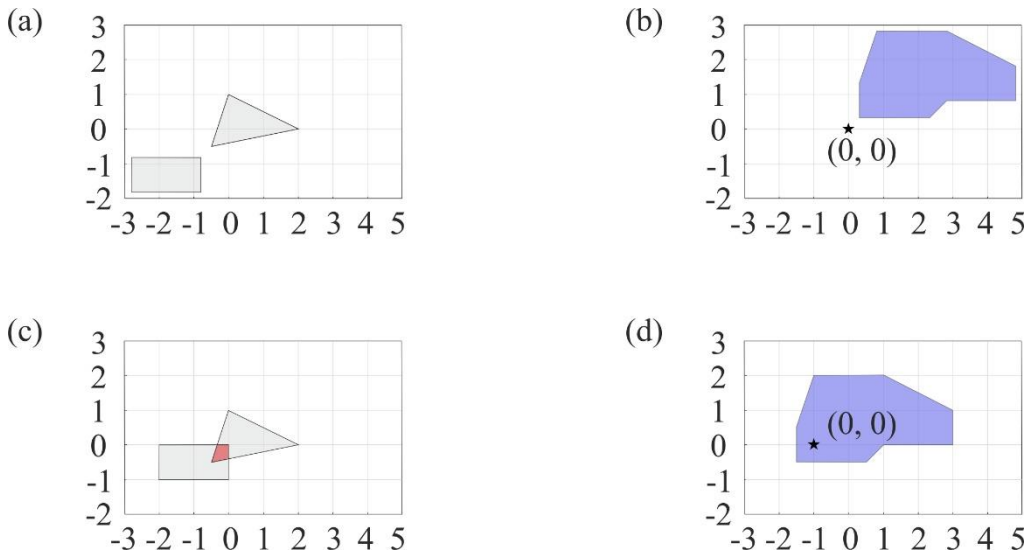

Figure 4.7 (a) Two polygons in Euclidean space when they are not overlapping, and (b) their corresponding MD. (c) Two overlapping polygons in Euclidean space, and (d) their MD.

Figure 4.7(c) shows the same rectangle and the triangle but they intersect one another in Euclidean space. Their corresponding MD has the same geometry but contains the origin as shown in Figure 4.7(d). This is because the overlapping region in Euclidean space indicates that some points in the triangle share the same coordinates as the points in the rectangle. When all the points in the triangle are subtracted from all the points in the rectangle, one of the differences must be a zero vector. The same principle can be applied to convex polytopes in 3D or even higher dimensions.

MD transforms the problem of intersection detection between two polytopes into determining if a point is within a new polytope or not. The geometrical collision detection can be conducted through the GJK algorithm (Gilbert et al., 1988), which calculates the MD of any given convex polytopes. It outputs the proximal distance between the two panels, i.e. the minimal distance between them if they do not interfere with each other. Otherwise, the proximal distance is set to zero.

The dynamic simulation contains a total of S time steps with the corresponding time instances being t_j (j = 1, 2, … S) evenly distributed from the start to the end of the deployment. By post-

processing the dynamic simulation results, the positions of all the panels can be acquired. Applying the algorism outlined above, a dataset **D** of S columns can be obtained, with each column denoted as $\mathbf{D}_j$, containing the proximal distances between every pair of panels except the connected ones at time instance t_j.

4.4 Collision avoidance via optimisation

In this multi-body system, the properties of the panels and their connectivity are pre-determined based on the applications. To avoid collisions in the deployment process, the trajectory of panels needs to be sequenced by carefully designing the properties at various hinge locations, including the stiffness and damping coefficient (Yang et al., 2022b). Nevertheless, the stiffness and damping coefficient to reflect the actual situation upon physical contact, k_s and c_s are pre-determined and hence, not to be optimised. Besides, the hinge properties at the cut joint are pre-set, including the virtual spring stiffness k_{ch} and the damping coefficients c_{ch} so that the separations between M and M′, N and N′ are negligible in comparison to the motion-of-interest during the deployment process, meanwhile ensuring the system not being too stiff to cause integration errors.

Therefore, the deciding parameters at a hinge that affect the trajectories of panels are the torsional spring stiffness k_i and the damping coefficient c_i. The stiffness of a spring can be tuned, but the damping of the elastic hinge is not easily tuned unless packing lubricants with different viscosities are applied within the hinge. When precise damping control is absent, we assume that the energy loss is through Rayleigh damping, i.e., the damping changes in proportion to the change of spring stiffness (Adhikari & Phani, 2007; Gartung, 2018). This is reasonable because if we put two identical torsional springs in parallel to double spring stiffness at one hinge, the damping coefficient of this hinge doubles as a result. Based on this assumption,

the only independent variables are now the spring stiffness at various hinge locations $K = \{k_0, k_1, \ldots, k_{n-1}\}$. The aim is to acquire appropriate spring stiffnesses so that no collision amongst panels occurs during deployment. Once a suitable set of stiffnesses is obtained, corresponding springs can be produced by changing their windings during manufacturing. This leads to an optimisation process.

A few parameters need to be introduced following the collision detection method outlined previously. In ascending order of time instances, every element in $\mathbf{D}_j$ is examined after each simulation. If one or more elements are identified to have zero value, the first collision takes place. The time instance is denoted as t_J and its corresponding column of proximal distances that contain zero elements is denoted as $\mathbf{D}_J$. A dataset $\mathbf{V}_J$ will be calculated, containing the approaching speed of every pair of panels at t_J, using

$$\mathbf{V}_J = \frac{\mathbf{D}_{J-2} - \mathbf{D}_{J-1}}{t_{J-1} - t_{J-2}} \tag{4.25}$$

and then set the elements in $\mathbf{V}_J$ to zero if the corresponding elements in $\mathbf{D}_J$ have non-zero values. It is reasonable to assume that $J \geq 3$ since it is unlikely in practice that the panels collide right after being released from stacks. Once a collision is detected at t_J, the subsequent deployment becomes invalid and therefore the dynamic simulation results are voided.

Let d_p be the value of the smallest element in $\mathbf{D}$ and v_a be the value of the largest element in $\mathbf{V}_J$. When no collision is detected, $\mathbf{V}_J$ is not defined and v_a is set to zero. The optimisation process minimises v_a, the approaching speed if panels collide during the simulation; and maximises d_p, the minimum proximal distance between any pair of panels if the panels are not in collision. A single-objective function can be formulated as

$$\min f(K) = pv_a - qd_p \tag{4.26}$$

where p and q are pre-set coefficients to make pv_a and qd_p unitless. The set of variables to be optimised is $K = \{k_0, k_1, \ldots, k_{n-1}\}$, the stiffnesses of torsional springs at all hinges. They are allowed to vary within the upper and lower bounds specified by the user.

Figure 4.8 shows a flow chart of the optimisation process. It starts with an initial set of spring stiffnesses K_0 as input, which is advanced through dynamic simulation and collision detection. If collisions occur, MATLAB function *fmincon* (MathWorks, R2019b) is used to minimise $f(K)$ via an interior-reflective Newton approach (Coleman & Li, 1994) aimed to minimise v_a, the approaching speed between two panels. This leads to a set of updated K. The process is repeated until no collision is detected, indicating that the acquired K is a feasible solution.

Among many feasible solutions, it is preferable to have panels as far apart as possible throughout the deployment process. Hence, even after a set of K is obtained with no collisions, the objective function $f(K)$ can be continuously optimised via running MATLAB function *fmincon* until a local optimum is found. If on the other hand, collisions remain to be unavoidable at the end of the iterations, where the objective function is positive, a new set of initial spring stiffnesses is used to re-run the optimisation process.

Besides, the program checks if the panels have been deployed to a flat surface at the end of each iteration. If not, the simulation results are also rejected and another iteration starts.

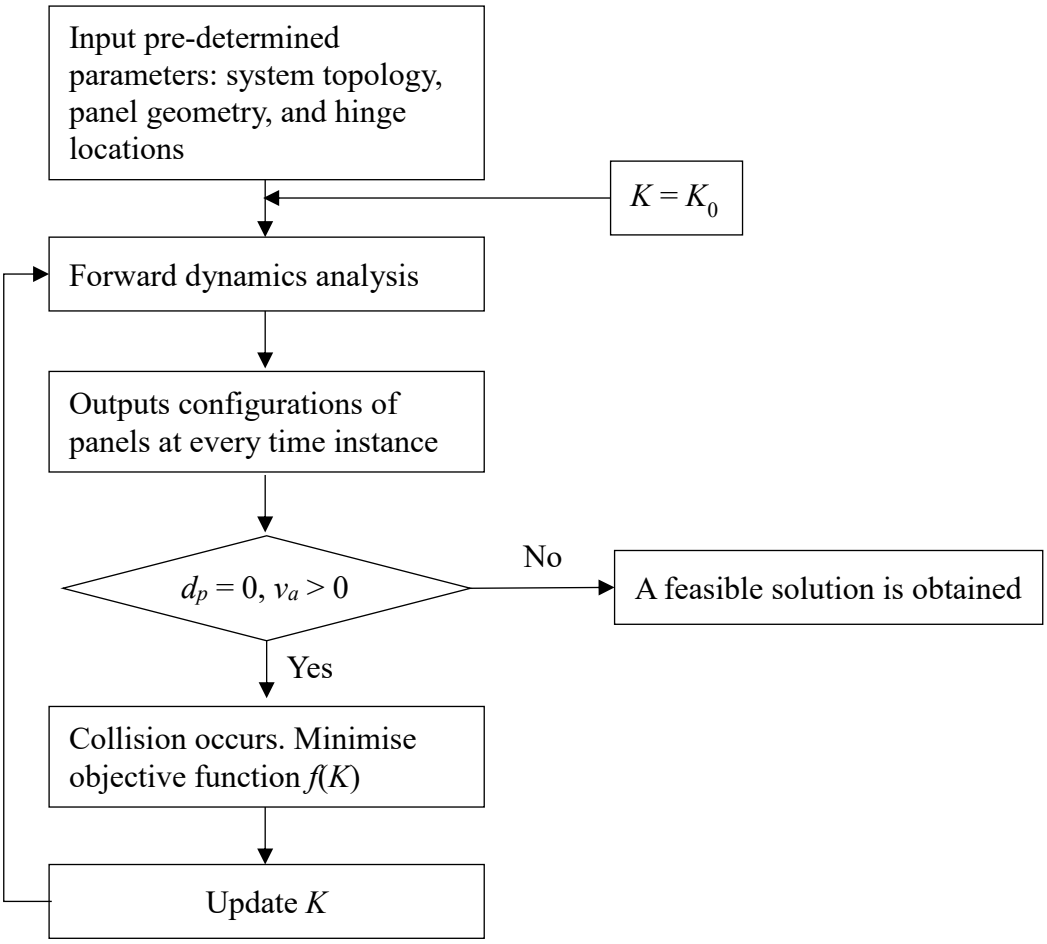

Figure 4.8 Flow chart of the optimisation process for the spring parameters.

4.5 Physical models and experiments

4.5.1 Folding and deploying a rectangular array with the same spring stiffness

An array was constructed to demonstrate the effectiveness of the compact packaging scheme and the subsequent deployment process without collision. Its topology and geometry follow the design in Figure 4.1, and thus, it contains eight identical smaller panels and four larger panels that are twice the size of the smaller ones, as shown in Figure 4.9(a).

(a) (b)

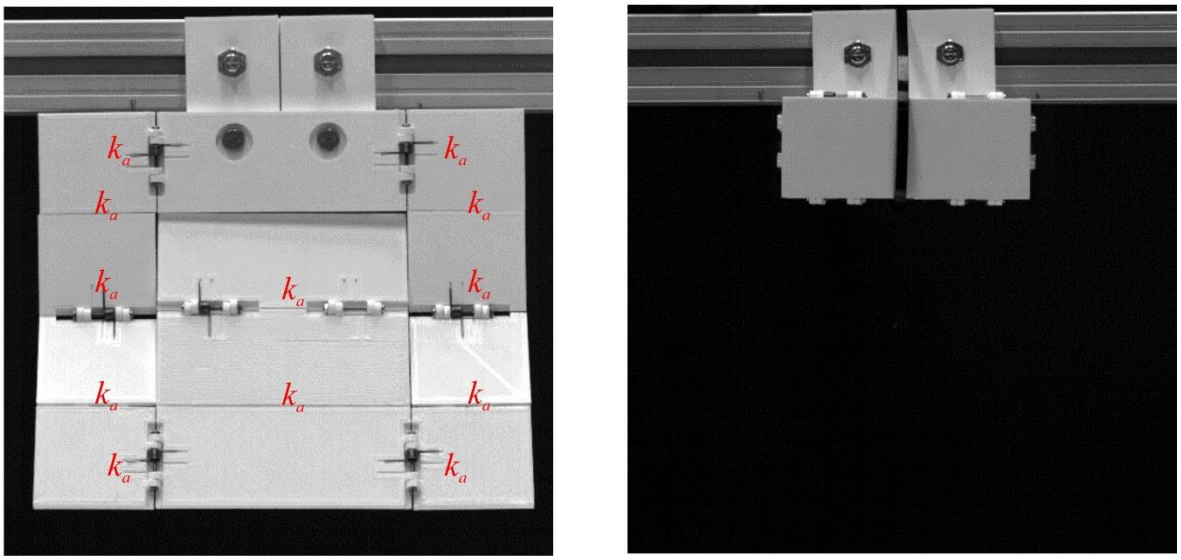

Figure 4.9 (a) Torsional springs with the same stiffness k_a were connecting the panels in an array. (b) The array was folded into two stacks and confined by a cable tie.

The geometry of a smaller panel is detailed in Table 4.1. All panels were 3D printed by Raise3D N2 using Polylactic acid (PLA) material with 0.15 mm layer resolution and 5% honeycomb infill to obtain reasonable precision while minimising the mass. The panel was then weighed on a scale and density was calculated from the ratio of the mass and volume of the panel.

Table 4.1 Dimensions and physical properties of a small rigid panel

Panel length (mm)	50
Panel width (mm)	40
Panel thickness (mm)	6
Panel density (kg/m^3)	547

The linear torsional springs with the same stiffness k_a were commercially available from McMaster-Carr®. They were designed to have 180° deflection angles and manufactured by music-wire steel, whose Young's modulus is 207 GPa (McMaster-Carr, 1994). The torsional springs are placed along all the hinges such that the resting position of the springs coincided with the deployed configuration of the rectangular array. The optimisation process outlined in Section 4.4 was not yet implemented at this stage. After that, the array was folded into two stacks, which were confined by a plastic cable tie and fixed onto an aluminium frame that was mounted on the floor, as shown in Figure 4.9(b).

The deployment process was initiated by cutting the cable tie. A PHOTRON FASTCAM SA-X2 camera recorded the deployment process with a motion capture rate of 1000 fps. The video is included in the *supplementary materials*. Besides, some characteristic snapshots of the deployment process are presented in Figure 4.10. The large panel in the middle of the array swung back and collided with the back of the top panel when t = 0.30s in Figure 4.10(e).

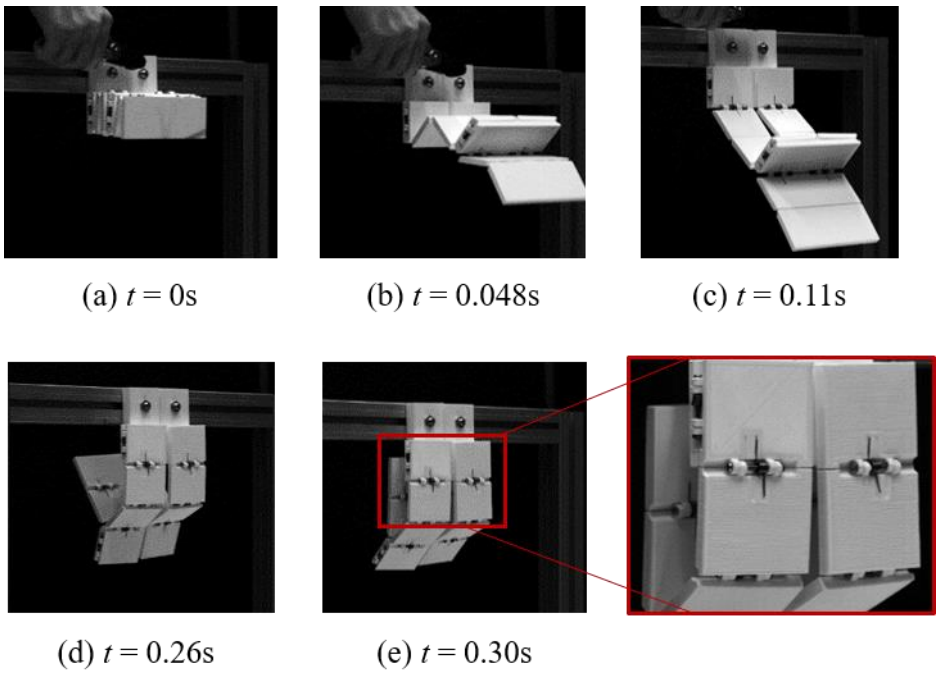

Figure 4.10 Deployment exhibited collision when the same stiffness was applied at every hinge.

The deployment after the first occurrence of collision is not in the interest of this work as any collision is to be avoided by adjusting the stiffness of torsional springs through the optimisation package. Before that, the spring stiffness k_a and the damping of the hinge were measured experimentally.

4.5.2 Measuring the spring stiffness (Yang et al., 2022c)

Figure 4.11 shows the apparatus to test the stiffness of the torsional spring, which is a similar setup as described in (Seffen & Pellegrino, 1999). Four threaded holes were drilled on the platform at an equal distance away from the centre. To measure the angle of rotation of the torsional spring, a testing specimen was set up consisting of two rigid blocks connected by a rotational hinge that housed the spring. The rigid blocks were 3D printed using the same PLA material and the same printing settings as the panels that were constructed in the experiments. The two rigid blocks were mounted onto the platforms such that their mid-plane was passing through the geometric centre of each platform. The platforms were then connected to the shaft of a torsion gauge (Omega TQ202 Series Reaction Torque Sensor). The lower end of the platform fitted over the torsion gauge shaft and three grub screws were against three flat surfaces of the shaft of the torsion gauge to ensure that there were no relative rotational motions between the platform and the shaft. Each gauge was wired to a 10V DC source and a voltmeter. When a torque was applied to its shaft, where a sensor plate was attached, an output voltage could be read from the voltmeter, indicating the magnitude of the applied torque. The torsion gauge on each side was then placed on a 60 mm × 60 mm Standa Rotary Table, respectively. The rotary table on the left-hand side was fixed to the ground through an aluminium block. The one on the right-hand side was mounted onto a carriage of the same height as the aluminium block that was moving linearly on two parallel rails. Therefore, the rigid block on the left-hand

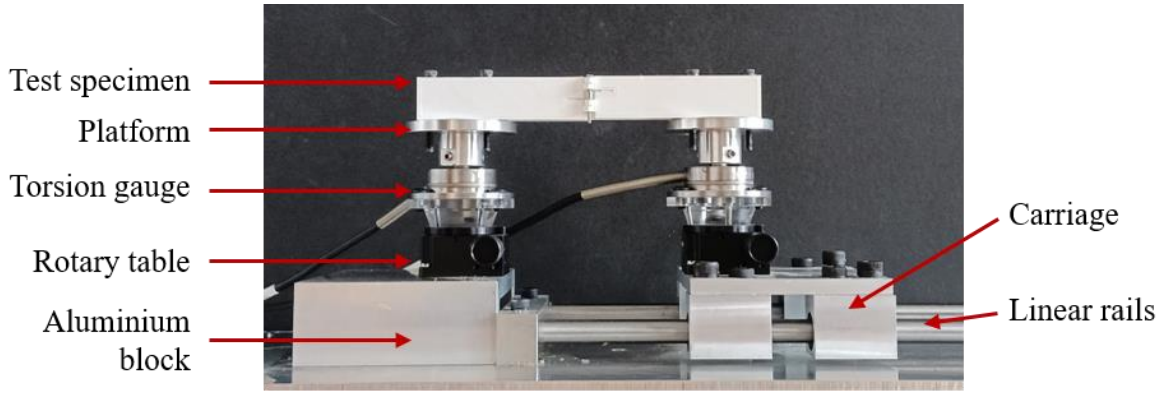

Figure 4.11 The setup to test the stiffness of torsional springs quasi-statically.

side could only rotate about the centre of its corresponding rotary table; whereas the one on the right-hand side had both rotating motion about the centre of its corresponding rotary table and free linear motion along the rails. Between the rails and the carriage, bearings were installed to minimise friction when the carriage was travelling along the rails.

The measurement started when there was no strain in the torsional spring, where the angle of rotation of the spring is 0 rad. The rotary tables were aligned at the best possible angle so the moment applied on the testing sample was negligible. The rotation angles of the rotary tables were marked as 0 rad at both ends. After that, a rotation was applied to the testing specimen by turning the knobs of the rotary tables at each end simultaneously in increments of 1 arcminute, which is 1/60 of a degree or $\pi/10800$ radian. Driven by the rotary tables, the carriage moved closer to the aluminium block along the parallel rails. The torque incurred by the torsional spring was transferred to the strain gauges and indicated by the output voltages on the voltmeters. The output voltages of the two gauges were then recorded in an Excel spreadsheet after every increment. Then, another rotation was applied and the previous steps were repeated multiple times. An example of the testing specimen is demonstrated in Figure 4.12 when it was in the process of measurement.

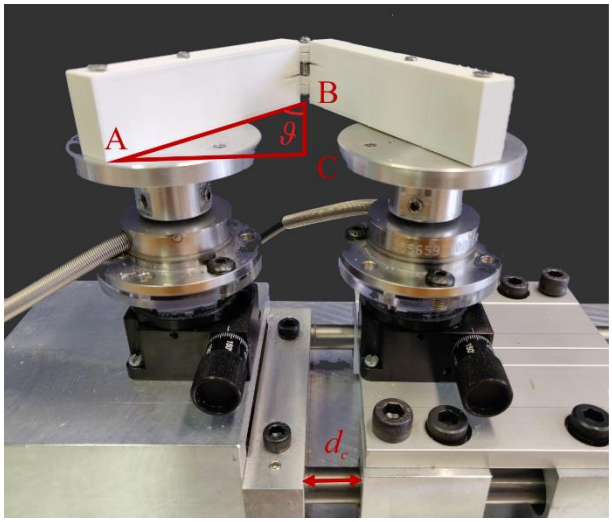

Figure 4.12 A configuration of the test specimen when the spring was deformed.

The measurements continued until the distance between the aluminium block and the carriage d_c became zero. Besides, the output voltage on either voltmeter was ensured not to exceed 20 millivolts, which was 95% of the capacity of the torsion gauge. Finally, the voltage outputs were converted to bending moments according to calibration equations provided by the manufacturer's datasheet. In each increment, an average value of the bending moments at both ends was taken.

The required torque to generate the corresponding angles of rotation of the spring was plotted in Figure 4.13. The data points were then linearly fitted with a gradient of 0.10 Nm/rad, which was regarded as the spring stiffness. The raw data of the torque versus the angle of rotation can be found in an open-access data repository https://data.mendeley.com/datasets/fnw2jrwwhx/1 (Yang, 2022).

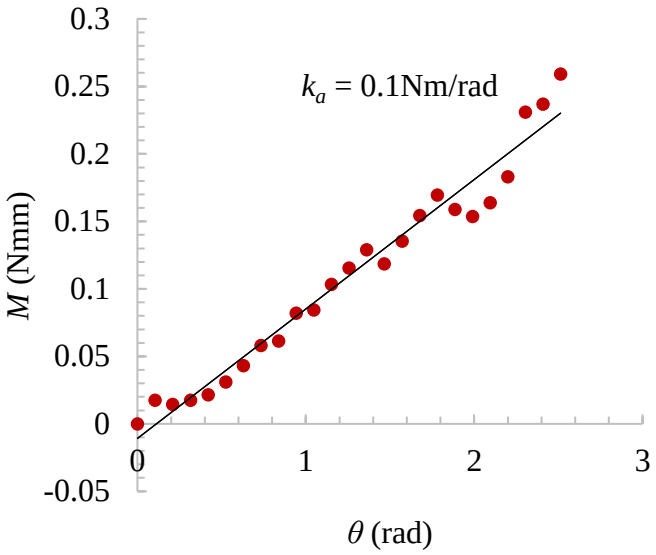

Figure 4.13 Moment and rotational angle relationship of a torsional spring with stiffness k_a.

It can be noted from Figure 4.13 that the angle of rotation of the spring is not reaching its expected range of motion, π. This is because the maximum angle of rotation of the spring can only reach $13\pi/15$ before d_c reduces to zero. The stiffness of the spring when the angle of rotation beyond $13\pi/15$ was not measured. However, according to the trend of the curves in Figure 4.13, the stiffening effects of the springs were observed at large angles. The actual overall stiffness of the torsional springs was therefore expected to be slightly higher than the current linearly fitted gradient. This source of error can be reduced by increasing the length of the rigid blocks AB as shown in Figure 4.12. When d_c reached zero, the length AC was a fixed value based on the dimension of the apparatus. A longer AB would result in a smaller ϑ, which is half of the dihedral angle between the two blocks, and hence the larger angle of rotation. However, as the length increases, the blocks could become more flexible, resulting in a non-negligible bending of the blocks as compared to the deformation of the spring. Therefore, both the range of rotational angles and the flexibility of the material were considered when designing the specimen.

4.5.3 Measuring the damping

Five free-vibration tests were conducted on a single Degree-of-Freedom (DoF) rotational system to measure the damping ratio of the elastic hinge as demonstrated in Figure 4.14.

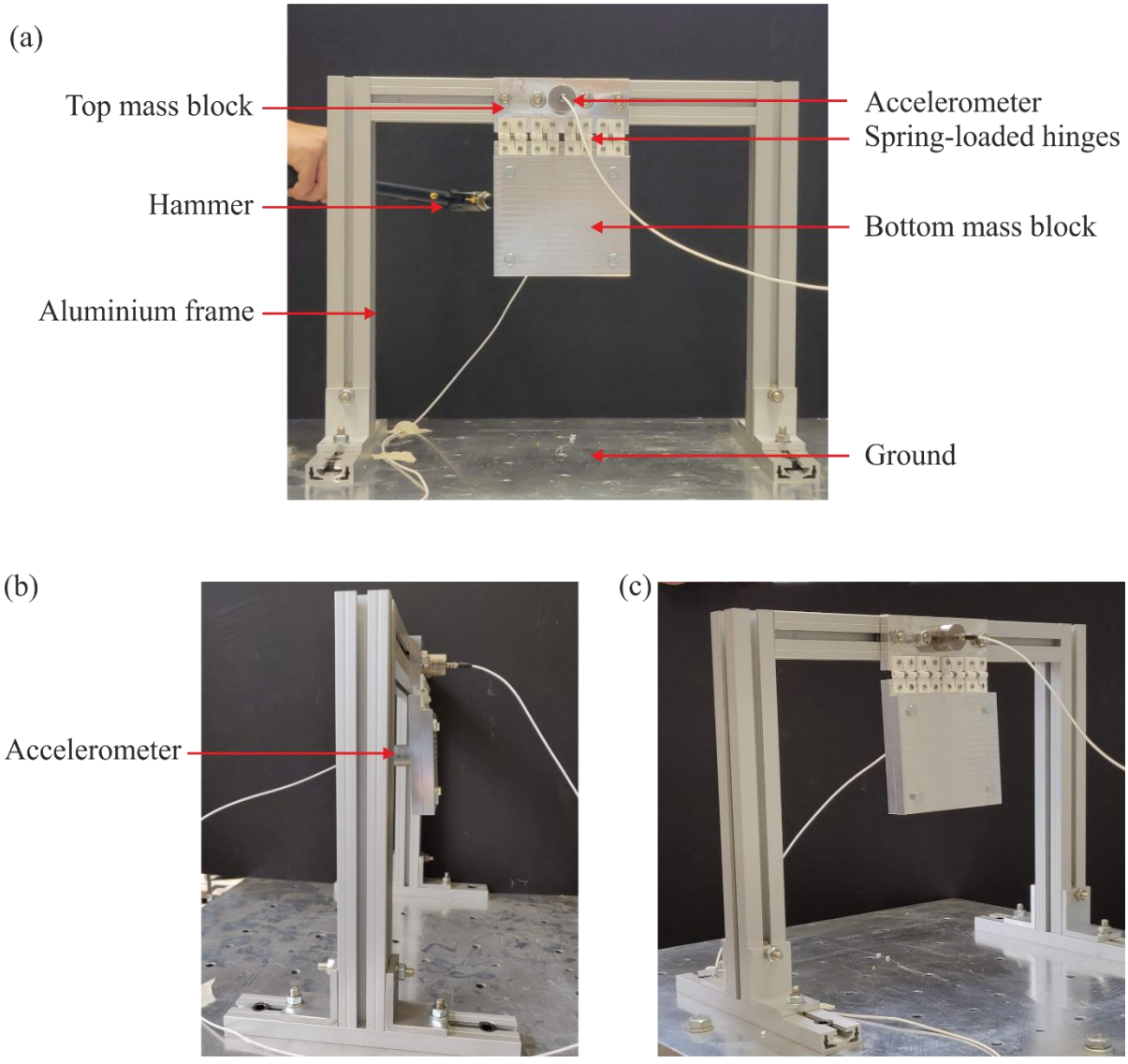

Figure 4.14 Free vibration tests were conducted on a single-DoF rotational system. (a) Front view, (b) side view, and (c) isometric view.

The mass blocks were machined from 6061 aluminium alloy, whose density is 2700 kg/m^3 and Young's modulus is 69 GPa. The top block was fixed to an aluminium frame that was grounded.

The bottom aluminium block, which weighed 0.98 kg, was allowed to rotate with respect to the top one resisting four elastic hinges with a measured spring stiffness of 0.10 Nm/rad each. To acquire the free-vibration response of the system, two accelerometers (PCB Piezotronics with model number 393B04) with sensitivities of 1005 and 998 mV/g were mounted onto the centres of the surfaces of the top and bottom mass blocks, respectively. The time histories of acceleration were sent to a PXI system (National Instruments PXIe-1082) with a sampling rate of 200 Hz, which then could be visualised through LabVIEW.

In each test, the bottom mass block was excited by an Impact Hammer (Impulshammer inkl. Kraftaufenhmer 8200) which resulted in an initial velocity of the block. After each hammer strike, the responses of the frame and the mass block were recorded in the magnitude of gravitational acceleration g until the mass block came to a rest. An example in Figure 4.15 shows a decaying motion of the mass block and a constant vibration of the frame. After processing the data through a highpass Butterworth filter (Greene, 2021), which eliminated low-frequency noise that was below 0.5 Hz, the system identification was carried out by estimating a state-space model of the system using the N4SID algorithm (Ljung, 1988; Overschee & Moor, 1994). The frequencies and damping ratios corresponding to the identified state-space matrices were then calculated (Reynders, 2012).

After dropping the first several data points for which the hammer was still in contact with the mass block, the acceleration of the frame was used as an input signal and the acceleration of the mass block was used as an output signal. N4SID resulted in models of different state sizes, from which the frequencies f and the damping ratios ζ of the system were retrieved from the eigenvalues of the state matrix of the state-space model (Cara et al., 2013). Typically, successful model orders were in the size of four or six, resulting in two to three modes. For instance, the structural vibration frequencies of the structure were calculated to be 2.53 Hz, 33.72 Hz, and 89.64 Hz in one test.

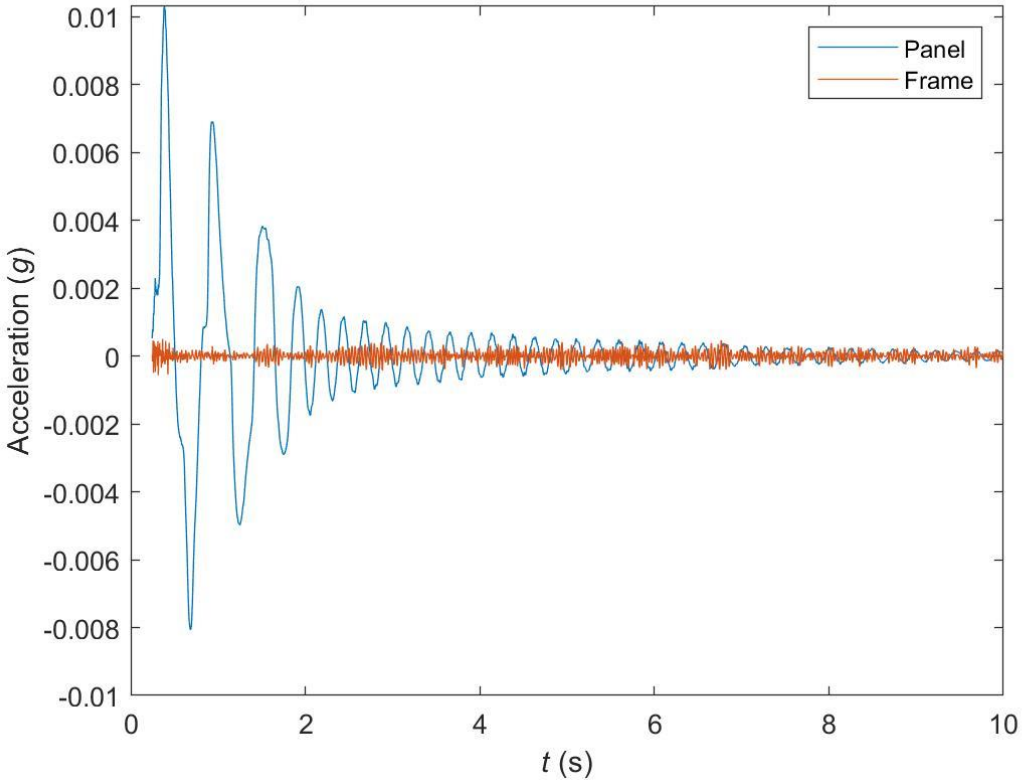

Figure 4.15 Free-vibration response of the spring-mass system after a hammer strike.

The raw data recorded by accelerometers in this test can be found in a Mendeley data repository https://data.mendeley.com/datasets/fnw2jrwwhx/1.

Only the smallest natural frequency and its corresponding damping ratio were recorded in each test as they described the vibration mode due to the rotation of the panel about the hinges. The larger natural frequencies and their corresponding damping ratios appeared to be associated with additional vibrational modes of the aluminium frame. The large separations between the identified modes also allowed us to truncate to the first mode, which appeared to describe the rotation of the mass block about the elastic hinges.

Five free-vibration tests had been conducted and the frequency of vibration f and its corresponding damping ratio ζ were recorded in each test. After that, the damping coefficient c_a of each elastic hinge was obtained by

$$c_a = \zeta c_c / 4, \tag{4.27a}$$

$$c_c = 2 I_m \omega_n \tag{4.27b}$$

$$\text{and } \omega_n = 2\pi f \tag{4.27c}$$

where c_c and ω_n are the critical damping coefficient, and the natural frequency of the system, respectively. I_m = 0.0051 kg·m^2 is the moment of inertia of the aluminium block rotating about the hinges. The damping coefficient was divided by four because four elastic hinges with the same stiffness k_a were connecting the mass block to the frame.

Table 4.2 summarises the damping properties obtained from five tests, whose first two columns are data for four hinges in parallel, and the last column lists the calculated damping coefficient for one hinge with a spring stiffness of 0.10 Nm/rad. The average damping coefficient is calculated to be 0.0043 Nm·s/rad with a small standard deviation of 0.0002 Nm·s/rad.

Table 4.2 Summary of damping properties of the elastic hinges with stiffness 0.10Nm/rad.

Test	Frequency f (Hz)	Natural frequency ω_n (rad/s)	Damping ratio ζ	Damping Coefficient c (Nm·s/rad)
1	2.530	15.896	0.110	0.0045
2	2.425	15.237	0.111	0.0043
3	2.462	15.467	0.115	0.0045
4	2.642	16.598	0.100	0.0042
5	2.440	15.332	0.101	0.0039
AVG	2.497	15.689	0.107	0.0043
SD	0.088	0.553	0.007	0.0002

4.5.4 Optimisation for a collision-free deployment

An optimisation process was conducted to search for a set of suitable spring stiffness to avoid any collision occurring during deployment.

First, the assembly was modelled in MATLAB Simscape according to its topology and the physical properties of the rigid panels as listed in Table 4.1. The same spring stiffness was adopted for springs at symmetrical hinge locations to obtain a symmetrical deployment, with the lower and upper bounds of the stiffness along all hinges set to be 0.001 and 0.2 Nm/rad, respectively. After that, the optimisation process started with an initial rotational spring stiffness of k_a = 0.1 Nm/rad and a damping coefficient of c_a = 0.0043 Nm/(rad/s) at all hinges, which were the test results from Sections 4.5.2 and 4.5.3. During the optimisation process, the damping coefficient of the spring changed with spring stiffness but remained proportional to it, according to the previous assumptions. The gravitational acceleration g was set to 9.81 m/s^2 in all simulations to resemble the Earth-based deployments. Other properties of the hinges that were input to initiate the dynamic simulations were enumerated in Table 4.3.

Table 4.3 Hinge parameters that are not to be optimised

Initial hinge angle (rad)	0.999π
Final hinge angle (rad)	0
Contact stiffness k_s (Nm/rad)	10^6
Contact damping c_s (Nm·s/rad)	1
Cut hinge stiffness k_{ch} (N/m)	10^8
Cut hinge damping c_{ch} (Ns/m)	10

Before each simulation, the torsional hinges were rotated 0.999π, which was 99.9% of its total range of motion. The deformed springs had tendencies to return to their natural length, which drove the deployment of the array. Contacts occurred when any torsional hinges tended to cross their permissible range of motion, 0 or π rad. Torsional springs and dampers with high stiffness k_s and high damping c_s were implemented at all hinges to model the contacts. Besides, translational springs and dampers were enforced at the cut hinge with high stiffness k_{ch} and high damping c_{ch} to resemble the assembly before the cut was made. All the hinge parameters listed in Table 4.3 were not to be optimised.

A set of optimised spring stiffnesses was obtained after the optimisation process, and the values at all hinges were marked in Figure 4.16(a). The optimised stiffnesses ensured a collision-free deployment in the simulation.

To check the effectiveness of the optimisation package, a physical prototype was built afterwards, in which the optimised values were conveniently rounded and indicated along the hinges as shown in Figure 4.16(b). Since the top two horizontal hinges have rather negligible stiffness, more than ten times smaller than that of the other springs, hinges of zero stiffness were used for them. Besides, some rotational hinges employed two springs that were placed in parallel to obtain the required stiffness. For instance, the 0.20 Nm/rad was achieved by placing two springs with stiffness k_a.

(a) (b)

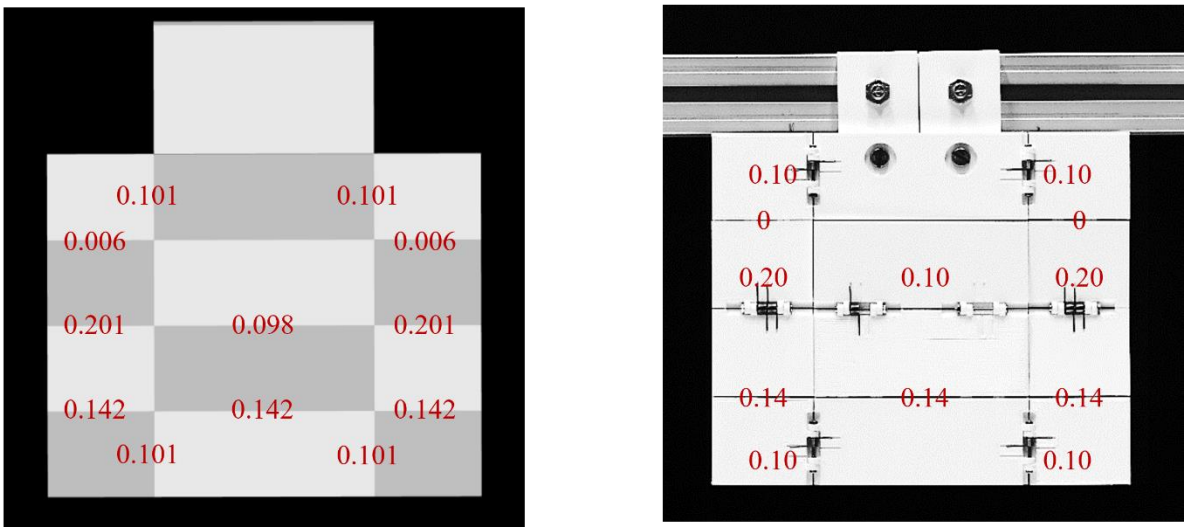

Figure 4.16 Assignments of spring stiffnesses at various hinges (in Nm/rad). (a) The optimised values and (b) the values used to construct the physical prototype.

4.5.5 Collision-free deployments with a physical prototype

Apart from the spring with a stiffness of 0.10 Nm/rad, the second type of spring with a stiffness of 0.07 Nm/rad can be manufactured with fewer music-wire steel coils. The springs were commercially available from the same manufacturer, McMaster-Carr®. It was also measured quasi-statically using the same testing method detailed in Section 4.5.2, and the test results were plotted in Figure 4.17. The data between the required torque and rotational angles were linearly fitted to a line of gradient 0.07 Nm/rad, which was regarded as the stiffness of the spring, k_b.

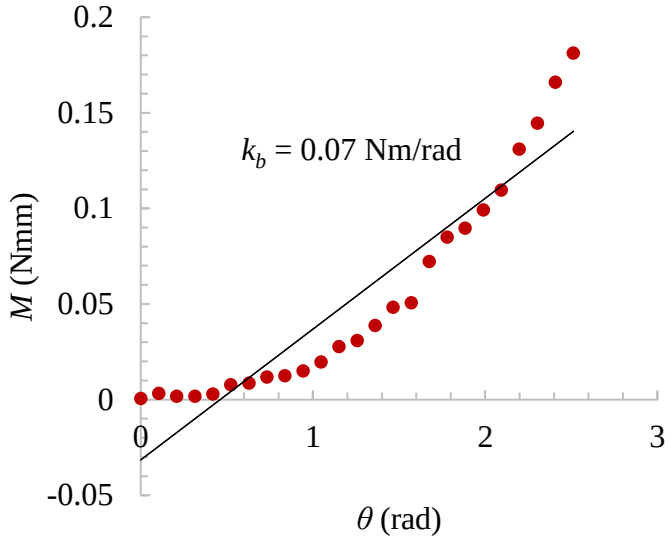

Figure 4.17 Moment and rotational angle relationship of a torsional spring with stiffness k_b.

Five tests were conducted to test the collision-free deployment of the prototype. The outcomes were rather consistent, and no collision was observed throughout the deployment processes. Some snapshots are shown in Figure 4.18 to benchmark the simulated and actual deployment of one of the tests at some characteristic time instances. Overall, the simulated and experimental deployments matched well except at t = 0.11s. The discrepancies might come from many aspects. For instance, the aerodynamic drag was not considered in the simulation but was inevitable during the deployment of the physical prototype. Besides, there might be inaccuracies when measuring the spring stiffness and damping coefficients of a hinge.

The videos of the simulation and the deployment of the physical prototype are included in the *Supplementary Materials*. The deployment was considered to be completed once a flat surface was first reached. However, the panels tended to oscillate around their corresponding equilibrium positions before settling down since there was no locking mechanism installed at any of the hinges. This was observed in both the experiments and the simulation in the videos despite not being shown in Figure 4.18.

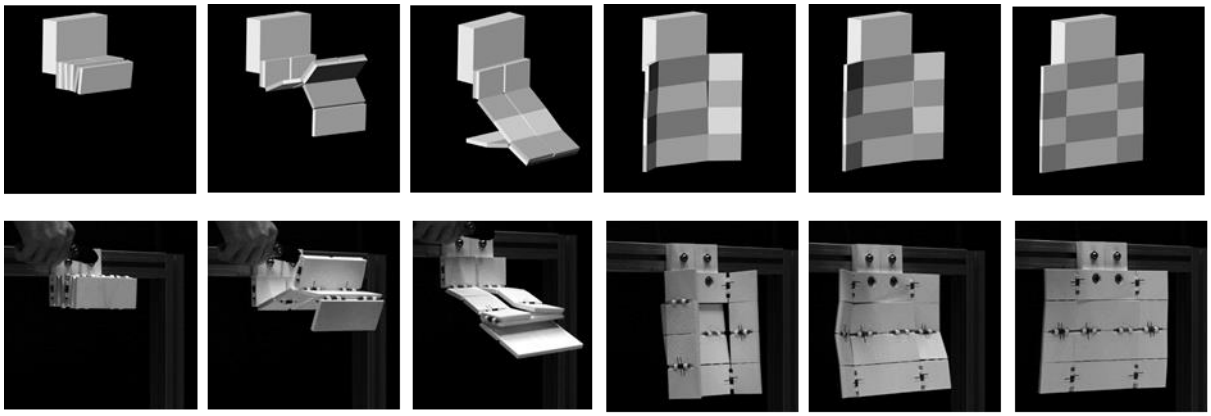

(a) $t = 0$s (b) $t = 0.048$s (c) $t = 0.11$s (d) $t = 0.26$s (e) $t = 0.30$s (f) $t = 0.36$s

Figure 4.18 The simulated (first row) and actual (second row) deployments at representative moments.

4.6 Conclusion

This chapter deals with the deployment of compactly folded chessboard-like flat arrays. The assembly processes multiple DoFs, which are inevitable when the number of panels is large. Spring-loaded joints are therefore employed to synchronise the deployment process. An optimisation method was proposed to select the stiffnesses of joints to ensure a collision-free deployment. Dynamic simulation of deployment and a collision detection method were incorporated into the optimisation process. The sequenced deployment trajectories of the panels ensured that no collisions occurred in the simulation, and the array was always deployed to a flat surface from the packaged stacks. Although a continuous optimisation process was carried out, the stiffnesses of the torsional springs are discrete. A prototype was constructed based on the closest number of the optimised spring parameters obtained in the simulation and the collision-free deployments were successfully validated by experiments. Apart from deploying solar panels driven by linear rotational springs, this research demonstrates a potential to deploy panels that are connected by compliant hinges (Howell, 2001) with the energy-restoring property.

The discrepancies between the results of the simulation and experiments may come from many aspects. First, the elasticity of the panels was not considered in the multibody dynamics simulation, in which all panels were assumed to be rigid bodies for a faster simulation result. Secondly, it was noticed that the damping coefficient at each hinge is an important parameter that could affect the deployment process. It is, however, rather complex to measure in the actual prototype. This problem can be overcome either by more precise measurement in future work or by incorporating suitable damping control within spring-loaded joints, for instance, by applying packing lubricants of different viscosities within the rotational hinges. Thirdly, the stiffness of the torsional springs might be quadratic instead of linear by nature, with a higher stiffness when the angle of rotation is larger and a lower stiffness when it is smaller. Therefore, the panels were expected to deploy faster than the simulation at the beginning of the deployment process and slowed down later on. The simulation model can be refined by using the exact moment-angle relations in future work.

Besides, the torsional springs can be designed to have non-zero torque at the fully deployed configuration to resist any unexpected disturbance that may act on the flat array after being deployed.

CHAPTER 5

SINGLE-DOF KIRIGAMI WITH UNIFORM THICKNESS

The approach presented in the previous chapters enables flat arrays consisting of regular polygons to be packaged into compact stacks by arranging revolute joints according to the HC of the panels. The resultant assemblies usually have multiple DoFs. In this chapter, we first use the HC approach to construct a foldable element and then combine four such elements to form a unit that can be packaged into compact stacks without any voids with a single DoF. Flat arrays consisting of many such units can be created where the kinematic properties associated with their constitutive units are retained.

5.1 Compact folding triangular prisms

5.1.1 Folding a loop of triangles into two compact stacks

Consider an origami pattern consisting of ten identical isosceles triangles, P_1, P_2,…, P_{10} as shown in Figure 5.1(a). An HC can be found for it, which is plotted in blue dotted dash lines (Yang et al., 2022a). Placing the mountain and valley creases accordingly, the assembly can fold into two compact stacks. It is a closed kinematic chain of ten rigid bodies, and in general, the number of DoF is four, calculated using the Kutzbach criterion in Eqn (2.4).

In the folded configuration, facets P_4, P_5 and P_9, P_{10} appear to be the top and bottom layers of the stacks, respectively. Since there is no relative motion between these two-facet pairs, the crease between P_4 and P_5 need not be activated. Neither does the one between P_9 and P_{10}. It is possible to rigidise the two creases without changing their stackability.

As the result, two pairs of triangular facets are merged into two parallelograms, as illustrated in Figure 5.1(b). Connected by eight creases, the facets are re-numbered from P_1 to P_8, where P_1 – P_3 and P_5 – P_7 are six isosceles triangles, and P_4 and P_8 are two parallelograms. It is a kirigami pattern due to the slit between facets P_3 and P_7.

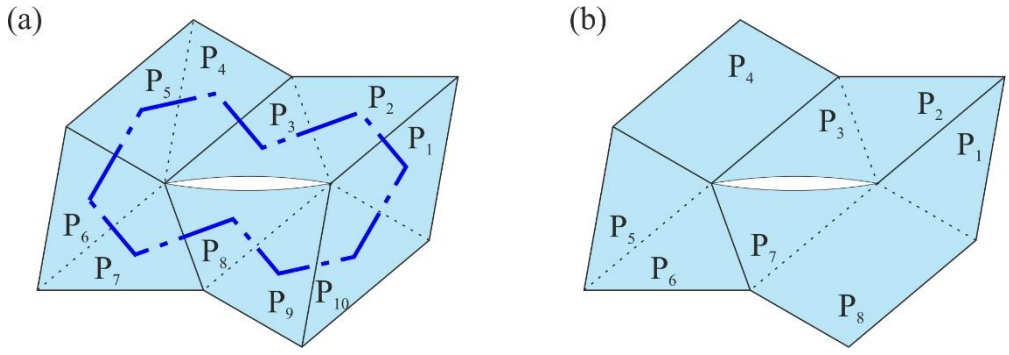

Figure 5.1 Forming a kirigami pattern from isosceles triangles. (a) A slit is made if an edge is not crossed by the HC plotted in the array. (b) A kirigami pattern of six isosceles triangles and two parallelograms.

Converting the facets to panels of uniform thickness yields an assembly shown in Figure 5.2(a). Consecutive panels are connected by a rotational joint (also known as a revolute joint) whose axis is along the bottom or top edges of the panels subject to mountain or valley creases, respectively. It is better visualised in a partially folded view as shown in Figure 5.2(b), in which the slit between P_3 and P_7 remains.

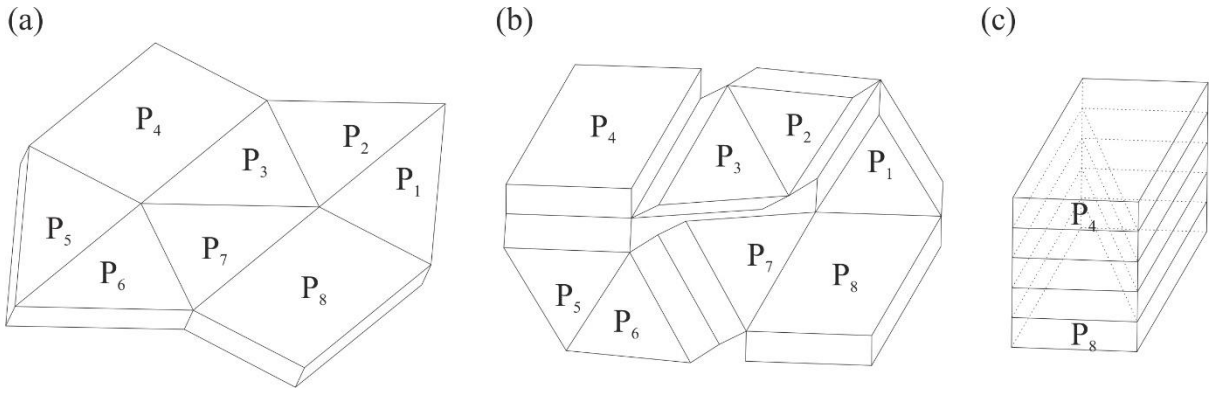

Figure 5.2 A thick-panel version of the 8R assembly. (a) Converting the kirigami pattern to thick panels with uniform thickness. (b) A partially folded and (c) fully folded 8R assembly.

Since there are a total of eight revolute joints, kinematically this assembly is an 8R closed chain, with the remaining DoF being

$$\text{DoF} = 6(n-1) - 5j = 6\times(8-1) - 5\times 8 = 2 \tag{5.1}$$

where the number of panels $n = 8$ and the number of revolute joints $j = 8$.

The fully folded configuration of this 8R assembly is illustrated in Figure 5.2(c). As expected, the parallelogram panels P_4 and P_8 appear at the top and bottom layers of the stack, respectively, whereas all of the triangular panels are sandwiched between panels P_4 and P_8. This 8R closed chain is the element that is used to construct foldable units.

5.1.2 Kinematics of the 8R element

Since the 8R element can be modelled by a spatial linkage (Chen et al., 2015), it can be analysed through the matrix method based on the D-H notation (Denavit & Hartenberg, 1955). A partially folded 8R element is shown in Figure 5.3(a), in which eight Cartesian coordinate systems are set up with the axis z_i along the axis of joint i (i = 1, 2, …, 8) and x_i along the thickness direction of panel P_{i-1}. Axis y_i is not shown in the figure but it can be easily obtained by the right-hand rule.

Based on the coordinate systems in Figure 5.3(a), an equivalent linkage of the 8R element can be obtained as shown by the red lines in Figure 5.3(b). The geometric parameters and kinematic variables are defined as follows. Link length $a_{(i-1)i}$ measures the normal distance between axes z_{i-1} and z_i, positively along x_i. $\alpha_{(i-1)i}$ is the twist angle from axes z_{i-1} to z_i positively about x_i. The offset d_i is the distance between x_i to x_{i+1}, positively along z_i, and the kinematic variable θ_i is the angle of rotation from x_i to x_{i+1} positively about z_i.

A set of dihedral angles are then introduced along the revolute joints for they are more intuitive to describe the folding process in origami structures. Let φ_i be the dihedral angle between adjacent panels with a common axis z_i. There are

$$\begin{aligned} &\theta_1 = \pi - \varphi_1,\ \theta_2 = \varphi_2,\ \theta_3 = -\varphi_3,\ \theta_4 = \varphi_4, \\ &\theta_5 = \varphi_5 - \pi,\ \theta_6 = -\varphi_6,\ \theta_7 = \varphi_7,\ \theta_8 = -\varphi_8. \end{aligned} \tag{5.2}$$

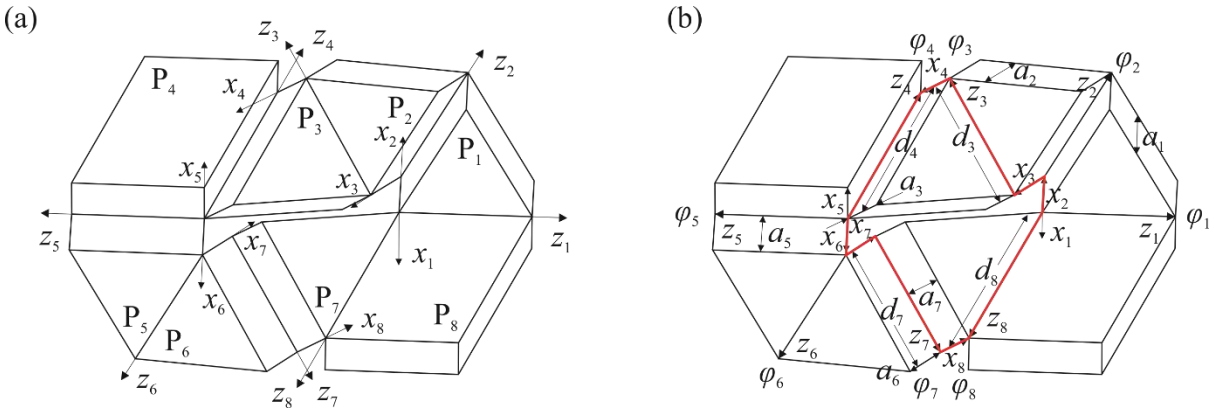

Figure 5.3 Setting up D-H notation on a thick-panel 8R element. (a) Eight coordinate systems are set up on a partially folded 8R. (b) The 8R element and its equivalent linkage (in red).

Since the 8R element consists of isosceles triangles and parallelograms of the same thickness, the geometric conditions of its equivalent linkage are listed as follows.

$$a_{12} = a_{23} = a_{34} = a_{56} = a_{67} = a_{78} = a\,,\ a_{45} = a_{81} = 0 \tag{5.3a}$$

$$\alpha_{12} = \alpha_{67} = \alpha_{78} = -\alpha\,,\ \alpha_{23} = \alpha_{34} = \alpha_{56} = \alpha\,,\ \alpha_{45} = \pi - \alpha\,,\ \alpha_{81} = \alpha - \pi \tag{5.3b}$$

$$d_1 = d_2 = d_5 = d_6 = 0\,,\ d_3 = d_7 = 2d\cos\alpha\,,\ d_4 = d_8 = -d \tag{5.3c}$$

where a is the thickness of each panel, α $(0 < \alpha < \frac{\pi}{2})$ is the base angle of the isosceles triangle, and d is the equal side length of an isosceles triangle in Figure 5.3(a).

Let $\mathbf{T}_{i(i+1)}$ be a 4×4 homogenous transformation matrix between the coordinate systems at joints i and $i+1$ ($i+1$ is replaced by 1 if $i+1>8$).

$$\mathbf{T}_{i(i+1)} = \begin{bmatrix} \cos\theta_i & \sin\theta_i & 0 & -a_i \\ -\sin\theta_i\cos\alpha_{i(i+1)} & \cos\theta_i\cos\alpha_{i(i+1)} & \sin\alpha_{i(i+1)} & -d_i\sin\alpha_{i(i+1)} \\ \sin\theta_i\sin\alpha_{i(i+1)} & -\cos\theta_i\sin\alpha_{i(i+1)} & \cos\alpha_{i(i+1)} & -d_i\cos\alpha_{i(i+1)} \\ 0 & 0 & 0 & 1 \end{bmatrix} \tag{5.4}$$

Also, the inverse of $\mathbf{T}_{i(i+1)}$ can be taken as

$$\mathbf{T}_{(i+1)i} = \mathbf{T}_{i(i+1)}^{-1} = \begin{bmatrix} \cos\theta_i & -\cos\alpha_{i(i+1)}\sin\theta_i & \sin\alpha_{i(i+1)}\sin\theta_i & a_i\cos\theta_i \\ \sin\theta_i & \cos\alpha_{i(i+1)}\cos\theta_i & -\sin\alpha_{i(i+1)}\cos\theta_i & a_i\sin\theta_i \\ 0 & \sin\alpha_{i(i+1)} & \cos\alpha_{i(i+1)} & d_i \\ 0 & 0 & 0 & 1 \end{bmatrix} \tag{5.5}$$

For the 8R closed chain, the loop closure equation is

$$\mathbf{E} = \mathbf{T}_{21}\mathbf{T}_{32}\mathbf{T}_{43}\mathbf{T}_{54} - \mathbf{T}_{18}^{-1}\mathbf{T}_{87}^{-1}\mathbf{T}_{76}^{-1}\mathbf{T}_{65}^{-1} = \mathbf{0}_{4\times4} \tag{5.6}$$

where $\mathbf{0}_{4\times4}$ is a null matrix.

5.2 Units consisting of four 8R elements

The 8R element has, in general, two DoFs. However, a single-DoF unit can be created by connecting them properly. Combining four 8R elements in different topologies, two deployable units can be created, which are hereafter termed unit I and unit II, respectively.

5.2.1 Topology of unit I

The formation and connectivity of unit I are demonstrated in Figure 5.4. In Figure 5.4(a), a topological graph $\mathcal{G} = (V, E)$ is plotted on the blue 8R element A to demonstrate the connectivity of panels. It is set up based on Davies's convention (Davies, 1981) where solid dots (vertices), $V = \{A_1, A_2, ..., A_8\}$, represent rigid panels, and the lines connecting the vertices, $E = \{a_1, a_2, ..., a_8\}$, represent revolute joints. Each line allows one DoF. If a revolute joint is placed on the top surface of a pair of adjacent panels, i.e., it is a valley fold, a dashed line is drawn to connect the adjacent dots. Otherwise, a solid line is used for a mountain fold.

Now flipping the blue 8R element horizontally and then rotating it by 2α anticlockwise yields the yellow 8R element *B* in Figure 5.4(b). All the mountain folds turn into valley folds after flipping, and vice versa. For instance, line a_1 is a valley fold in *A*, and it turns into a mountain fold in *B* after the operations, represented by line b_1.

After that, second copies of elements *A* and *B* are created and named elements *C* and *D*, respectively. All four elements can then be connected to form unit I. Element *B* is firstly connected to element *A* by superimposing hinges that accommodate revolute joints b_1 and b_2 on the ones that accommodate joints a_7 and a_8, as shown in Figure 5.4(c). As a result, panels A_6, A_7 and A_8 merge with panels B_8, B_1 and B_2, respectively. Similarly, *C* and *D* are connected to *A* and *B* via merging corresponding hinges and panels. This leads to the creation of unit I in Figure 5.4(d), where the green panels, including the parallelogram panel at the centre, are formed by merging those overlapping ones. Note that in unit I, all the mountain and valley folds remain as they are in each element.

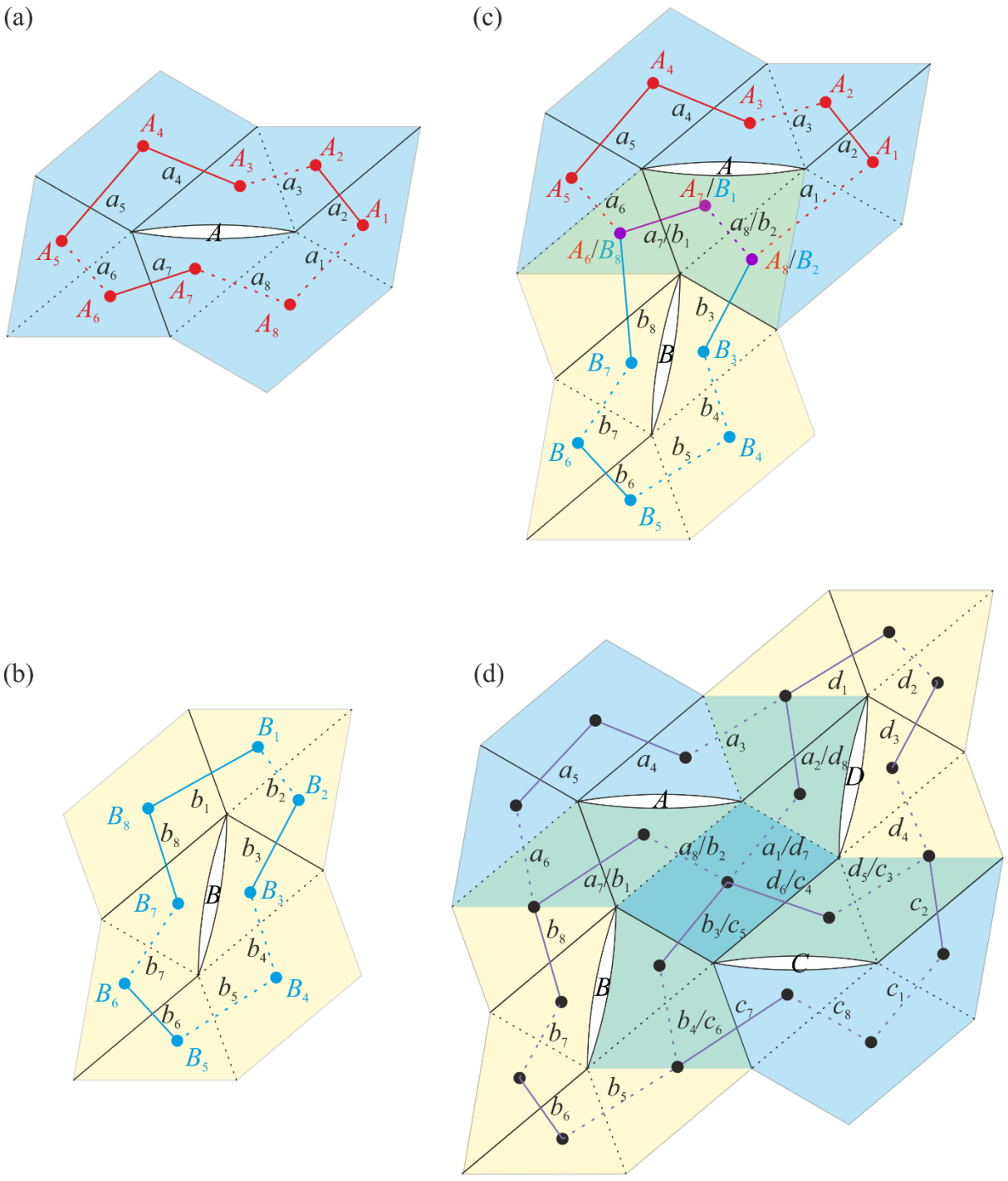

Figure 5.4 Formation of unit I with four 8R elements. (a)-(b) Elements *A* and *B* and their topological graphs. (c) Connection of elements *A* and *B* with overlapping panels and joints merged. (d) Formation of unit I and its topological graph.

In unit I where the four 8R elements combine, some panels and revolute joints are merged. Around merged revolute joints, the dihedral angles of two facets are equal. For instance, joints b_1 and b_2 are merged with a_7 and a_8, respectively, marked as a_7/b_1 and a_8/b_2 in Figure 5.4(d). Hence, $\varphi_{b1} = \varphi_{a7}$, $\varphi_{b2} = \varphi_{a8}$ and also

$$\begin{cases} \varphi_{a1} = \varphi_{d7} \\ \varphi_{a2} = \varphi_{d8} \end{cases}, \begin{cases} \varphi_{b1} = \varphi_{a7} \\ \varphi_{b2} = \varphi_{a8} \end{cases}, \begin{cases} \varphi_{c3} = \varphi_{d5} \\ \varphi_{c4} = \varphi_{d6} \end{cases}, \begin{cases} \varphi_{b3} = \varphi_{c5} \\ \varphi_{b4} = \varphi_{c6} \end{cases}. \tag{5.7}$$

Now, the overall DoF of unit I can be examined. Since each 8R element has, in general, 2 DoFs, the rest of the dihedral angles in *A* are defined if the angles φ_{a4} and φ_{a5} are inputs to element *A*. Two pairs of angles, φ_{a7} and φ_{a8} as well as φ_{a1} and φ_{a2}, are then passed on to define the configurations of its neighbouring elements *B* and *D*, respectively. After that, a pair of dihedral angles, φ_{b3} and φ_{b4}, from *B* and another pair φ_{d5} and φ_{d6} from *D* provide inputs to define the configuration of element *C*. However, the 8R element *C* requires only two inputs to be fully defined instead of four. Hence, there must be some kinematic constraints that relate these two pairs of inputs, which could lead to a reduction of overall DoF. Besides, the Kutzbach criterion can be applied to estimate the number of DoF of the unit. Since it has 21 rigid panels connected by 24 revolute joints,

$$\text{DoF} = 6(n-1) - 5j = 6 \times (21-1) - 5 \times 24 = 0. \tag{5.8}$$

The unit is likely to be an overconstrained mechanism if it is mobile, which will be proved in the next section.

5.2.2 Kinematics of unit I

All elements forming unit I are based on element *A*, and thus, it is plausible to argue that the motions of the four elements are coordinated such that each moves along the same motion path. The dihedral angles around the corresponding revolute joints in each 8R are therefore the same, i.e.,

$$\varphi_{ai} = \varphi_{bi} = \varphi_{ci} = \varphi_{di} \ (i = 1, 2, \ldots, 8). \tag{5.9}$$

Combining the constraints in Eqn. (5.7) and (5.9) give

$$\varphi_1 = \varphi_7, \ \varphi_2 = \varphi_8, \ \varphi_3 = \varphi_5, \ \varphi_4 = \varphi_6 \tag{5.10}$$

for each element. Replacing the dihedral angles with kinematic variables using Eqn. (5.2) and then substituting these variables into the loop closure equation (5.6) results in a matrix equation with four variables. Simplifying the (1,1) term in matrix **E** yields

$$\begin{aligned}\mathbf{E}_{(1,1)} = -\frac{3}{8}\{&-\sin\varphi_2 \sin\varphi_3 + \cos\varphi_4(-2\sin\varphi_1 + \sin\varphi_2 + \cos\varphi_1 \sin\varphi_2)\sin\varphi_3 \\ &- \cos\varphi_1 \sin\varphi_2 \sin\varphi_3 + \sin\varphi_1 \sin\varphi_4 + \cos\varphi_3 \sin\varphi_1 \sin\varphi_4 \\ &+ 2\cos\varphi_1 \sin\varphi_2 \sin\varphi_4 - 2\cos\varphi_3 \sin\varphi_2 \sin\varphi_4 \\ &+ \cos\varphi_2 \sin\varphi_1[2\sin\varphi_3 - (1+\cos\varphi_3)\sin\varphi_4]\} = 0\end{aligned} \tag{5.11}$$

Denoting $t_i = \tan\frac{\varphi_i}{2}$, and considering the following trigonometric functions,

$$\sin\varphi_i = \frac{2t_i}{1+t_i^2}, \ \cos\varphi_i = \frac{1-t_i^2}{1+t_i^2}, \tag{5.12}$$

Eqn. (5.11) can be further simplified into

$$\frac{6(t_1t_2 - t_3t_4)\left[t_2(t_3 - t_4) + t_1t_4\right]}{(1+t_1^2)\,(1+t_2^2)\,(1+t_3^2)\,(1+t_4^2)} = 0 \tag{5.13}$$

where $t_i \geq 0$ for $0 \leq \varphi_i \leq \pi$ throughout the range of motion of the elements. There are two possible sets of solutions:

$$t_1t_2 - t_3t_4 = 0 \tag{5.14a}$$

or

$$t_2(t_3 - t_4) + t_1t_4 = 0 \tag{5.14b}$$

Similarly, simplifying the (3,3) term in the matrix $\mathbf{E}$ yields

$$\begin{aligned}\mathbf{E}_{(3,3)} = -\frac{3}{16}\{&2(\sin\varphi_1 - \sin\varphi_3)[2\cos(\varphi_2 + \frac{\varphi_4}{2})\sin\frac{\varphi_4}{2} - \sin\varphi_4] \\ &+ \cos\varphi_1[1 + \cos\varphi_2(\cos\varphi_4 - 1) - \cos\varphi_4 - 4\sin\varphi_2\sin\varphi_4] \\ &+ \cos\varphi_3[\cos\varphi_2 + \cos\varphi_4 - \cos\varphi_2\cos\varphi_4 + 4\sin\varphi_2\sin\varphi_4 - 1]\} = 0\end{aligned} \tag{5.15}$$

Introducing t_i into Eqn. (5.15) results in

$$\frac{3t_2t_4(t_3 - t_1)\left[4(t_1 + t_3) - 2(t_2 + t_4) + 2t_1t_3(t_2 + t_4) - t_2t_4(t_1 + t_3)\right]}{2\,(1+t_1^2)\,(1+t_2^2)\,(1+t_3^2)\,(1+t_4^2)} = 0 \tag{5.16}$$

For (5.16) to hold during the full range of motion, $t_2 \neq 0$ and $t_4 \neq 0$. There are two possible sets of conditions.

$$t_3 - t_1 = 0 \tag{5.17a}$$

or

$$4(t_1 + t_3) + 2t_1t_3(t_2 + t_4) - 2(t_2 + t_4) - t_2t_4(t_1 + t_3) = 0 \tag{5.17b}$$

To comply with the loop closure equation, Eqn. (5.14) and (5.17) need to be satisfied simultaneously. Four combinations are possible.

When Eqn. (5.14a) and (5.17a) are satisfied, one can easily obtain the following relationships

$$t_3 = t_1 \text{ and } t_4 = t_2 \tag{5.18}$$

Substituting relationships (5.18) into the other terms in matrix **E** and letting all of them equal zero, another relationship can be obtained, which is

$$t_2 = 2t_1 \tag{5.19}$$

When Eqn. (5.14a) and (5.17b) are satisfied, $t_1 = \frac{t_3 t_4}{t_2}$ can be obtained from Eqn. (5.14a). Substituting it into Eqn. (5.17b) yields

$$-\frac{\left(t_2 - 2t_3\right)\left(t_2 + t_4\right)\left(2 + t_3 t_4\right)}{t_2} = 0 \tag{5.20}$$

Since $t_i \geq 0$, the only set of solutions is

$$t_2 = 2t_3 \text{ and } t_4 = 2t_1 \tag{5.21}$$

Again, substituting Eqn. (5.21) into the other terms in matrix **E**, $t_1 = t_3$ and $t_2 = t_4$ can be obtained, which are as same as Eqn. (5.18).

For the other two remaining combinations, the sets of solutions obtained are

$$t_3 = t_1,\ t_4 = t_2 \text{ and } t_2 = 2t_1, \tag{5.22}$$

which are identical to the solutions given by Eqn. (5.18) and (5.19). Therefore, all four combinations of equations result in the same set of solutions. Writing them in terms of dihedral angles, one can obtain

$$\varphi_3 = \varphi_1,\ \varphi_4 = \varphi_2,\ \cos\alpha \tan\frac{\varphi_2}{2} = \tan\frac{\varphi_1}{2} \tag{5.23}$$

Finally, combining Eqn. (5.10) and (5.23), the kinematic relationship amongst dihedral angles of one 8R element in unit I can be revealed.

$$\varphi_1 = \varphi_3 = \varphi_5 = \varphi_7,\ \varphi_2 = \varphi_4 = \varphi_6 = \varphi_8,\ \cos\alpha \tan\frac{\varphi_2}{2} = \tan\frac{\varphi_1}{2} \tag{5.24}$$

A single input, e.g., φ_1, defines the configurations of all four elements forming the unit. All motions within each 8R element are eliminated except the skew-symmetric one. It has therefore a single DoF. The unit is an overconstrained mechanism since the Kutzbach criterion predicts that it would have zero mobility. An input-output kinematic curve determined by Eqn. (5.24) is shown in Figure 5.5 when the base angle α is set to $7\pi/18$.

A prototype was constructed using 10mm thick PVC panels to demonstrate the deploying sequence of unit I, which is shown alongside the kinematic curve in Figure 5.5. In addition, a video is included in the *Supplementary Materials* to demonstrate the single-DoF motion of unit I. It can be observed that the folded package contains no voids. Define the surface footprint as the projected area of the unit along the normal direction of the surface of a panel. The surface footprint of a fully deployed unit I consists of 14 isosceles triangles and seven parallelograms. When it is fully folded into a compact bundle as shown in the left bottom corner of Figure 5.5, its surface footprint consists of two isosceles triangles and one parallelogram. Thus, the deployment ratio of unit I, which is the ratio between the surface footprints of expanded and folded configurations, is 7:1.

The total volume of unit I is the same in both fully deployed and packaged states because there is no void while packaged. Therefore, the smaller the surface footprint when packaged, the taller the package. Its height depends on the thickness of the panels *a*.

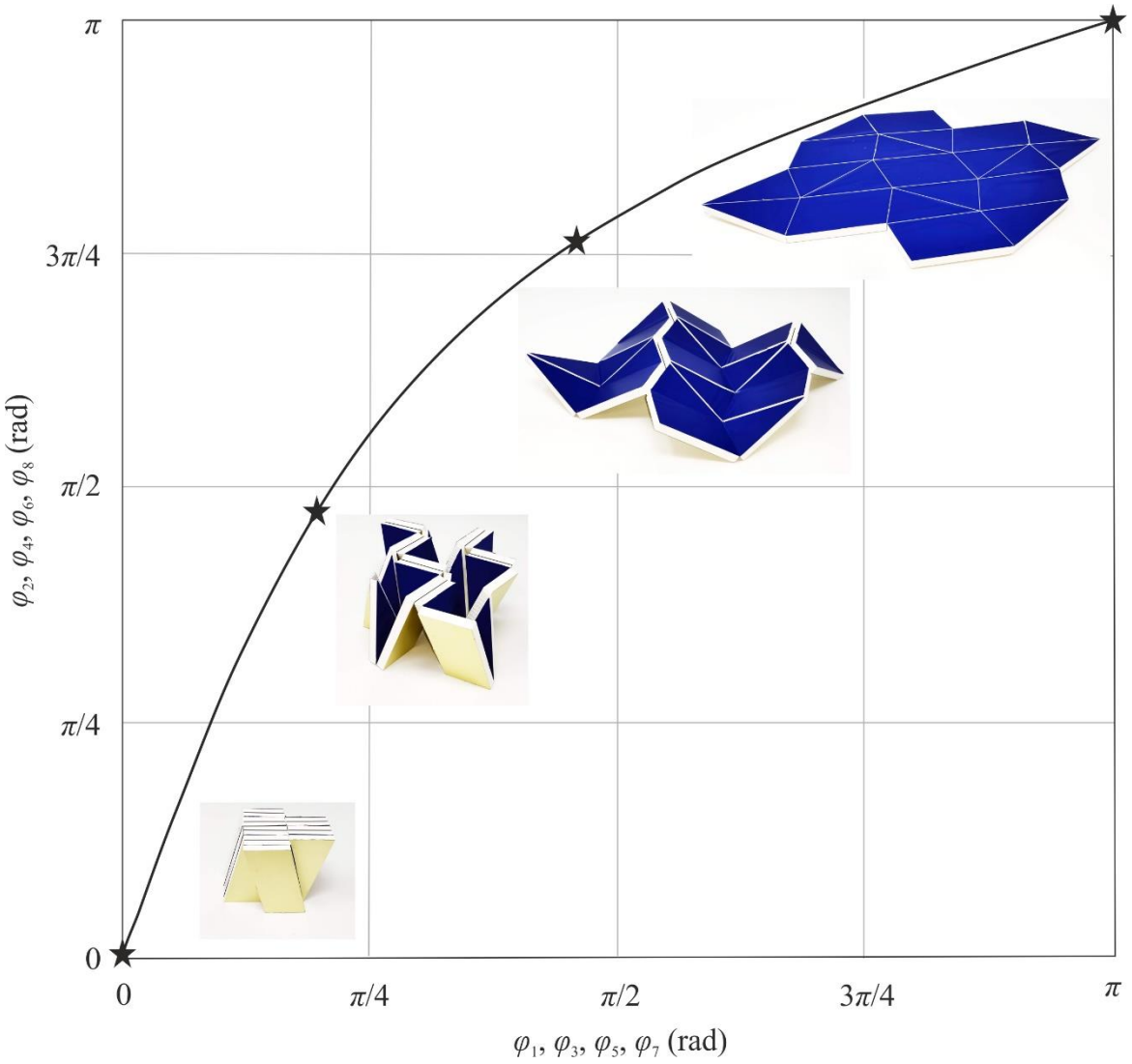

Figure 5.5 Kinematic relationship of dihedral angles in one 8R element of unit I with $\alpha = 7\pi/18$.

5.2.3 Topology of unit II

The formation of unit II is given in Figure 5.6. Element *A* in Figure 5.6(a) is identical to element *A* in unit I. Rotating it by π results in the 8R element *F* shown in Figure 5.6(b). Copies of elements *A* and *F* are named elements *G* and *H*, respectively. Elements *A* and *F* are then connected through overlapping panels and merging joints, as shown in Figure 5.6(c). Bringing in elements *G* and *H* leads to the formation of unit II in Figure 5.6(d), in which the darker-coloured panels are formed by merging those overlapping ones.

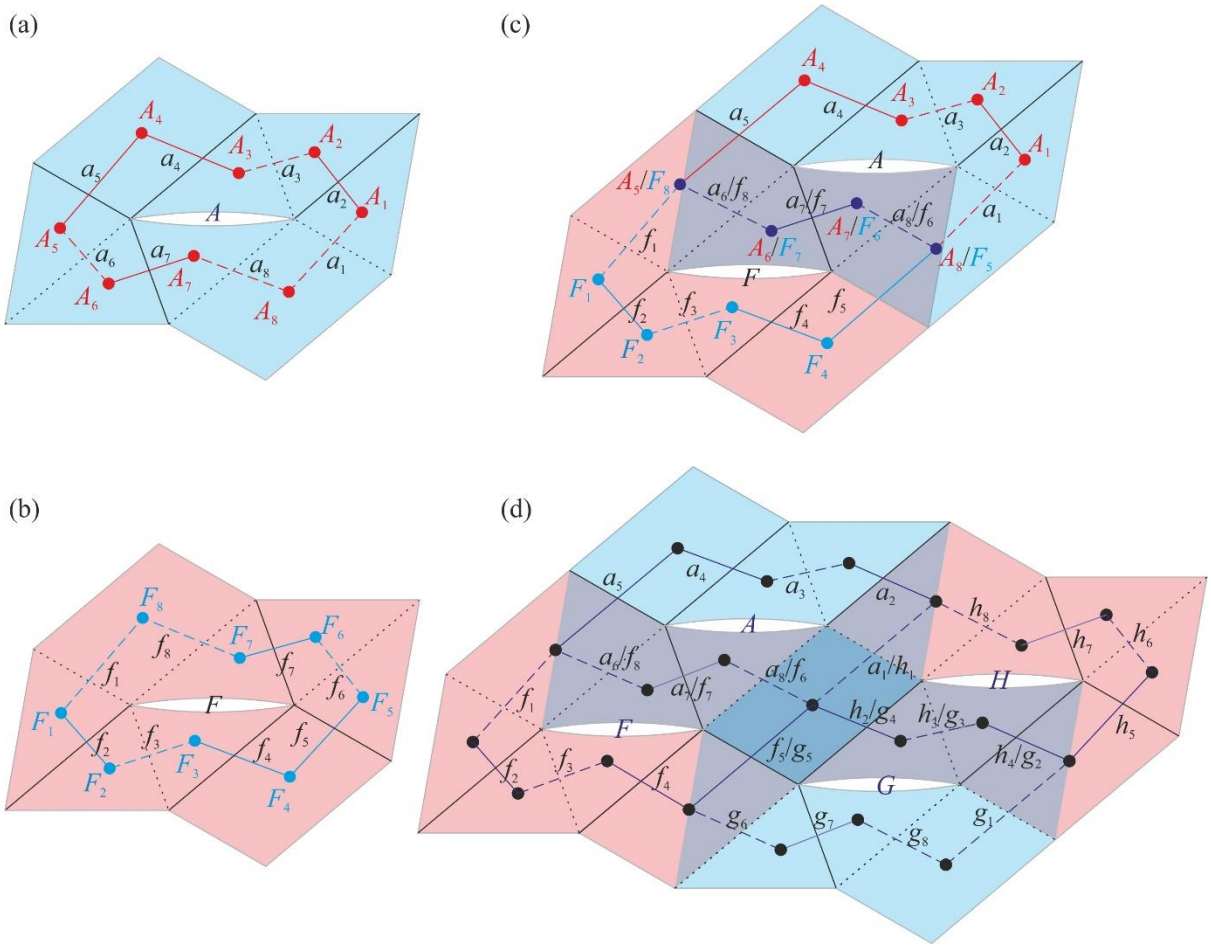

Figure 5.6 Formation of unit II with four 8R elements. (a)-(b) Elements *A* and *F* and their topological graphs. (c) Connection of elements *A* and *F* with overlapping panels and joints merged. (d) Formation of unit II and its topological graph.

Since the overlapping panels in unit II share the same revolute joints, the dihedral angles must meet the following conditions:

$$\varphi_{a1}=\varphi_{h1},\ \begin{cases}\varphi_{f6}=\varphi_{a8}\\ \varphi_{f7}=\varphi_{a7}\\ \varphi_{f8}=\varphi_{a6}\end{cases},\ \varphi_{f5}=\varphi_{g5},\ \begin{cases}\varphi_{h2}=\varphi_{g4}\\ \varphi_{h3}=\varphi_{g3}\\ \varphi_{h4}=\varphi_{g2}\end{cases} \tag{5.25}$$

Combining the constraints in Eqn. (5.9) and (5.25) gives

$$\varphi_2=\varphi_4,\ \varphi_6=\varphi_8 \tag{5.26}$$

for each 8*R* element.

5.2.4 Kinematics of unit II

It is possible to set up loop closure equations in matrix form for unit I. Equation (5.26) reduces the number of variables in the loop closure equation from eight to six, i.e., φ_1, φ_2, φ_3, φ_5, φ_6 and φ_7, instead of four as in unit I. We are, however, unable to simplify the closure equations because of the large number of variables, and thus, we opt for a numerical approach (Müller, 2018; Gan & Pellegrino, 2006).

The details of the numerical method are provided in *Appendix*. Starting from the fully packaged state, we built the Jacobian matrix of unit II based on the loop closure equation for each 8R element and the global constraints that are imposed when elements are connected. It was found that, although it is rank-deficient with nullity of four, only one finite mechanism exists, corresponding to the motion where all four elements move in unison. In the subsequent partially deployed states, the rank of Jacobian matrix is 23, indicating that unit II is a single-DoF mechanism. The Jacobian matrix at a fully deployed state again is rank-deficient with nullity of four, but only one finite mechanism exists, enabling it to fold up.

A data package enclosing five files can be found in the link for the numerical calculations https://www.dropbox.com/sh/pteiwtvarhb32wq/AABoSIR1k5gUNGioHC9QTxYha?dl=0. The time history of all kinematic variables in unit II is stored in "theta_time_history.mat", whose data can be reproduced by running "unit_II_numerical_rspa.m".

A motion curve is plotted in Figure 5.7 to illustrate the kinematic relationship of the dihedral angles in unit II when the base angle of an isosceles triangle $\alpha = 7\pi/18$. The kinematic relationships in Eqn. (5.24) are also valid for unit II. The same skew-symmetric motion can be observed in all 8R elements. Alongside the motion path, some snapshots of a physical model

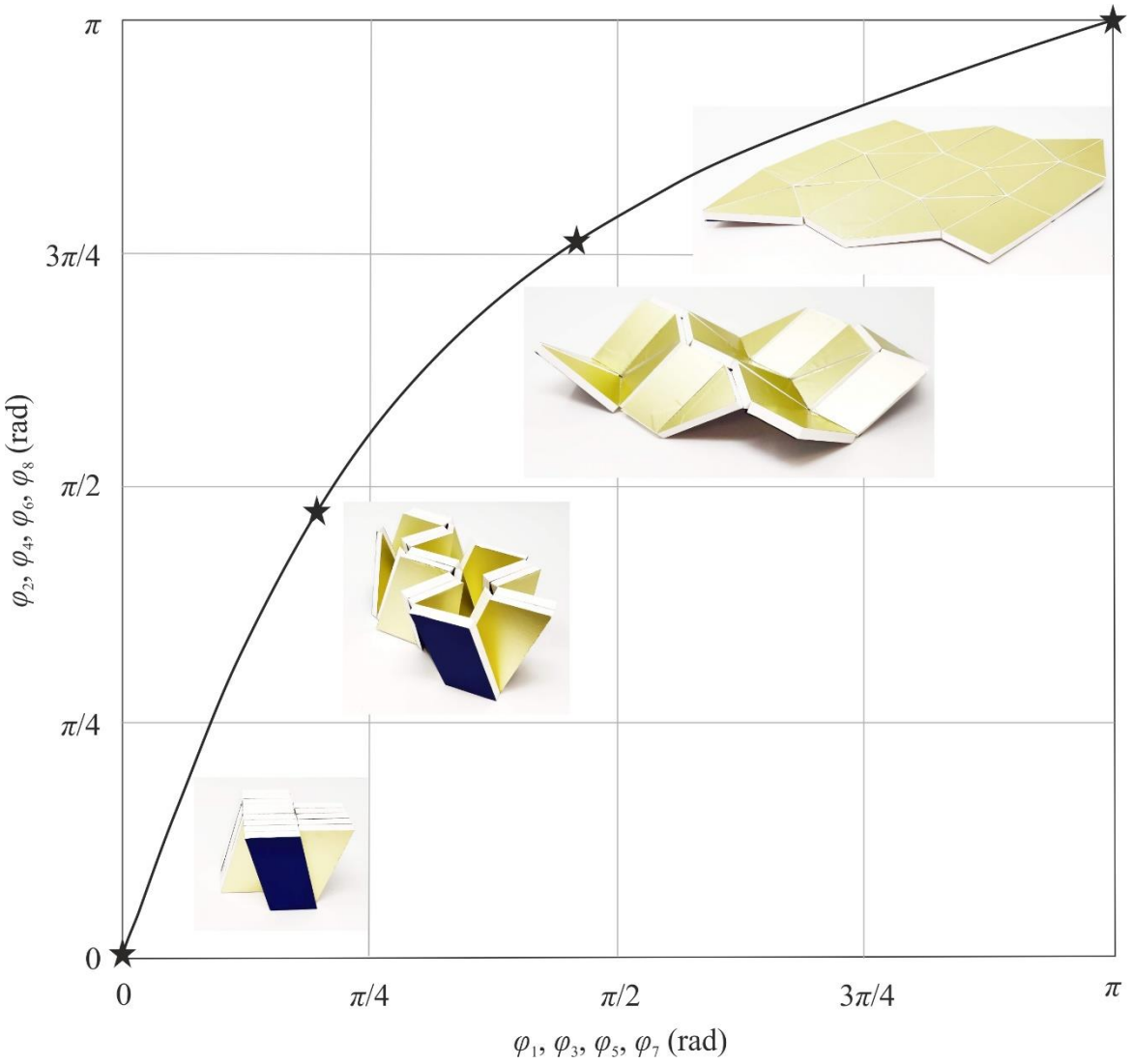

Figure 5.7 Kinematic relationship of dihedral angles in one 8R element of unit II with $\alpha = 7\pi/18$. The deployment sequence of a physical model is shown alongside the motion curve.

are given to demonstrate its deployment sequence. A video capturing the single-DoF motion of unit II is also included in the *Supplementary Materials*. Furthermore, the projected footprints of a fully deployed and a fully folded unit II are identical to those of unit I.

5.3 Geometric constraints

5.3.1 Geometric constraints due to physical interference

Figure 5.8(a) demonstrates a partially folded 8R element along its skew-symmetric motion path, whose motion is described by the equations in (5.24). The positions of M_4, N_4, S_4 and M_8, N_8, R_8 can be easily acquired in the coordinate systems x_4-y_4-z_4 and x_8-y_8-z_8, respectively. The corresponding normal vectors of the planes $M_4N_4S_4$ and $M_8N_8R_8$ can be obtained, which can then be transformed into a common coordinate system using the transformation matrix defined in Eqn. (2.1). Throughout the motion profile described in (5.24), the two normal vectors are always linearly dependent on each other, indicating that the two facets $M_4N_4S_4$ and $M_8N_8R_8$ are always parallel even though the slit opens and closes. So are the normal vectors of the planes $N_4'N_4M_4M_4'$ and $N_8'N_8M_8M_8'$, which implies that the two planes are always parallel to each other as well. In the deployment process, the distance between the two planes $N_4'N_4M_4M_4'$ and $N_8'N_8M_8M_8'$, denoted as the slit distance p hereafter, is

$$p = \frac{4\cos\frac{\varphi_1}{2}\sin\frac{\varphi_1}{2}\cos\alpha(2\cos^2\alpha - 1)}{(\sin^2\alpha + \cos\varphi_1 \times \sin^2\alpha - 2)}a \tag{5.27}$$

It is positive when the two panels P_3 and P_7 do not have physical contact, and negative when P_3 and P_7 have physical interference. Since the denominator in Eqn. (5.27) is always less than zero with any $0 \le \varphi_1 \le \pi$ and $0 < \alpha < \pi/2$, the sign of the slit distance p depends on the numerator. In the numerator, all the terms are positive except $(2\cos^2\alpha - 1)$, which results in a negative slit distance p when $0 < \alpha < \pi/4$, a positive p when $\pi/4 < \alpha < \pi/2$ and a zero p throughout the deployment process if $\alpha = \pi/4$. In Figure 5.8(b), p/a is plotted against the full range of motion of the dihedral angle φ_1 with different base angles α of an isosceles triangle.

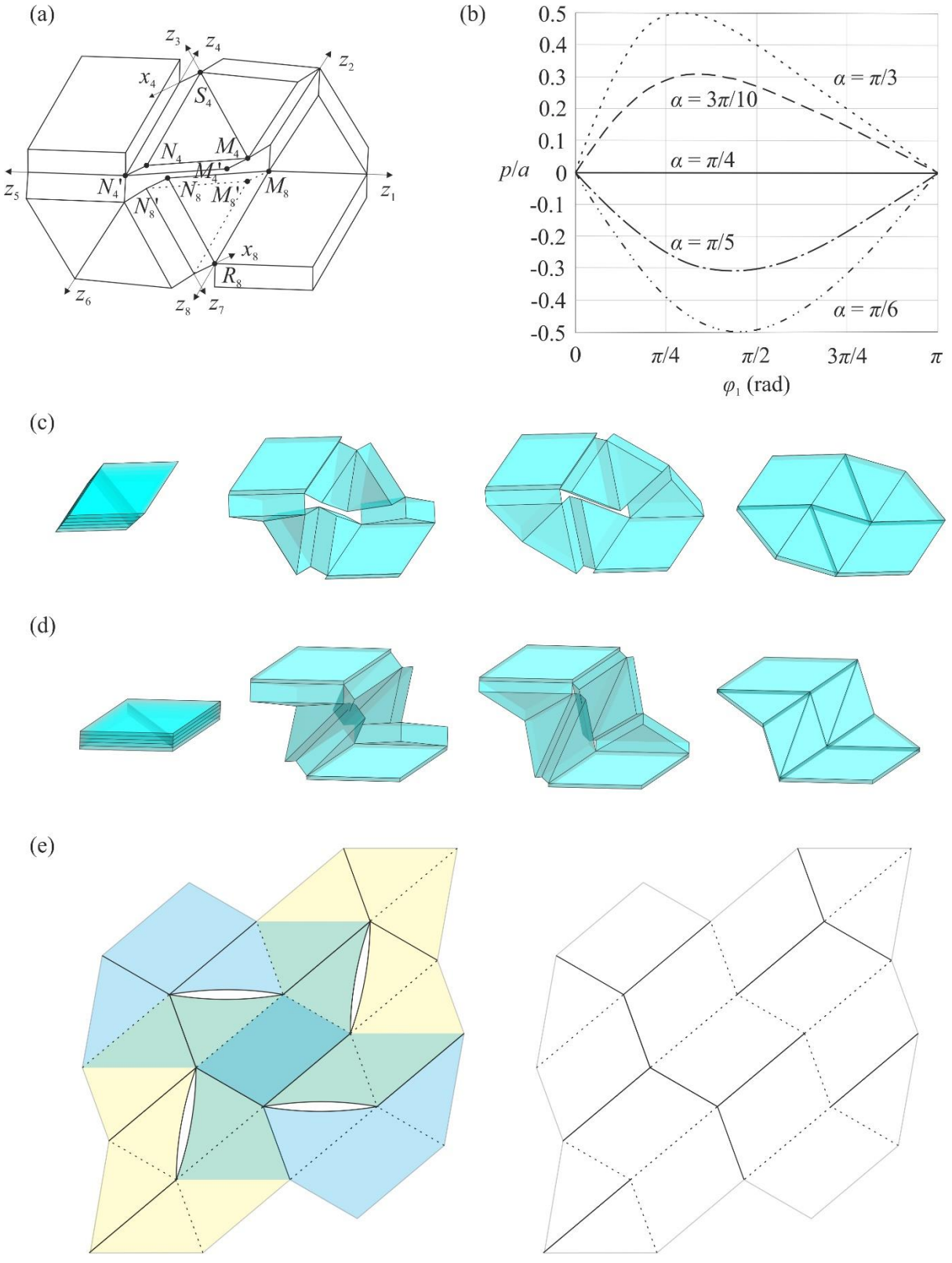

Figure 5.8 Skew-symmetrical deployments of 8R elements with various base angles α. (a) A partially folded 8R with $\alpha = 7\pi/8$. (b) p/a vs. φ_1 plots for various α. (c) Deployment sequence of an element with $\alpha = 3\pi/10$. No physical interference occurs. (d) Deployment sequence of an element with $\alpha = \pi/5$. Panels invade each other during deployment. (e) A comparison of origami patterns of unit I and the Miura-ori.

The deployment sequence of an 8R element with $\alpha = 3\pi/10$ is shown in Figure 5.8(c). The slit opens up when the element deploys from the fully packaged state and closes when it reaches the flat state. If $\alpha = \pi/5$, the deployment of the element involves penetration of the panels around the slit, which is given in Figure 5.8(d). This deployment cannot be initiated in reality. Both simulations were implemented in Solidworks®, in which panels were allowed to invade each other. Therefore, for an 8R element to be mobile with the skew-symmetry, $\pi/4 \leq \alpha < \pi/2$.

When an element is designed appropriately with p/a equal to or greater than zero, deployment of the units formed by such elements will also not encounter collisions amongst panels. This can be explained by looking at the units from a different perspective. Take unit I as an example. This unit can be treated as a modified Miura-ori where slits are introduced along the diagonals of some facets. Both unit I and its Miura-ori counterpart are shown in Figure 5.8(e). The folding of unit I mimics that of the Miura-ori except that the two triangular panels separated by a slit move apart during deployment, but they always remain parallel. As no panel collision occurs during the deployment of the Miura-ori, the same is true for unit I.

5.3.2 Geometric constraints due to flat foldability

Forming the 8R element and later the unit I and II with isosceles triangles, one may naturally ask whether any triangles can form a single-DoF array that is constructed by 8R elements. Folding along the creases from a flat surface to two compact stacks, the two pairs of triangles on the outer layers of the stacks merge into two quadrilaterals. Two geometric constraints shall be satisfied. First, reflections shall be taken about any creases regardless of mountain or valley creases. Secondly, the sector angles around any vertices must sum to 2π to form a flat deployable surface. Based on the constraints, two 8R elements are formed by arranging triangles with sector angles α_1, α_2 and α_3 in Figure 5.9, corresponding to two arrangements of

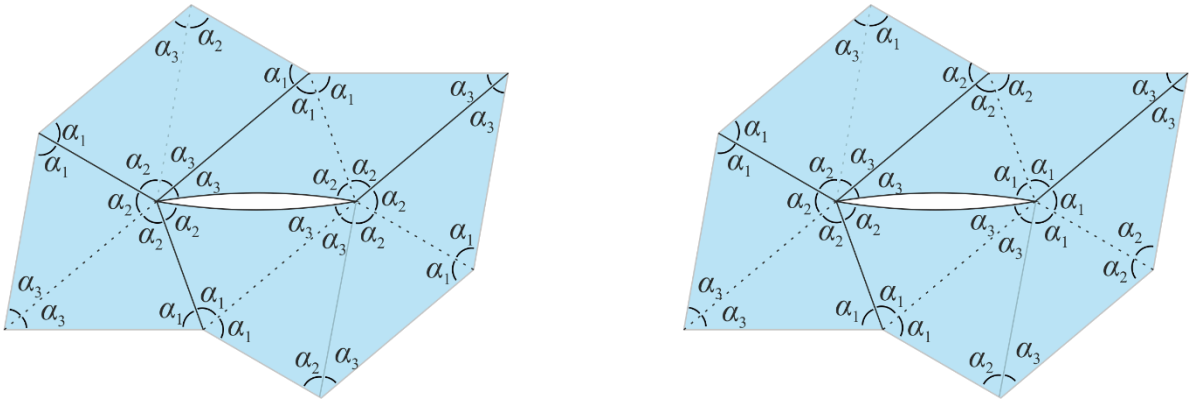

Figure 5.9 Two 8R elements are formed with different arrangements of triangles.

the triangles on the top and bottom layer in the folded stacks, whereas the same sector angle must be designed on both sides of a crease.

Around the two inner vertices where the slits start and end, the summation of the angles must be 2π,

$$4\alpha_2 + 2\alpha_3 = 2\pi \text{ and } 4\alpha_1 + 2\alpha_3 = 2\pi \tag{5.28}$$

Besides, the angles of a triangle are summed to π in Euclidean geometry, i.e., $\alpha_1 + \alpha_2 + \alpha_3 = \pi$. Together with Eqn. (5.28), α_1 must be equal to α_2 to tessellate a plane. In other words, only isosceles triangles can construct 8R elements and subsequently single-DoF units that can be folded from a flat surface.

5.4 Tessellation of unit I and unit II

The combinations of four 8R elements lead to the creation of two deployable units. These units can be further tessellated to form large deployable structures of flat profile that are capable of being folded into compact packages.

Let us consider two identical units I composed of equilateral triangles ($\alpha = \pi/3$) and rhombuses (a combination of two equilateral triangles) as shown in Figure 5.10(a). When the units are in motion, each element contains two sets of identical dihedral angles, $\varphi_1 = \varphi_3 = \varphi_5 = \varphi_7$ and $\varphi_2 = \varphi_4 = \varphi_6 = \varphi_8$, marked by red and black lines, respectively. Solid or dash lines indicate if the creases are on the bottom or top of the panels. Tessellating these two units with an overlapping region shown in green, the dihedral angles of the yellow unit are passed onto those in the blue unit as inputs. Thus, the resultant assembly retains a single DoF. There is more than one method to combine the two units. Another way of tessellation is illustrated in Figure 5.10(b). A physical model was made based on it and its deployment sequence is demonstrated in Figure 5.10(c).

Similarly, two units II can overlap to form larger assemblies with a single DoF as shown in Figure 5.11(a)-(b), where the blue unit is an inversion of the yellow one – in other words, the top and bottom creases are exchanged. Furthermore, the deployment sequence of a physical model based on Figure 5.11(b) is shown in Figure 5.11(c).

The tessellation in Figure 5.10(b) has an area of 44 triangles (24 equilateral triangles and ten rhombuses) when fully deployed. Its projected footprint in the fully folded states contains four triangles (two equilateral triangles and one rhombus), giving a deployment ratio of 11:1. The second tessellation in Figure 5.11(b) covers an area of 38 triangles (18 equilateral triangles and ten rhombuses) in its fully deployed state, which folds to a projected footprint of five triangles (three triangles and one rhombus), giving a deployment ratio of 38:5. It is, therefore, necessary to choose the design based on the particular requirements of the application.

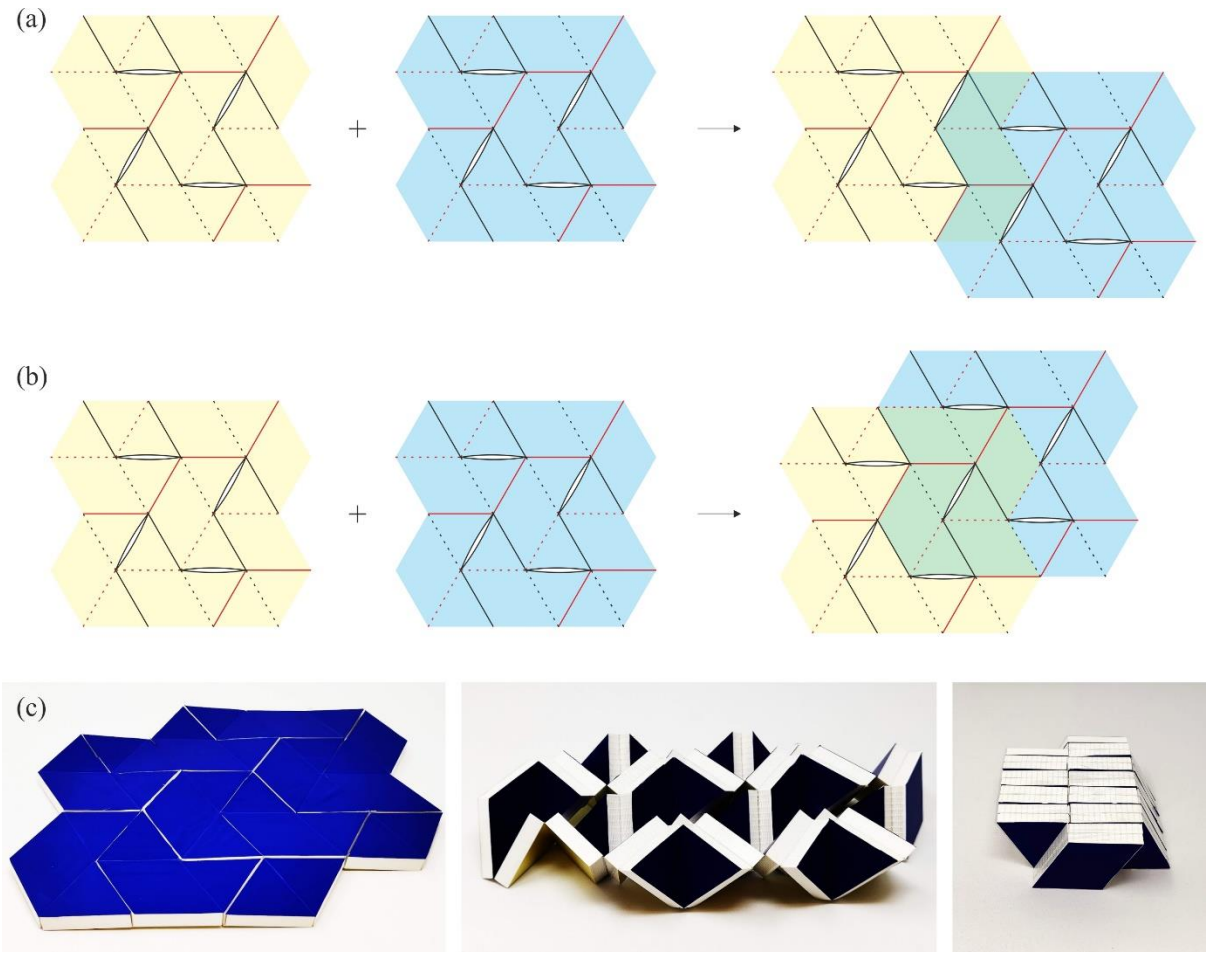

Figure 5.10 Tessellations of units I composed of equilateral triangles ($\alpha = \pi/3$) and rhombuses. (a) Four and (b) eight revolute joints are merged. (c) A physical prototype demonstrating the folding process of the tessellation in (b).

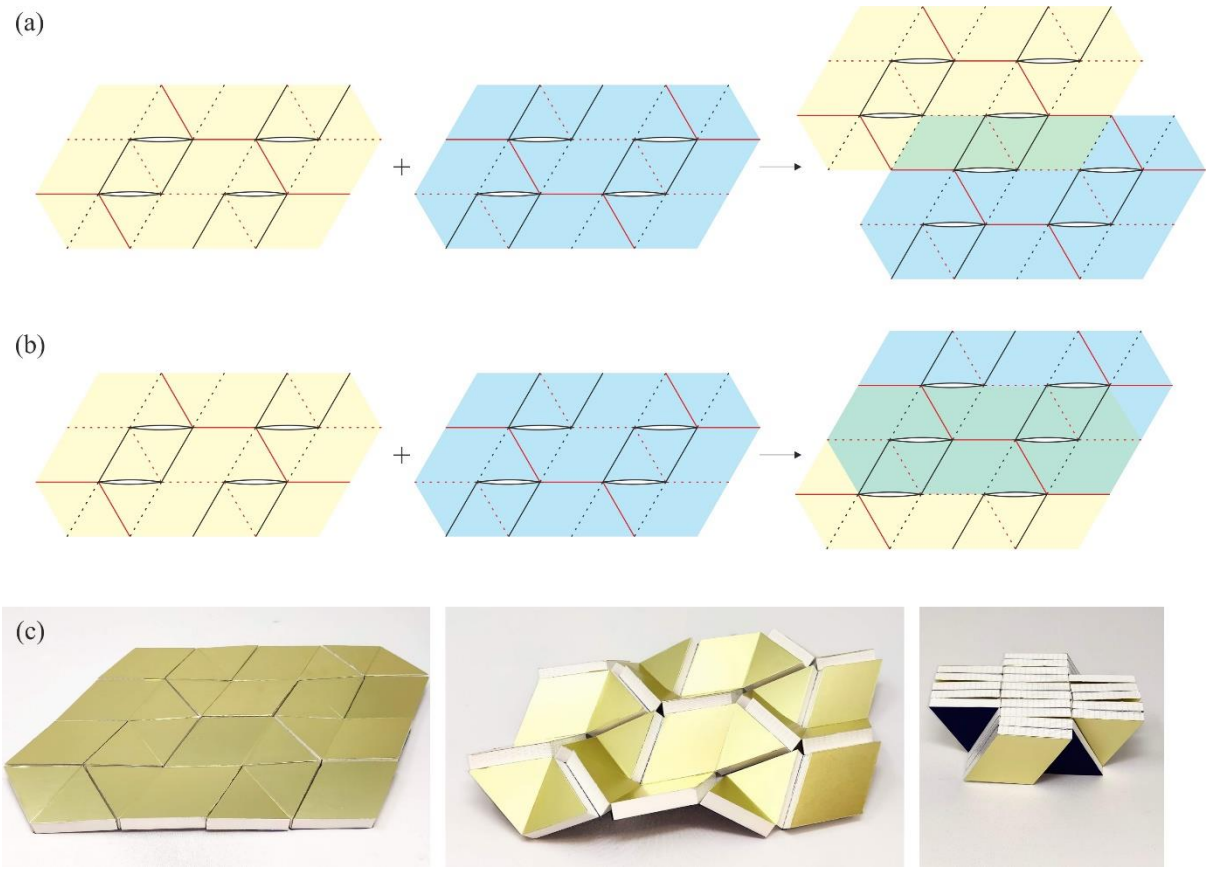

Figure 5.11 Tessellations of units II composed of equilateral triangles ($\alpha = \pi/3$) and rhombuses. (a) Three and (b) 14 revolute joints are merged. (c) A physical model demonstrating the folding process of the tessellation in (b).

Units I and II can also be mixed in a tessellation to form a single-DoF assembly as long as there are sufficient overlapping dihedral angles to pass inputs to adjacent units. Figure 5.12(a) shows an example. It is also possible to take a portion of a large assembly to make a new deployable array. Figure 5.12(b) is the deployment sequence of a physical model, which was created with the panels encircled by the green dotted dash lines from the tessellation in Figure 5.12(a). This approach offers freedom to designers to obtain large flat assemblies with a desirable deployment ratio.

Videos capturing the folding processes of the three tessellations are included in the *Supplementary Materials*.

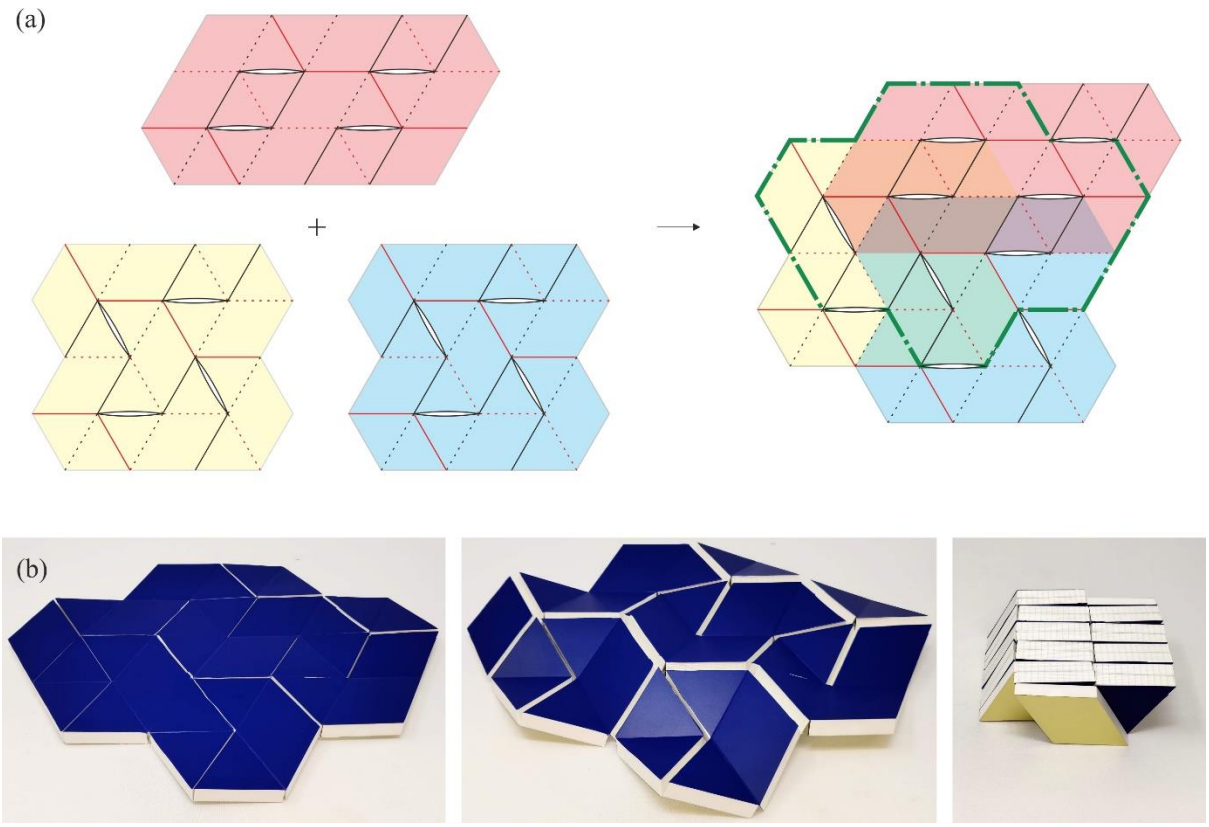

Figure 5.12 Tessellation containing a mixture of units I and II. (a) One unit II is combined with two units I. (b) Deployment sequence of a physical model that contains panels encircled by the green dotted dash line in (a).

5.5 Conclusion

In this chapter, a method is proposed to compactly fold arrays composed of two types of panels of uniform thickness. In modular construction, two deployable arrays were first created, namely, units I and II, each of which comprises four eight-panel closed-chain mechanisms. Though an 8R linkage usually has two DoFs in general, the units were proven to have a single DoF, and they can be folded from a flat array to compact bundles without any voids. A parametric study was carried out to provide precise design ranges that prevent the panels from physical interference during deployment. Furthermore, several units were combined to form larger flat arrays where single-DoF deployment and compact packaging properties were intact.

The single-DoF deployment considerably reduces control complexity, and the revolute joints amongst the panels are one of the simplest but most reliable mechanical connections. Although slits are introduced in the tessellation to facilitate folding, they are closed in the fully deployed state, leading to a flat, continuous and accurate surface on both the top and bottom sides. The versatility of the concept offers designers plenty of choices in terms of the number of panels and deployment ratios. The findings can be readily applied to the design of solar panels and reflectarray antennas for aerospace applications.

This work is also important in the theory of mechanisms. The units made of isosceles triangles are one of the examples where a kinematic loop consisting of linkages of multiple DoFs results in a single DoF. Other combinations may be possible, which can be studied in future work.

One of the drawbacks of our work is that the completed folded packages do not conform to the shape of a cuboid despite being compact without voids. Numerous methods can be used to make the folded volume closer to a cuboid. For instance, the corners can be trimmed off in the folded volume, but it may make the deployed shape less regular. Another approach is to use panels with shapes of rectangles instead of triangles and parallelograms, which will be detailed in Chapter 6.

CHAPTER 6

ARRAYS VIA MODULAR DESIGNS

In Chapter 5, a single-DoF assembly can be formed with triangular panels but the folded stacks cannot conform to the shape of a CubeSat despite being compact. In this chapter, we try to address this problem. Again a modular approach is taken in which we first identify the foldable modules, and then investigate how the modules can be tessellated to form large arrays with either a single DoF or a small number of DoFs. The number of stacks could be one, two or more, but they all contain no voids and conform to the shape of a cuboid.

6.1 Assembling kinematic loops of squares

Considering an eight-panel loop of square panels, an HC is drawn by the blue dotted dash lines in Figure 6.1(a). The creases and slits are placed accordingly. After merging the panels in the top and bottom layers of the stacks, a closed loop of six polygons is formed, labelled as P_1, P_2,…, P_6 in Figure 6.1(b). This is named a 6R element hereafter. The solid and dotted lines represent mountain and valley creases, respectively.

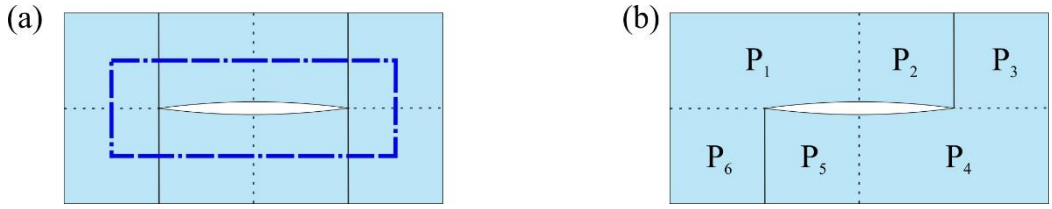

Figure 6.1 Forming a 6R kirigami pattern from squares. (a) An HC is drawn within eight squares. (b) A 6R element is formed after merging panels.

Converting the facets to panels of uniform thickness yields an assembly shown in Figure 6.2(a). The panels are connected by a revolute joint whose axis is along their bottom edge when it is a mountain crease, or along their top edge when it is a valley crease. Due to the orthogonality of creases, bifurcation occurs at the fully deployed configuration. The two horizontal creases in the 6R element shall be folded first such that the dihedral angles around the two joints go from π to 0 in Figure 6.2(b), followed by a synchronised single-DoF motion as a planar 4R linkage in Figure 6.2(c), where P_1 and P_6 move together as one link, so do P_3 and P_4. Finally, panel P_1 is folded onto P_4 with all the other panels sandwiched in-between compactly, as shown in Figure 6.2(d).

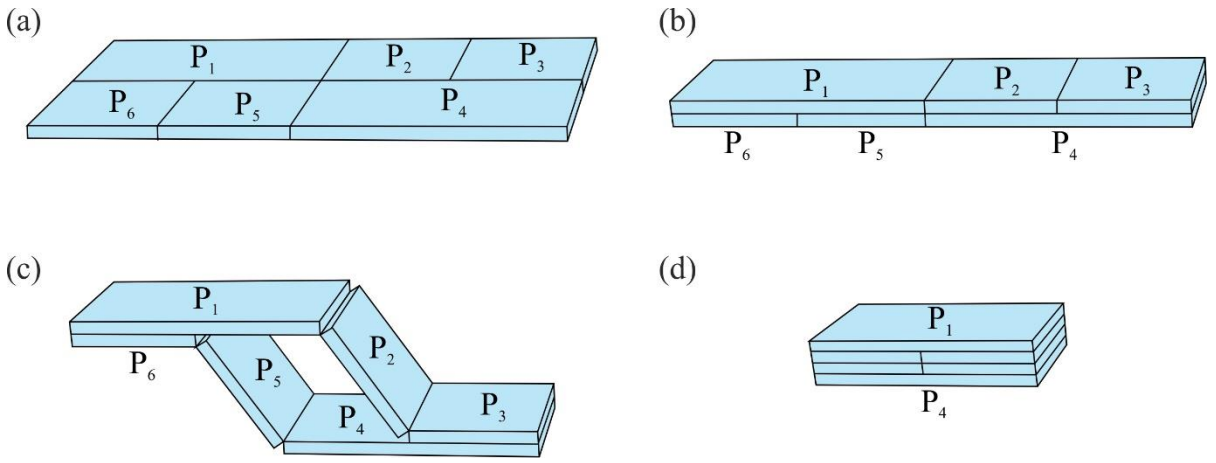

Figure 6.2 Stepwise folding of the thick-panel counterpart of the 6R element.

For a better illustration, coordinate systems are set up in a partially folded state in Figure 6.3, in which the *z*-axes are along the axes of revolute joints, and the *x*-axes are along the thickness direction of the panels. The *y*-axes are not shown in the figure but they can be obtained by the right-hand rule. The dihedral angle between adjacent panels with a common axis z_i is denoted as φ_i. Its motion can be modelled by a planar 4R linkage with equal length as shown by the red lines.

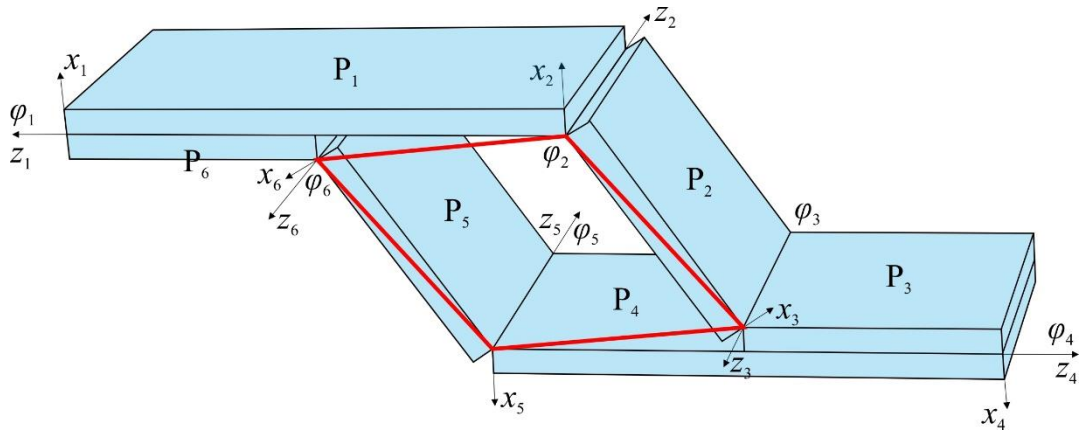

Figure 6.3 Coordinate systems are set up on a partially folded state of the 6R element.

The kinematics relationship of the dihedral angles can be summarised in Eqn. (6.1).

$$\varphi_1 = \varphi_4 = 0,\ \varphi_2 = \varphi_3 = \varphi_5 = \varphi_6\ (0 \le \varphi_2 \le \pi) \tag{6.1}$$

Despite the stepwise folding process and bifurcations, the 6R element behaves like a single-DoF assembly.

In Figure 6.4, several 6R elements are combined to form larger arrays. First, a blue 6R element *A* is taken. The panels and the creases are labelled as A_1, A_2, …, A_6, and a_1, a_2, …, a_6 as shown in Figure 6.4(a). Then, a yellow copy in an inversion of the blue one is made, where all the mountain creases turn into valley creases, and vice versa. After that, the blue and the yellow 6R elements are combined vertically in Figure 6.4(b) by superimposing the crease a_5 on b_1, and a_4 on b_2. As a result, panels A_6, A_5 and A_4 are merged with B_1, B_2 and B_3, and creases a_5 with b_1, a_4 with b_2, respectively. If taking another copy of element *A* and naming it as element *C*, it can be combined with *A* side by side by merging crease c_6 with a_3 in Figure 6.4(c). Now, if another copy of element *B* is taken and named element *D*, the four elements can be connected by the same approach where all mountain and valley folds remain as they are in each element. This leads to an array of four 6R elements in two rows and two columns where the green panels are formed by merging those overlapping ones, as shown in Figure 6.4(d).

In Figure 6.4(b), the kinematics of the 6R elements *A* and *B* are found to be synchronised if they are arranged in one column. The motion of the array remains single DoF and the bifurcation remains at the fully deployed state. However, it is found that placing the 6R elements side-by-side results in an extra DoF in the assembly as elements *A* and *C* can have independent motion paths. The horizontal creases including the merged ones a_3 and c_6 need to be folded completely first then the folding along the vertical creases can be initiated.

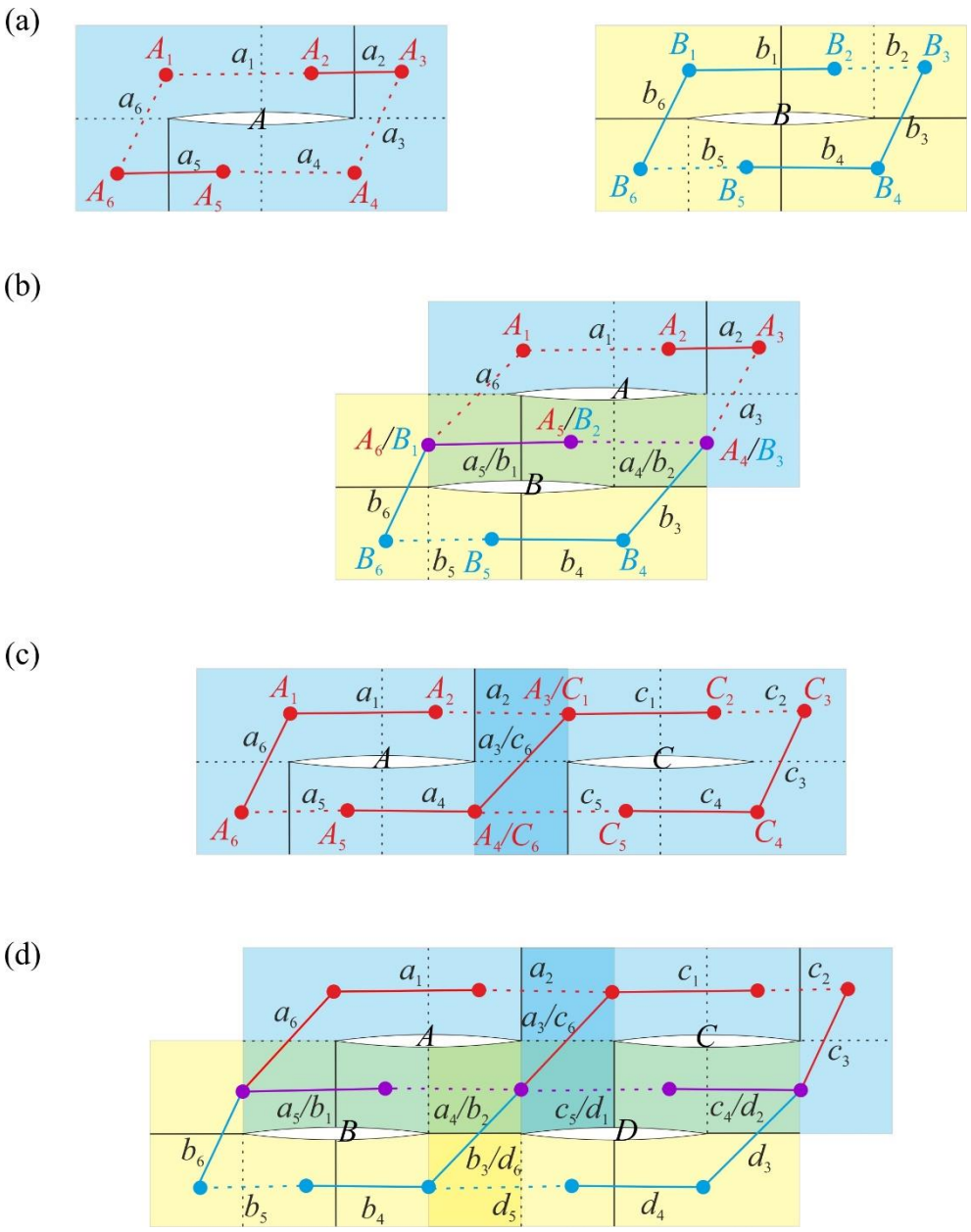

Figure 6.4 Combining several 6R elements with squares. (a) Two copies of the 6R element where the yellow element B is the inversion of the blue A. (b) Combining 6R elements A and B vertically. (c) Combining 6R elements A and C column-wise. (d) An array of four 6R elements in two rows and two columns.

In Figure 6.4(d), where four 6R elements are arranged in two rows and two columns, two DoFs are observed when it is in motion. A thick-panel prototype was constructed to demonstrate its stepwise folding sequence in Figure 6.5. It has an area of 22 squares (eight squares and seven rectangles) when fully deployed, and its projected footprint in the fully folded state contains

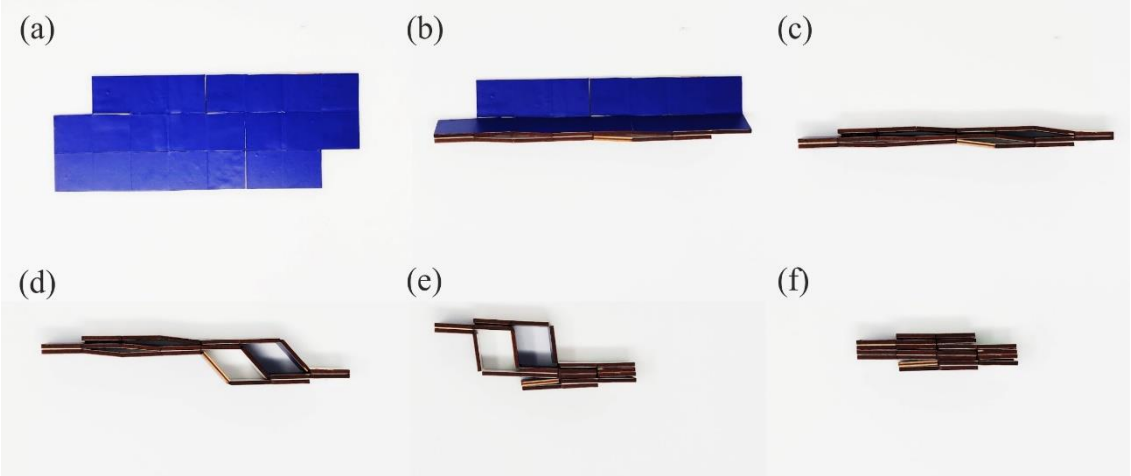

Figure 6.5 The stepwise folding sequence of an array of four 6R elements.

four squares (two squares and one rectangle), giving a deployment ratio of 11:2. More 6R elements can be added to extend the array in either row or column-wise direction, which will give a larger deployment ratio but also may result in more DoFs in the assembly. Nevertheless, the folded volume is compact and is more conforming to the shape of a CubeSat.

6.2 Case-specific modular designs

6.2.1 Module I and its tessellations

The Yoshimura pattern is a well-known origami pattern consisting of 6-crease vertices and triangular facets (Lang et al., 2018; Yoshimura, 1955), the sector angles around each vertex are defined as α, $\pi - 2\alpha$, α, α, $\pi - 2\alpha$, α. The pattern cannot be fully folded due to physical interference of facets if $\alpha > \pi/4$, and a void is inevitable in the folded state if $\alpha < \pi/4$. Only when $\alpha = \pi/4$ can the origami pattern be fully folded without voids. Adapting the special Yoshimura pattern where $\alpha = \pi/4$, module I is formed consisting of half-square triangles and squares, as shown in Figure 6.6(a), where mountain and valley creases are marked as solid and dotted lines, respectively (Yang & You, 2019).

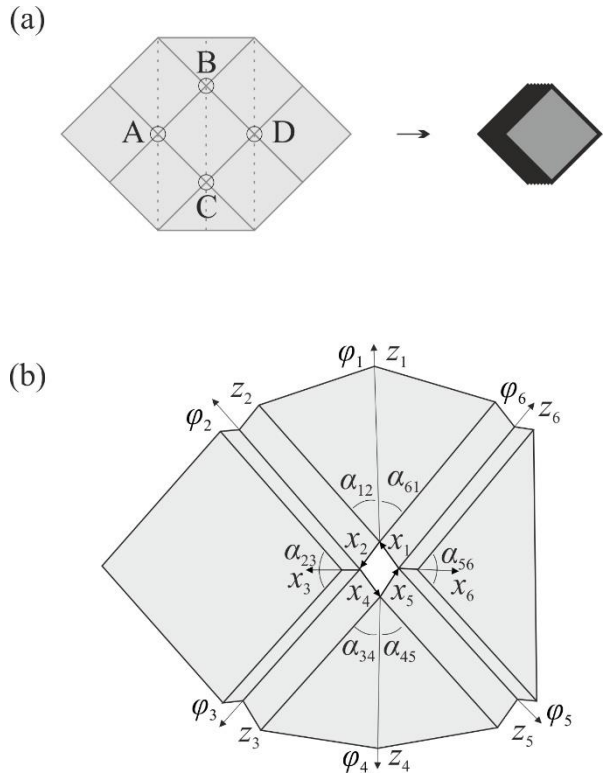

Figure 6.6 Crease pattern of module I and an enlarged view of one vertex constructed by thick panels. (a) The crease pattern is adapting a special Yoshimura pattern and the folded stack. (b) Setting up coordinate systems of the thick-panel assembly around vertex A.

It turns out that Module I can be constructed not only with paper of zero thickness but also with rigid panels of uniform thickness. Its thick-panel counterpart around vertex A in its partially folded state is plotted in Figure 6.6(b), in which coordinate systems are set up such that their *z*-axes are along the axes of revolute joints, and *x*-axes are along the thickness direction of the panels.

Kinematically it is a Bricard linkage with plane and line symmetry (Chen et al., 2015). The link length $a_{(i-1)i}$ measures the normal distance between axes z_{i-1} and z_i, positively along x_i. $\alpha_{(i-1)i}$ is the twist angle from axes z_{i-1} to z_i positively about x_i. Offset d_i is the distance between x_i to x_{i+1}, positively along z_i. The geometric parameters of its equivalent plane and line-symmetric Bricard linkage are listed in Eqn. (6.2).

$$a_{12} = a_{34} = a_{45} = a_{61} = a\,,\ a_{23} = a_{56} = 0 \tag{6.2a}$$

$$\alpha_{12} = \alpha_{45} = -\frac{\pi}{4},\ \alpha_{23} = \alpha_{56} = \frac{\pi}{2},\ \alpha_{34} = \alpha_{61} = \frac{\pi}{4} \tag{6.2b}$$

$$d_i = 0\ \ (i = 1, 2, \ldots, 6) \tag{6.2c}$$

where a is the thickness of the panels.

Furthermore, the kinematic variable θ_i is defined to be the angle of rotation from x_i to x_{i+1} positively about z_i. A set of dihedral angles are also introduced along the revolute joints because they are more intuitive when describing the folding process of an origami structure. Let φ_i be the dihedral angle between adjacent panels with a common axis z_i. There are

$$\theta_1 = -\varphi_1,\ \theta_2 = \varphi_2,\ \theta_3 = -\varphi_3,\ \theta_4 = -\varphi_4,\ \theta_5 = \varphi_5,\ \theta_6 = \varphi_6 - \pi \tag{6.3}$$

The kinematic variables of a Bricard linkage satisfy the loop closure equation. The relationship of the dihedral angles of the panels around vertex A can be calculated as

$$\varphi_1 = \varphi_4,\ \varphi_2 = \varphi_3 = \varphi_5 = \varphi_6,\ \tan\frac{\varphi_2}{2} = \cos\frac{\pi}{4}\tan\frac{\varphi_1}{2} \tag{6.4}$$

Though bifurcations exist at the fully deployed configuration, a plane and line-symmetric Bricard linkage has only one DoF (You & Chen, 2011; Zhang & Chen, 2018). Note that vertices A, B, C and D in this origami pattern are identical. When one dihedral angle at vertex A is taken as an input, the rest of the dihedral angles between adjacent panels around vertex A can be uniquely determined. One of them is passed on as an input to vertex B, which determines all other dihedral angles around it. Subsequently, one of the angles gives an input to vertex D, and the rest of the dihedral angles around D is determined. Now consider vertex C. It shares one dihedral angle with that of vertices A, B and D, respectively, and thus, it has three inputs.

Since all these vertices are identical, three inputs are compatible, and they determine the remaining three dihedral angles around C.

Module I has only one DoF when it opens up from the folded stack. A physical model has been constructed with thick cardboard, and its deployment process from a compact volume to a flat surface is shown along a kinematic curve in Figure 6.7.

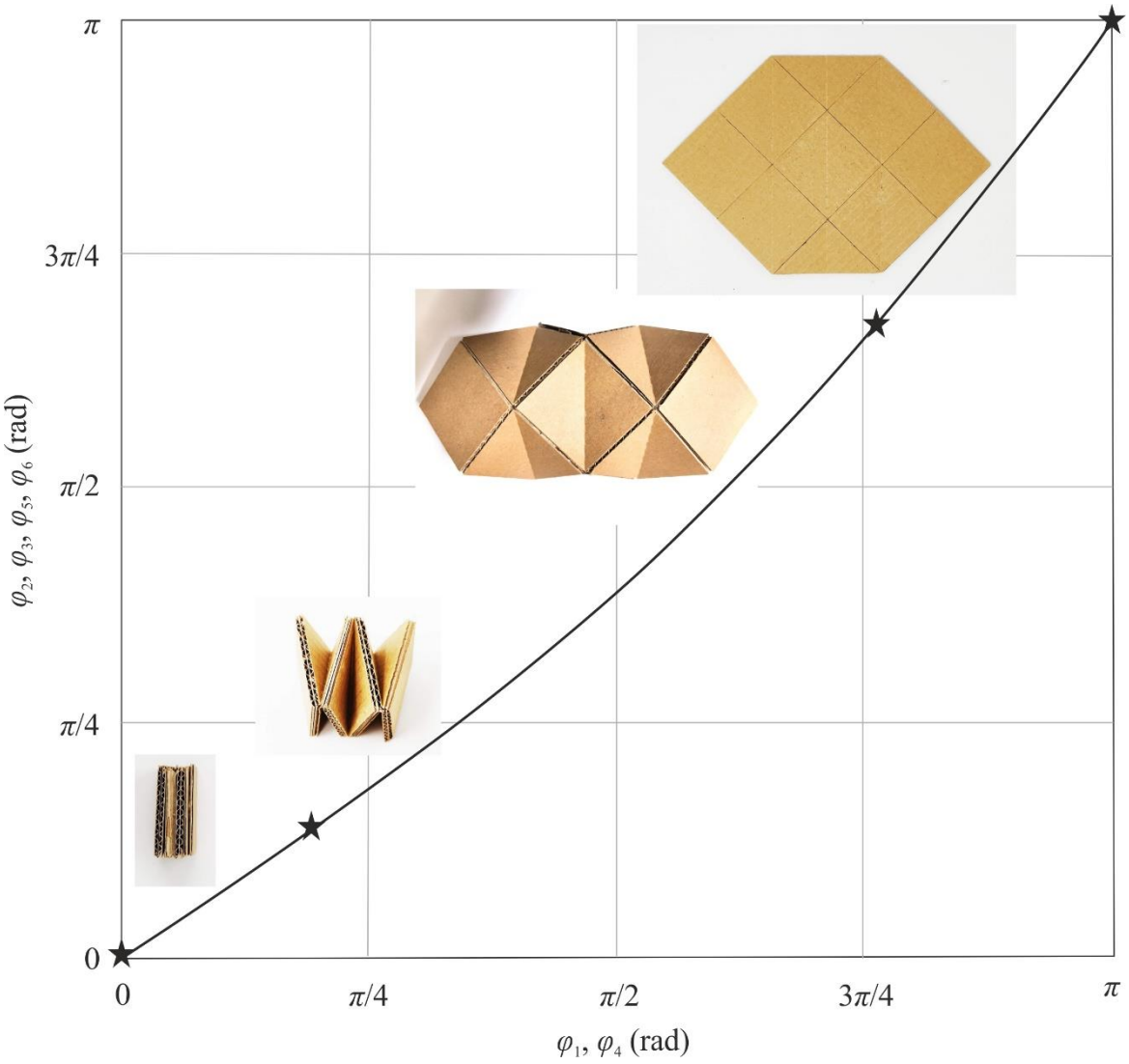

Figure 6.7 Deployment sequence of module I demonstrated by a thick cardboard model.

At its fully deployed configuration, bifurcations occur because the mountain creases around the vertices are aligned, and so are the valley creases. Apart from the motion as demonstrated in Figure 6.7, the model can be folded along any of the aligned creases. The surface of module I, consisting of four small triangles, ten larger ones, and two squares, packages into a stack with a square footprint, giving a deployment ratio of 8:1, which was previously defined in Chapter 5.

Several modules I can be combined to form larger arrays with a single DoF, as demonstrated by four examples in Figure 6.8. Two identical modules, one in light grey and one in red overlap each other such that the valley folds in the red unit coincide with the valley folds in the light grey one in Figure 6.8(a). So do the mountain folds. When the light grey unit is in motion, the overlapped region ensures that the dihedral angles are passed onto those in the red unit as inputs. The resultant assembly retains a single DoF and it can be folded compactly onto one square. In Figure 6.8(b)-(d), three arrays are formed when combining four modules I. Some panels are merged, as illustrated by the double arrows, where the relative rotations between the merged panels are unnecessary. Each array can be folded into a bundle without any voids.

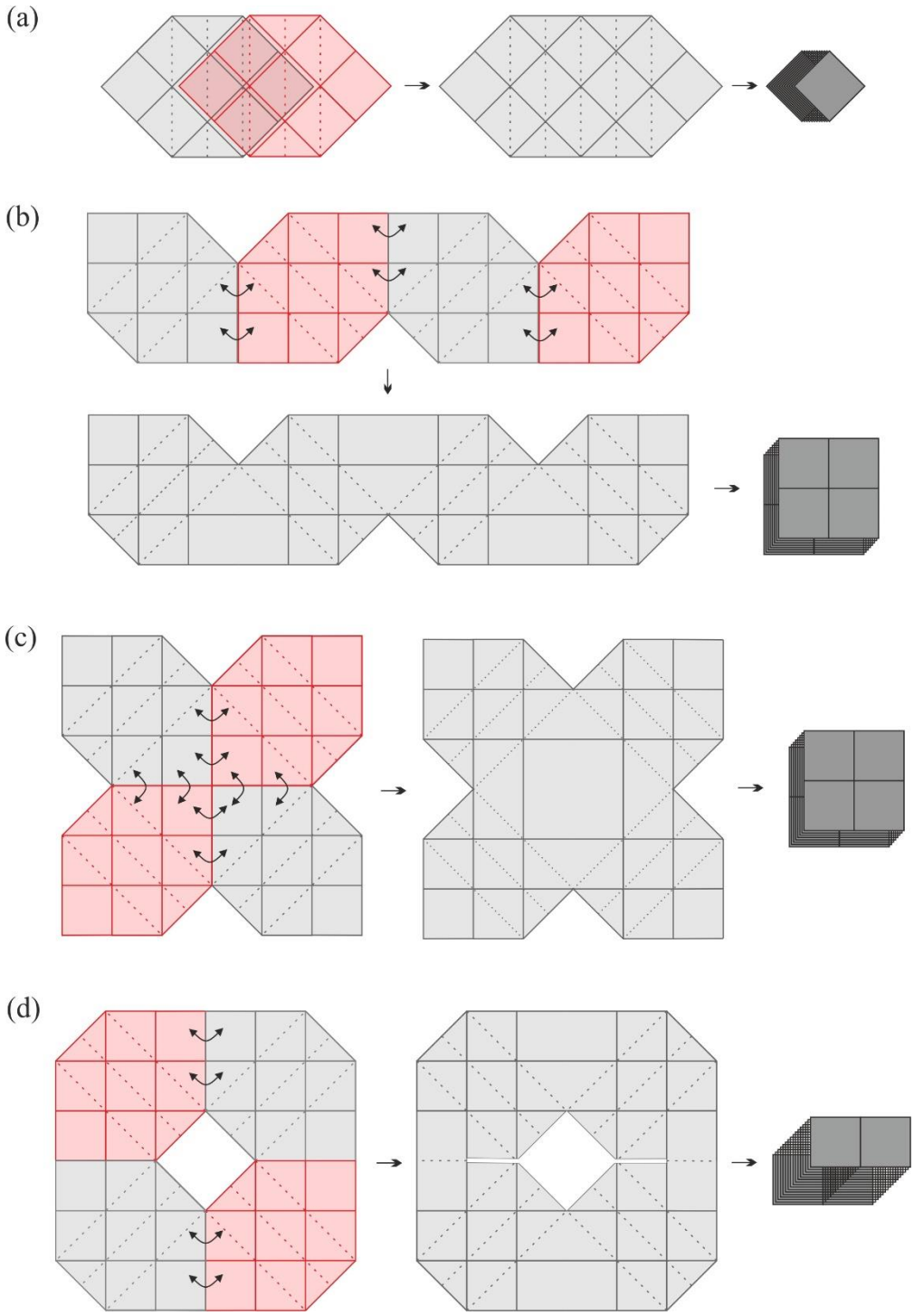

Figure 6.8 Combination of several modules I. (a) Two modules II are combined to fold onto one square. (b)-(c) Four modules I are combined to fold onto four squares. (d) Four modules I are combined to fold into two squares, with a void in the centre of the deployed array.

6.2.2 Module II and its tessellation

Module II can be obtained if arranging the four identical vertices A, B, C and D as shown in Figure 6.9(a). The crease pattern around vertex A in Module II is the same as that of vertex A in Module I, but inverted, in which the valley creases of A in Module I become the mountain creases of A in Module II, and vice versa. Therefore, its thick-panel counterpart is also a plane and line-symmetric Bricard linkage and its kinematics can be described by Eqn. (6.4).

The two pairs of horizontal valley creases are shared by vertices A and B, C and D, respectively, The panels on the two central columns are then merged due to symmetry as indicated by the double arrows in Figure 6.9(a). A slit is made in the middle of the array to facilitate the folding of the thick panels.

When the dihedral angle along crease a_1 is provided to the assembly as an input, as highlighted by the red arrow, the other angles around vertex A are set, among which, the dihedral angle along the crease a_5 is passed on to determine the dihedral angles at vertex B. Till now, the configuration of the upper half of module II is defined, marked by the blue arrows. Around the slit, revolute joints connect ten bodies into a closed loop. It can be regarded as a spatial linkage of ten links, which requires four inputs to be fully defined according to the Kutzbach criterion. The four dihedral angles along creases a_3, a_4, b_4, b_5 will then serve as inputs and thus, the configuration of panels around the slits can be determined. Likewise for the remaining array. Therefore, the configuration of module II is determined when one angle is given as input, indicating a single-DoF assembly. A flat surface can be folded into a compact volume without voids, as shown in Figure 6.9(b).

The folding sequence of module II is demonstrated via a thick card model in Figure 6.9(c). Although slits are made to facilitate the folding process, they are fully closed in the deployed state and the folded state. Similar to module I, bifurcations occur in the deployed state of

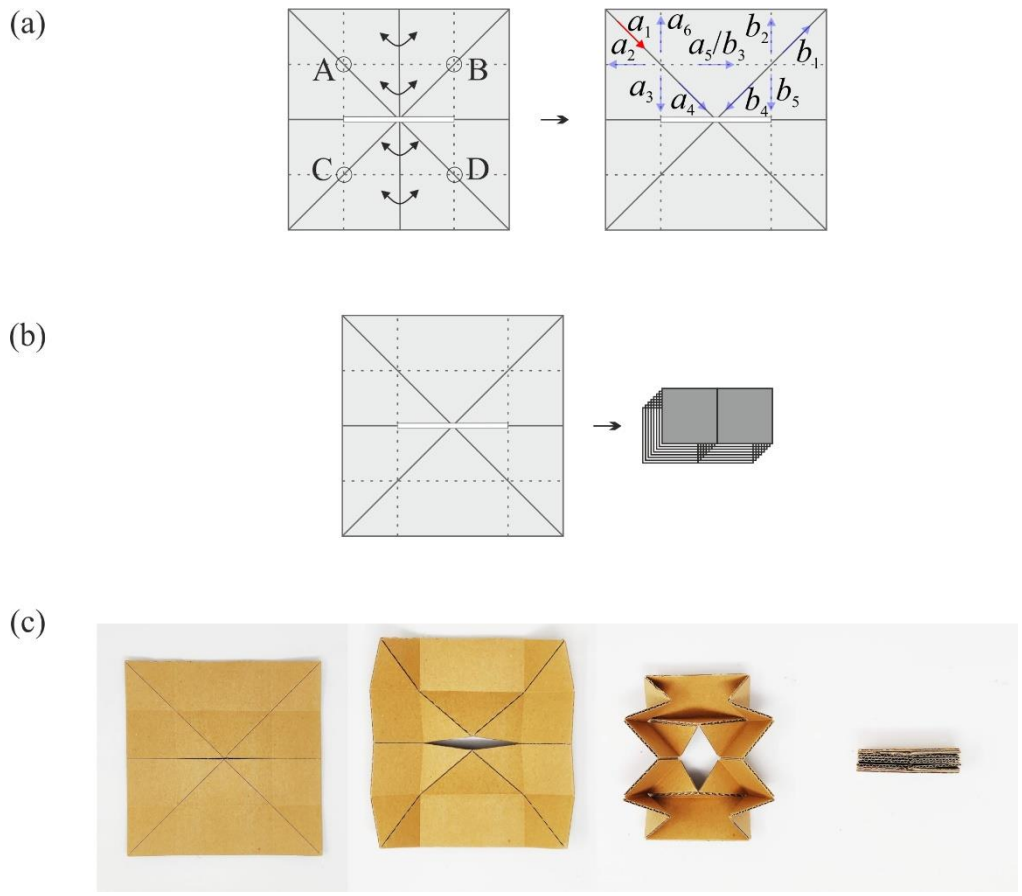

Figure 6.9 Crease pattern of module II and its folding sequence demonstrated by a prototype. (a) Formation of module II and its input-output relationship. (b) Crease pattern of module II and its folded configuration. (c) Folding sequence of module II that is made of thick cardboard.

module II as the mountain creases are aligned, and so are the valley creases. Furthermore, its deployment ratio is calculated to be 8:1 since a surface footprint of 16 squares in the deployed state is folded onto two squares.

Several modules II can be combined to form a larger array. One example is demonstrated in Figure 6.10(a), in which four modules II in grey are tessellated next to each other. They are combined through another module II that is embedded in the array, as highlighted in red. It shares six panels and six revolute joints with each module II in grey, as shown by the overlapping region, resulting in a synchronised single-DoF motion. The folding sequence of the array made of thick cardboard is demonstrated in Figure 6.10(b). All the slits are closed in the deployed state. A flat and continuous surface is folded to a compact volume. Due to the

(a)

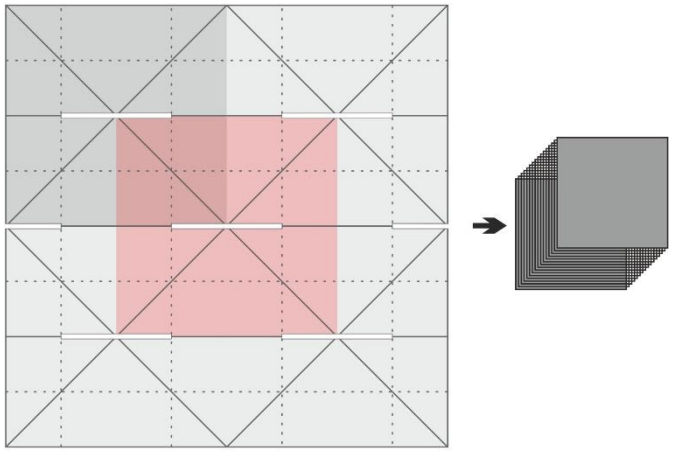

(b)

Figure 6.10 A larger array forms from combining several modules II. (a) A flat surface can be folded into a compact volume. (b) A thick card model demonstrates the folding sequence.

contractive motion of panels, the array can only be enlarged by increasing more rows, whereas adding more modules II column-wise will result in physical interference of panels.

6.2.3 Module III and its tessellation

Figure 6.11(a) shows the formation of Module III, where four identical vertices A, B, C and D are arranged such that not only the horizontal and vertical creases are shared, but the diagonal crease is also shared by vertices B and C. Again, the thick-panel counterpart of these vertices can be modelled by a plane and line-symmetric Bricard linkage. Therefore, their motion follows the kinematic relationship obtained in Eqn. (6.4).

When the dihedral angle along crease a_1 is provided to module III as an input, as highlighted by the red arrow, the other angles around vertex A are fixed, passing the ones along creases a_6 and a_5 to vertices B and C, respectively. After that, the dihedral angles at vertices B and C are defined and input to determine the configuration of panels at vertex D. Since vertices A, B, C and D in this origami pattern are identical, the two inputs are compatible, and they determine the remaining four dihedral angles around D, resulting in a single-DoF assembly. Again, we can observe that the mountain and the valley creases are aligned at the fully deployed state in Figure 6.11(b), resulting in bifurcations. A deployed surface area of 16 squares is folded onto four squares, giving module III a deployment ratio of 4:1.

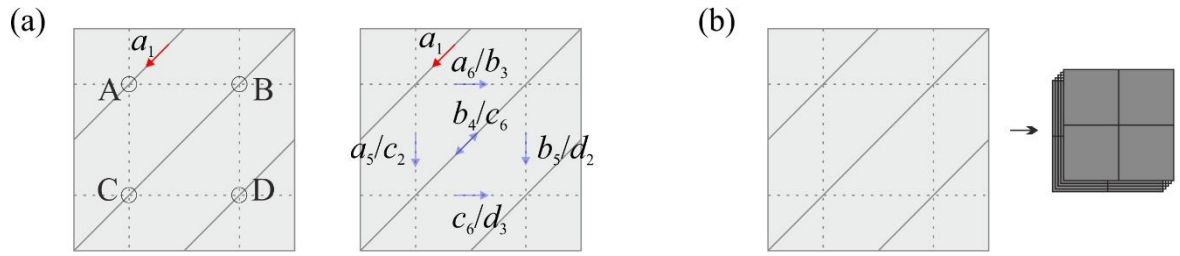

Figure 6.11 Crease pattern of module III. (a) Input-output angle relationship. (b) A flat surface is folded into a compact volume.

A larger array can be tessellated by combining several modules III. An example is shown in Figure 6.12(a), where two modules III, one in grey and one in red are connected by overlapping some panels and creases. It can also be folded onto an area of four squares. A thick cardboard model was made to demonstrate its folding process in Figure 6.12(b), in which a spiral motion can be observed. A flat and continuous surface is folded into a compact volume, but a stepped surface is obtained in the folded package. Besides, though more modules III can be connected to tessellate a larger surface area along the horizontal direction, no more panels can be added to the array along the vertical direction due to physical interference.

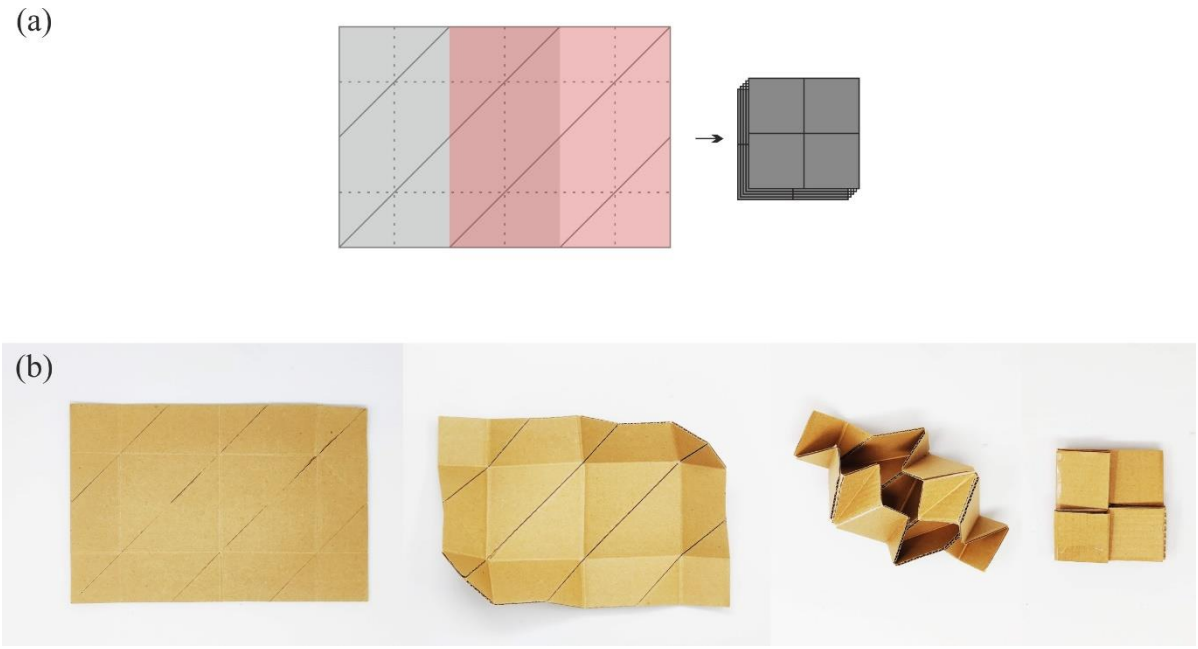

Figure 6.12 A larger array forms from combining two modules III. (a) A flat surface can be folded into a compact volume. (b) A thick card model demonstrates the folding sequence.

6.3 Conclusion

Via modular designs, flat surfaces of squares or the combination of squares and half-square triangles are folded into compact stacks that are conforming to the shape of a cuboid. However, doing so usually increases the number of DoFs. Besides, kinematic bifurcations are identified in the fully deployed configuration due to the orthogonality of the axes of the revolute joints. Nevertheless, the modular designs provide engineers with more options to form a large flat array with a small number of DoFs.

CHAPTER 7

FINAL REMARKS

This thesis is concerned with folding an array of rigid panels with uniform thickness into a compact volume without voids. Panels are connected only by the simple and robust revolute joints on either their top or bottom facet. Slits can be made in some arrays to facilitate the folding of the thick panels, but they are fully closed in the deployed state, forming a completely flat and continuous surface. Four main achievements are summarised in this chapter, followed by an attempt to identify future work.

7.1 Summary of achievements

7.1.1 Fold a flat surface of thick panels into a compact volume

All existing solutions to deployable thick-panel structures contain one or more major disadvantages. First, the thickness of each panel has to be adjusted to enable folding possibly kinematically, resulting in uneven surfaces in the fully deployed state. Secondly, voids appear in the folded state, indicating a lack of compactness in the packaged bundle.

Chapter 3 attempted to fold an array of identical rigid panels with uniform thickness into two compact stacks via the Hamiltonian circuit (HC) approach. By placing revolute joints on the

top and bottom facets of the thick panels consecutively according to an HC that was plotted within the array, a chessboard-like array turned into a closed loop of rigid panels. Furthermore, more than one HC could usually be found within a given array of regular polygons. Therefore, a method was proposed based on the reflection of vectors to judge if the given loop of panels could be folded into two stacks in parity. Finally, the approach was validated through folding experiments of the thick-panel prototypes.

7.1.2 Deploying a multi-DoF array with elastic hinges

Using the folding scheme devised in Chapter 3, the resulting array possesses multiple DoFs, which are inevitable when the number of panels is large, despite that it is possible to reduce the number of DoFs if inactive revolute joints are replaced by rigid joints along the plane of symmetry of the array. Therefore, spring-loaded hinges are employed to synchronise its deployment process.

In Chapter 4, an optimisation method was proposed to select the stiffness of the rotational hinges to ensure a collision-free deployment. Multi-body dynamic simulation of deployment and a collision detection method were incorporated into the optimisation process. The sequenced deployment trajectories of panels ensure no collisions occur during deployment, and the array always deploys to a flat surface from packaged stacks. Based on the optimised spring stiffnesses at various hinge locations, a physical prototype was constructed. The collision-free deployments were captured by a high-speed camera and they were benchmarked against the simulated results.

7.1.3 Single-DoF arrays of isosceles triangular panels

Chapter 5 unveiled a solution to compactly fold arrays composed of two types of panels with uniform thickness into stacks without any voids. First, a closed-loop chain was formed by connecting ten isosceles triangular panels by simple revolute joints on either top or bottom of panels according to the HC approach. After replacing the inactive revolute joints with rigid joints on the top and bottom layers of the stacks, a small deployable array consisting of eight bodies was formed, referred to as an 8R closed-chain element. Although an 8R closed chain would have two DoFs in general, single-DoF units were created by linking four 8R elements in particular topologies. After that, a parametric study was carried out to provide precise design ranges that prevent the panels from physical interference when the deployable array was in motion. Finally, tessellations of the units are presented to form larger flat arrays where single-DoF deployment and compact packaging properties were intact. The proposed designs were validated by folding thick-panel prototypes.

The bi-directional folding concept can be extended to fold assembly consisting of an infinite number of isosceles triangular panels. Besides, this work is also important in the theory of mechanisms. The units are rare examples where a kinematic loop consisting of linkages of multiple DoFs ends up with single mobility.

7.1.4 CubeSat-conforming arrays with less-DoFs

In Chapter 3, the HC approach results in arrays with multiple DoFs, which is not preferred for space applications, whereas the approach in Chapter 5 leads to arrays of single DoF but the folded bundles do not conform to the shape of a CubeSat. In Chapter 6, arrays are formed using squares or the combination of squares and half-square triangles via modular designs. The

modules can be combined to form a larger surface with a small number of DoFs and be folded into a compact cuboid.

7.2 Future work

This thesis has established preliminary findings to fold a flat surface of uniform thickness into a compact volume via the HC approach and its subsequent collision-free deployment if it has multiple DoFs. It opens up a multitude of research opportunities for future developments.

The first area of research lies in searching the useful HC to obtain a two-stack foldable configuration for any loops of regular polygons. In the array of 12 regular hexagons, creases are placed according to an HC that is plotted within the array. A crease satisfies the two-stack foldable criterion through the reflection operations. However, a twist of 2π formed and could not be resolved when we tried to fold a thin card model. Determining how the twist is formed and how to detect the twist from a planar connectivity graph of the polygons is still an open problem.

The second area of research emerges from the limitations in the current studies when employing spring-loaded hinges to deploy a multi-DoF array. The stiffness of the torsional springs may be quadratic instead of linear by nature, with a higher stiffness when the angle of rotation is larger and a lower stiffness when it is smaller. To overcome the limitation, the simulation model can be refined by using the exact moment-angle relations. Torsional springs with non-zero torque at the fully deployed configuration can be adopted in future designs to resist any unexpected impacts after being deployed. Besides, compliant hinges that are responsive to external stimuli can replace the torsional spring-loaded hinges to deploy the compact package.

Apart from the spring stiffness, the damping coefficient at each hinge is another important parameter that could affect the deployment process. However, there was no damping control in the current prototype, which explained the small discrepancies between the simulated and experimental results. This problem can be overcome by either conducting more precise measurements or incorporating suitable damping control within the spring-loaded hinges. For instance, packing lubricants with different viscosities can be applied within the rotational hinges to provide the required damping coefficients.

Another aspect of future work comes from the single-DoF mobile assembly of 8R elements. Symmetrical 8R elements that were formed out of isosceles triangles were combined into a mobile network to provide a single-DoF motion. Other combinations may also be possible, for instance, a network of asymmetrical 8R elements constructed out of other geometries. It would be interesting to study this type of unusual mechanism where a kinematic loop consisting of linkages of multiple DoFs ends up with a single DoF.

Appendix

A detailed numerical approach for kinematic analysis of unit II that is presented in Chapter 5 is conducted here.

Numerical Approach for Kinematic analysis of Unit II

Numerical analysis of assemblies forming closed loops can be done using a predictor-corrector approach (Gan & Pellegrino, 2006; Li, 2020). It consists of two steps. The first is to find all possible infinitesimal motions using a predictor step. This is followed by a correction step to acquire finite motions.

A1. Predictor Step

At step *s*, a set of geometrically compatible kinematic variables $\boldsymbol{\theta}_s = [\theta_{1s}, \theta_{2s}, ..., \theta_{8s}]^{\mathrm{T}}$ is obtained. They satisfied the loop closure equation

$$\mathbf{T}_{21\_s} \cdot \mathbf{T}_{32\_s} \cdot ... \cdot \mathbf{T}_{87\_s} \cdot \mathbf{T}_{18\_s} = \mathbf{I}_{4\times4} \tag{A1}$$

obtained by rearranging Eqn. (5.6) in the main context. At step *s* + 1, a new set of kinematic variables should also satisfy Eqn. (A1), i.e.,

$$\mathbf{T}_{21\_(s+1)} \cdot \mathbf{T}_{32\_(s+1)} \cdot \ldots \cdot \mathbf{T}_{87\_(s+1)} \cdot \mathbf{T}_{18\_(s+1)} = \mathbf{I}_{4\times4} \tag{A2}$$

With small-angle increments, the Taylor expansion is applied to each angle, and terms containing higher-order of increments were neglected, e.g.,

$$\sin(\theta_{1s} + \Delta\theta_1) \approx \sin\theta_{1s} + \cos\theta_{1s}\Delta\theta_1,\ \cos(\theta_{1s} + \Delta\theta_1) \approx \cos\theta_{1s} - \sin\theta_{1s}\Delta\theta_1. \tag{A3}$$

Hence, all transformation matrices at step $s + 1$, given by Eqn. (5.5) in the main text, can be simplified. For instance, for $\mathbf{T}_{21\_(s+1)}$, we have

$$\begin{aligned}\mathbf{T}_{21\_(s+1)} &= \begin{bmatrix} \cos(\theta_{1s} + \Delta\theta_1) & -\cos\alpha_{12}\sin(\theta_{1s} + \Delta\theta_1) & \sin\alpha_{12}\sin(\theta_{1s} + \Delta\theta_1) & a_1\cos(\theta_{1s} + \Delta\theta_1) \\ \sin(\theta_{1s} + \Delta\theta_1) & \cos\alpha_{12}\cos(\theta_{1s} + \Delta\theta_1) & -\sin\alpha_{12}\cos(\theta_{1s} + \Delta\theta_1) & a_1\sin(\theta_{1s} + \Delta\theta_1) \\ 0 & \sin\alpha_{12} & \cos\alpha_{12} & d_1 \\ 0 & 0 & 0 & 1 \end{bmatrix} \\ &\approx \mathbf{T}_{21\_s} + \mathbf{T}'_{21\_s}\Delta\theta_1\end{aligned} \tag{A4}$$

where $\mathbf{T}'_{21\_s}$ is the derivative of $\mathbf{T}_{21}$ with respect to θ_1. Likewise, we obtain the other transformation matrices $\mathbf{T}_{32\_(s+1)}$, $\mathbf{T}_{43\_(s+1)}$, etc.

Substituting these transformation matrices at step $s + 1$ into Eqn. (A2) gives

$$(\mathbf{T}_{21\_s} + \mathbf{T}'_{21\_s}\Delta\theta_1)(\mathbf{T}_{32\_s} + \mathbf{T}'_{32\_s}\Delta\theta_2)\ldots(\mathbf{T}_{18\_s} + \mathbf{T}'_{18\_s}\Delta\theta_8) = \mathbf{I}_{4\times4} \tag{A5}$$

Expanding Eqn. (A5) and rearranging it led to

$$\begin{aligned} &\mathbf{T}_{21\_s}\mathbf{T}_{32\_s}\ldots\mathbf{T}_{87\_s}\mathbf{T}_{18\_s} + \\ &(\mathbf{T}'_{21\_s}\mathbf{T}_{32\_s}\ldots\mathbf{T}_{87\_s}\mathbf{T}_{18\_s})\Delta\theta_1 + \\ &(\mathbf{T}_{21\_s}\mathbf{T}'_{32\_s}\ldots\mathbf{T}_{87\_s}\mathbf{T}_{18\_s})\Delta\theta_2 + \\ &\qquad\qquad\vdots \qquad\qquad + \\ &(\mathbf{T}_{21\_s}\mathbf{T}_{32\_s}\ldots\mathbf{T}_{87\_s}\mathbf{T}'_{18\_s})\Delta\theta_8 = \mathbf{I}_{4\times4} \end{aligned} \tag{A6}$$

Note that the first term in Eqn. (A6) equals $\mathbf{I}_{4\times4}$ according to Eqn. (A1). Therefore, Eqn. (A6) becomes

$$\mathbf{C}_1\Delta\theta_1 + \mathbf{C}_2\Delta\theta_2 + ... + \mathbf{C}_8\Delta\theta_8 = \mathbf{0}_{4\times4} \tag{A7}$$

where the constant matrices $\mathbf{C}_1 = \mathbf{T}_{21\_s}^{'}\mathbf{T}_{32\_s}...\mathbf{T}_{87\_s}\mathbf{T}_{18\_s}$, $\mathbf{C}_2 = \mathbf{T}_{21\_s}\mathbf{T}_{32\_s}^{'}...\mathbf{T}_{87\_s}\mathbf{T}_{18\_s}$, etc. It is interesting to note that in our case, the elements in the last row of the constant matrices $\mathbf{C}_1$, $\mathbf{C}_2$,…, $\mathbf{C}_8$ has elements with null value. Hence, Eqn. (A7) is effectively twelve simultaneous linear equations, and thus, Eqn. (A7) can be written more compactly as

$$\mathbf{M}_{12\times8}\Delta\boldsymbol{\theta}_{8\times1} = \mathbf{0}_{12\times1} \tag{A8}$$

where $\Delta\boldsymbol{\theta}_{8\times1} = \left[\Delta\theta_1,\ \Delta\theta_2,\ ...,\ \Delta\theta_8\right]^{\mathrm{T}}$, and

$$\mathbf{M}_{12\times8} = \begin{bmatrix} a_1 & a_2 & \cdots & a_8 \\ b_1 & b_2 & \cdots & b_8 \\ \vdots & \vdots & \ddots & \vdots \\ l_1 & l_2 & \cdots & l_8 \end{bmatrix} \tag{A9}$$

$\mathbf{M}_{12\times8}$ is a collection of known coefficients, which is also known as the Jacobian matrix of the 8R element.

After acquiring the Jacobian matrix for one 8R element, we can obtain a global Jacobian matrix for unit II, in which four 8R elements, *A*, *F*, *G*, *H* are interconnected, as shown in Figure 5.6(d) in the main text. Eqn. (A8) is extended to

$$\mathbf{M}^{II}\Delta\boldsymbol{\theta}^{II} = \begin{bmatrix} \mathbf{M}_A \\ \mathbf{M}_H \\ \mathbf{M}_F \\ \mathbf{M}_G \end{bmatrix}\Delta\boldsymbol{\theta}^{II} = \mathbf{0} \tag{A10}$$

where $\Delta\boldsymbol{\theta}^{II} = [\Delta\theta_1, \Delta\theta_2, ..., \Delta\theta_{24}]^{\mathrm{T}}$, is a vector with 24 entries because eight revolute joints merge when four 8R elements form unit II, leaving the 24 joints as labelled in Figure A1. $\mathbf{M}_A$ is

$$\mathbf{M}_A = \begin{bmatrix} a_{A1} & a_{A2} & \cdots & a_{A8} & 0 & \cdots & 0 \\ b_{A1} & b_{A2} & \cdots & b_{A8} & 0 & & 0 \\ \vdots & \vdots & \ddots & \vdots & \vdots & \ddots & \vdots \\ l_{A1} & l_{A2} & \cdots & l_{A8} & 0 & \cdots & 0 \end{bmatrix}_{12\times 24} \tag{A11}$$

obtained by expanding $\mathbf{M}_{12\times 8}$ for 8R element *A*. Likewise for $\mathbf{M}_H$, $\mathbf{M}_F$, and $\mathbf{M}_G$.

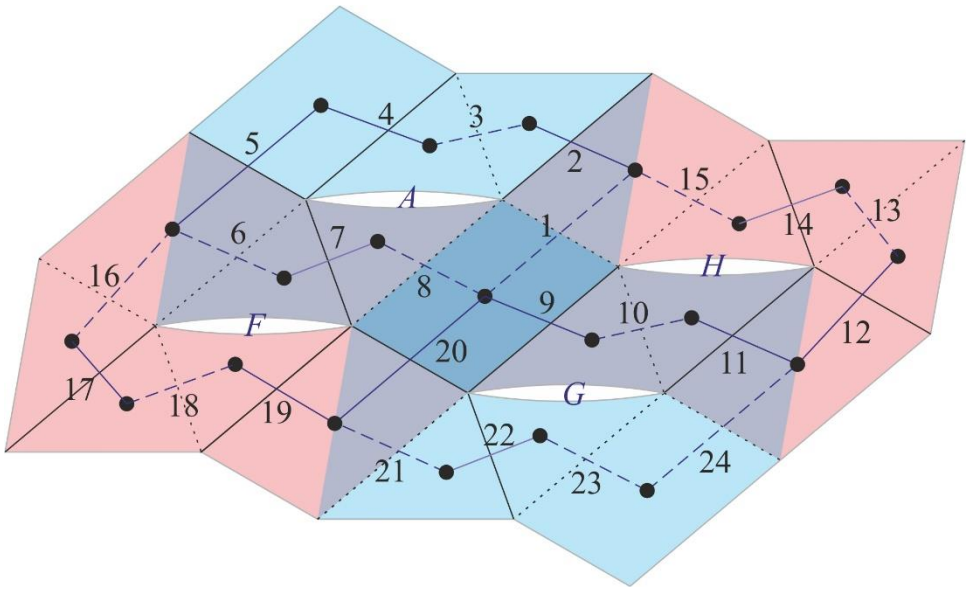

Figure A1. Unit II where all joints are numbered to facilitate numerical simulation.

Note that, when two revolute joints in their corresponding 8R elements shared one joint in unit II, e.g., a_1 and h_1, they merge into one joint, and the corresponding coefficients in these two elements are placed in one column. Hence, $\mathbf{M}^{II}$, the Jacobian matrix of unit II, has a dimension of 48×24, which is

$$\mathbf{M}^{II} = \begin{bmatrix}
a_{a1} & a_{a2} & ... & a_{a6} & a_{a7} & a_{a8} & 0 & & & & \cdots & & & & & & 0 \\
b_{a1} & b_{a2} & ... & b_{a6} & b_{a7} & b_{a8} & 0 & & & & \cdots & & & & & & 0 \\
\vdots & \vdots & \ddots & \vdots & \vdots & \vdots & \vdots & & & & \ddots & & & & & & \vdots \\
l_{a1} & l_{a2} & ... & l_{a6} & l_{a7} & l_{a8} & 0 & & & & \cdots & & & & & & 0 \\
a_{h1} & 0 & \cdots & 0 & 0 & 0 & a_{h2} & a_{h3} & a_{h4} & ... & a_{h8} & 0 & & & & \cdots & & & 0 \\
b_{h1} & 0 & \cdots & 0 & 0 & 0 & b_{h2} & a_{h3} & a_{h4} & ... & a_{h8} & 0 & & & & & & & \\
\vdots & \vdots & \ddots & \vdots & \vdots & \vdots & \vdots & \vdots & \vdots & \vdots & \vdots & \vdots & & & & \ddots & & & \vdots \\
l_{h1} & 0 & \cdots & 0 & 0 & 0 & l_{h2} & l_{h3} & l_{h4} & ... & l_{h8} & 0 & & & & \cdots & & & 0 \\
0 & ... & 0 & a_{f8} & a_{f7} & a_{f6} & 0 & & ... & & 0 & a_{f1} & a_{f2} & ... & a_{f5} & 0 & & \cdots & 0 \\
0 & & & b_{f8} & b_{f7} & b_{f6} & & & & & & b_{f1} & b_{f2} & & b_{f5} & & & & \\
\vdots & \ddots & \vdots & \vdots & \vdots & \vdots & \vdots & & \ddots & & \vdots & \vdots & \vdots & \ddots & \vdots & \vdots & & \ddots & \vdots \\
0 & ... & 0 & l_{f8} & l_{f7} & l_{f6} & 0 & & ... & & 0 & l_{f1} & l_{f2} & ... & l_{f5} & 0 & & \cdots & 0 \\
0 & & & ... & & 0 & a_{g4} & a_{g3} & a_{g2} & 0 & & ... & & 0 & a_{g5} & a_{g6} & a_{g7} & a_{g8} & a_{g1} \\
 & & & & & & b_{g4} & b_{g3} & b_{g2} & 0 & & & & 0 & b_{g5} & b_{g6} & b_{g7} & b_{g8} & b_{g1} \\
\vdots & & & \ddots & & \vdots & & & \vdots & \vdots & & \ddots & & \vdots & \vdots & \vdots & \vdots & \vdots & \vdots \\
0 & & & ... & & 0 & l_{g4} & l_{g3} & l_{g2} & 0 & & ... & & 0 & l_{g5} & l_{g6} & l_{g7} & l_{g8} & l_{g1}
\end{bmatrix} \tag{A12}$$

The SVD of the Jacobian matrix was obtained as

$$\mathbf{M}^{II}{}_{48\times24} = \mathbf{U}_{48\times48}\mathbf{V}_{48\times24}\mathbf{W}^{\mathrm{T}}_{24\times24}\,. \tag{A13}$$

$\mathbf{U} = [\mathbf{u}_1, \mathbf{u}_2, \ldots, \mathbf{u}_{48}]$ and $\mathbf{W} = [\mathbf{w}_1, \mathbf{w}_2, \ldots, \mathbf{w}_{24}]$ are the collections of left and right singular vectors, respectively, that were orthonormal to each other; $\mathbf{V}$ is a rectangular matrix containing r singular values on its diagonal where r was the rank of matrix $\mathbf{M}^{II}$. The last $24 - r$ columns of matrix $\mathbf{W}$ give the strain-free infinitesimal motions from steps s.

A2. Corrector Step

The predictor step does not include higher-order terms. Therefore, for an assembly to have finite motion, a corrector step is needed in order to find a configuration $\boldsymbol{\theta}^{II}_{s+1}$ based on $\bar{\boldsymbol{\theta}}^{II}$ without deforming the panels. Details of this step can be found in (Gan & Pellegrino, 2006). Completion of this step yields $\boldsymbol{\theta}^{II}_{s+1}$.

Using this predictor-corrector scheme, the motion path of unit II can be plotted by calculating incremental solutions of the loop closure equations while imposing global constraints that connected four 8R elements.

A3. Application to Unit II

We consider unit II with the following geometric properties.

$$a = 10,\ d = 43.86,\ \alpha = 7\pi/18 \tag{A14}$$

We start the predictor-corrector approach from the fully folded configuration, i.e.,

$$\boldsymbol{\theta}_0 = [\pi,\ 0, 0, 0,\ -\pi,\ 0, 0, 0]^{\mathrm{T}} \tag{A15}$$

The global Jacobian matrix $\mathbf{M}^{II}$ was constructed according to Eqn. (A1) – (A12). The joints are numbered as shown in Figure A1.

$$\mathbf{M}^{II} = \begin{bmatrix}
0 & 0 & 0 & 0 & 0 & 0 & 0 & 0 & 0 & 0 & 0 & 0 & 0 & 0 & 0 & 0 & 0 & 0 & 0 & 0 & 0 & 0 & 0 & 0 \\
-1 & -0.342 & -1 & -0.342 & 1.000 & 0.342 & 1.000 & 0.342 & 0 & 0 & 0 & 0 & 0 & 0 & 0 & 0 & 0 & 0 & 0 & 0 & 0 & 0 & 0 & 0 \\
0 & -0.940 & 0 & 0.940 & 0 & 0.934 & 0 & -0.940 & 0 & 0 & 0 & 0 & 0 & 0 & 0 & 0 & 0 & 0 & 0 & 0 & 0 & 0 & 0 & 0 \\
0 & 0 & 0 & -28.191 & 41.212 & 0 & 41.212 & 0 & 0 & 0 & 0 & 0 & 0 & 0 & 0 & 0 & 0 & 0 & 0 & 0 & 0 & 0 & 0 & 0 \\
1 & 0.342 & 1 & 0.342 & -1.000 & -0.342 & -1.0000 & -0.342 & 0 & 0 & 0 & 0 & 0 & 0 & 0 & 0 & 0 & 0 & 0 & 0 & 0 & 0 & 0 & 0 \\
0 & 0 & 0 & 0 & 0 & 0 & 0 & 0 & 0 & 0 & 0 & 0 & 0 & 0 & 0 & 0 & 0 & 0 & 0 & 0 & 0 & 0 & 0 & 0 \\
0 & 0 & 0 & 0 & 0 & 0 & 0 & 0 & 0 & 0 & 0 & 0 & 0 & 0 & 0 & 0 & 0 & 0 & 0 & 0 & 0 & 0 & 0 & 0 \\
0 & 3.420 & 20 & 10.261 & -30.000 & -6.840 & -10.000 & 0 & 0 & 0 & 0 & 0 & 0 & 0 & 0 & 0 & 0 & 0 & 0 & 0 & 0 & 0 & 0 & 0 \\
0 & 0.940 & 0 & -0.940 & 0 & -0.934 & 0 & 0.940 & 0 & 0 & 0 & 0 & 0 & 0 & 0 & 0 & 0 & 0 & 0 & 0 & 0 & 0 & 0 & 0 \\
0 & 0 & 0 & 0 & 0 & 0 & 0 & 0 & 0 & 0 & 0 & 0 & 0 & 0 & 0 & 0 & 0 & 0 & 0 & 0 & 0 & 0 & 0 & 0 \\
0 & 0 & 0 & 0 & 0 & 0 & 0 & 0 & 0 & 0 & 0 & 0 & 0 & 0 & 0 & 0 & 0 & 0 & 0 & 0 & 0 & 0 & 0 & 0 \\
0 & 9.397 & 0 & -28.191 & 0 & -18.794 & 0 & 0 & 0 & 0 & 0 & 0 & 0 & 0 & 0 & 0 & 0 & 0 & 0 & 0 & 0 & 0 & 0 & 0 \\
0 & 0 & 0 & 0 & 0 & 0 & 0 & 0 & 0 & 0 & 0 & 0 & 0 & 0 & 0 & 0 & 0 & 0 & 0 & 0 & 0 & 0 & 0 & 0 \\
-1 & 0 & 0 & 0 & 0 & 0 & 0 & 0 & -0.342 & -1 & -0.342 & 1.000 & 0.342 & 1.000 & 0.342 & 0 & 0 & 0 & 0 & 0 & 0 & 0 & 0 & 0 \\
0 & 0 & 0 & 0 & 0 & 0 & 0 & 0 & -0.940 & 0 & 0.940 & 0 & 0.940 & 0 & -0.940 & 0 & 0 & 0 & 0 & 0 & 0 & 0 & 0 & 0 \\
0 & 0 & 0 & 0 & 0 & 0 & 0 & 0 & 0 & 0 & -28.191 & 41.212 & 0 & 41.212 & 0 & 0 & 0 & 0 & 0 & 0 & 0 & 0 & 0 & 0 \\
1 & 0 & 0 & 0 & 0 & 0 & 0 & 0 & 0.342 & 1 & 0.342 & -1.000 & -0.342 & -1.000 & -0.342 & 0 & 0 & 0 & 0 & 0 & 0 & 0 & 0 & 0 \\
0 & 0 & 0 & 0 & 0 & 0 & 0 & 0 & 0 & 0 & 0 & 0 & 0 & 0 & 0 & 0 & 0 & 0 & 0 & 0 & 0 & 0 & 0 & 0 \\
0 & 0 & 0 & 0 & 0 & 0 & 0 & 0 & 0 & 0 & 0 & 0 & 0 & 0 & 0 & 0 & 0 & 0 & 0 & 0 & 0 & 0 & 0 & 0 \\
0 & 0 & 0 & 0 & 0 & 0 & 0 & 0 & 3.420 & 20 & 10.261 & -30.000 & -6.840 & -10.000 & 0 & 0 & 0 & 0 & 0 & 0 & 0 & 0 & 0 & 0 \\
0 & 0 & 0 & 0 & 0 & 0 & 0 & 0 & 0.940 & 0 & -0.9340 & 0 & -0.940 & 0 & 0.940 & 0 & 0 & 0 & 0 & 0 & 0 & 0 & 0 & 0 \\
0 & 0 & 0 & 0 & 0 & 0 & 0 & 0 & 0 & 0 & 0 & 0 & 0 & 0 & 0 & 0 & 0 & 0 & 0 & 0 & 0 & 0 & 0 & 0 \\
0 & 0 & 0 & 0 & 0 & 0 & 0 & 0 & 0 & 0 & 0 & 0 & 0 & 0 & 0 & 0 & 0 & 0 & 0 & 0 & 0 & 0 & 0 & 0 \\
0 & 0 & 0 & 0 & 0 & 0 & 0 & 0 & 9.397 & 0 & -28.191 & 0 & -18.794 & 0 & 0 & 0 & 0 & 0 & 0 & 0 & 0 & 0 & 0 & 0 \\
0 & 0 & 0 & 0 & 0 & 0 & 0 & 0 & 0 & 0 & 0 & 0 & 0 & 0 & 0 & 0 & 0 & 0 & 0 & 0 & 0 & 0 & 0 & 0 \\
0 & 0 & 0 & 0 & 0 & 0.342 & 1.000 & 0.342 & 0 & 0 & 0 & 0 & 0 & 0 & 0 & 1.000 & -0.342 & -1 & -0.342 & -1 & 0 & 0 & 0 & 0 & 0 \\
0 & 0 & 0 & 0 & 0 & -0.940 & 0 & 0.940 & 0 & 0 & 0 & 0 & 0 & 0 & 0 & 0 & 0.940 & 0 & -0.940 & 0 & 0 & 0 & 0 & 0 & 0 \\
0 & 0 & 0 & 0 & 0 & 0 & 41.212 & 0 & 0 & 0 & 0 & 0 & 0 & 0 & 0 & 41.212 & -28.191 & 0 & 0 & 0 & 0 & 0 & 0 & 0 & 0 \\
0 & 0 & 0 & 0 & 0 & -0.342 & -1.000 & -0.342 & 0 & 0 & 0 & 0 & 0 & 0 & 0 & -1.000 & 0.342 & 1 & 0.342 & 1 & 0 & 0 & 0 & 0 & 0 \\
0 & 0 & 0 & 0 & 0 & 0 & 0 & 0 & 0 & 0 & 0 & 0 & 0 & 0 & 0 & 0 & 0 & 0 & 0 & 0 & 0 & 0 & 0 & 0 \\
0 & 0 & 0 & 0 & 0 & 0 & 0 & 0 & 0 & 0 & 0 & 0 & 0 & 0 & 0 & 0 & 0 & 0 & 0 & 0 & 0 & 0 & 0 & 0 \\
0 & 0 & 0 & 0 & 0 & 0 & -10.000 & -6.840 & 0 & 0 & 0 & 0 & 0 & 0 & 0 & -30.000 & 10.261 & 20 & 3.420 & 0 & 0 & 0 & 0 & 0 & 0 \\
0 & 0 & 0 & 0 & 0 & 0.940 & 0 & -0.940 & 0 & 0 & 0 & 0 & 0 & 0 & 0 & 0 & -0.940 & 0 & 0.940 & 0 & 0 & 0 & 0 & 0 & 0 \\
0 & 0 & 0 & 0 & 0 & 0 & 0 & 0 & 0 & 0 & 0 & 0 & 0 & 0 & 0 & 0 & 0 & 0 & 0 & 0 & 0 & 0 & 0 & 0 \\
0 & 0 & 0 & 0 & 0 & 0 & 0 & 0 & 0 & 0 & 0 & 0 & 0 & 0 & 0 & 0 & 0 & 0 & 0 & 0 & 0 & 0 & 0 & 0 \\
0 & 0 & 0 & 0 & 0 & 0 & 0 & -18.794 & 0 & 0 & 0 & 0 & 0 & 0 & 0 & 0 & -28.191 & 0 & 9.397 & 0 & 0 & 0 & 0 & 0 & 0 \\
0 & 0 & 0 & 0 & 0 & 0 & 0 & 0 & 0 & 0 & 0 & 0 & 0 & 0 & 0 & 0 & 0 & 0 & 0 & 0 & 0 & 0 & 0 & 0 \\
0 & 0 & 0 & 0 & 0 & 0 & 0 & 0 & -0.342 & -1 & -0.342 & 0 & 0 & 0 & 0 & 1.000 & 0 & 0 & 0 & 0 & -1 & 0.342 & 1.000 & 0.342 \\
0 & 0 & 0 & 0 & 0 & 0 & 0 & 0 & 0.940 & 0 & -0.940 & 0 & 0 & 0 & 0 & 0 & 0 & 0 & 0 & 0 & 0 & 0.940 & 0 & -0.940 \\
0 & 0 & 0 & 0 & 0 & 0 & 0 & 0 & -28.191 & 0 & 0 & 0 & 0 & 0 & 0 & 41.212 & 0 & 0 & 0 & 0 & 0 & 0 & 41.212 & 0 \\
0 & 0 & 0 & 0 & 0 & 0 & 0 & 0 & 0.342 & 1 & 0.342 & 0 & 0 & 0 & 0 & -1.000 & 0 & 0 & 0 & 0 & 1 & -0.342 & -1.000 & -0.342 \\
0 & 0 & 0 & 0 & 0 & 0 & 0 & 0 & 0 & 0 & 0 & 0 & 0 & 0 & 0 & 0 & 0 & 0 & 0 & 0 & 0 & 0 & 0 & 0 \\
0 & 0 & 0 & 0 & 0 & 0 & 0 & 0 & 0 & 0 & 0 & 0 & 0 & 0 & 0 & 0 & 0 & 0 & 0 & 0 & 0 & 0 & 0 & 0 \\
0 & 0 & 0 & 0 & 0 & 0 & 0 & 0 & 10.261 & 20 & 3.420 & 0 & 0 & 0 & 0 & -30.000 & 0 & 0 & 0 & 0 & 0 & -6.840 & -10.000 & 0 \\
0 & 0 & 0 & 0 & 0 & 0 & 0 & 0 & -0.9340 & 0 & 0.940 & 0 & 0 & 0 & 0 & 0 & 0 & 0 & 0 & 0 & 0 & -0.940 & 0 & 0.940 \\
0 & 0 & 0 & 0 & 0 & 0 & 0 & 0 & 0 & 0 & 0 & 0 & 0 & 0 & 0 & 0 & 0 & 0 & 0 & 0 & 0 & 0 & 0 & 0 \\
0 & 0 & 0 & 0 & 0 & 0 & 0 & 0 & 0 & 0 & 0 & 0 & 0 & 0 & 0 & 0 & 0 & 0 & 0 & 0 & 0 & 0 & 0 & 0 \\
0 & 0 & 0 & 0 & 0 & 0 & 0 & 0 & -28.191 & 0 & 9.397 & 0 & 0 & 0 & 0 & 0 & 0 & 0 & 0 & 0 & 0 & -18.794 & 0 & 0
\end{bmatrix}$$

The SVD of the Jacobian matrix was then calculated, which gives

$$\mathbf{v}_{diag} = \begin{bmatrix} 91.6169 \\ 73.9355 \\ 73.3750 \\ 52.2536 \\ 38.9967 \\ 34.6444 \\ 32.5559 \\ 29.3057 \\ 23.5099 \\ 22.4854 \\ 14.7911 \\ 11.0325 \\ 2.19116 \\ 1.74072 \\ 1.60164 \\ 1.52818 \\ 1.34030 \\ 1.22320 \\ 1.17221 \\ 0.27834 \\ 9.21621\times10^{-15} \\ 6.58045\times10^{-15} \\ 4.87285\times10^{-15} \\ 2.65515\times10^{-15} \end{bmatrix}, \quad \mathbf{W}_4 = \begin{bmatrix} 0.2462 & 0.1537 & 0.1045 & 0.0440 \\ -0.3958 & 0.0123 & 0.3697 & 0.0739 \\ -0.0410 & -0.1670 & -0.2593 & -0.1737 \\ -0.2043 & 0.0266 & 0.0828 & 0.3054 \\ -0.1807 & -0.1488 & -0.2027 & 0.0352 \\ 0.1085 & -0.0337 & 0.0607 & -0.4211 \\ 0.0410 & 0.1670 & 0.2593 & 0.1737 \\ 0.3000 & -0.0194 & -0.2263 & -0.1896 \\ 0.1531 & -0.3465 & -0.0429 & 0.1795 \\ -0.2854 & 0.0881 & -0.1734 & -0.0876 \\ -0.0384 & -0.3608 & 0.2441 & -0.0520 \\ -0.3117 & -0.1586 & -0.0064 & -0.1232 \\ 0.1342 & 0.3679 & -0.3876 & 0.1677 \\ 0.2854 & -0.0881 & 0.1734 & 0.0876 \\ -0.0574 & 0.3536 & -0.1006 & -0.0638 \\ -0.1807 & -0.1488 & -0.2027 & 0.0352 \\ -0.2043 & 0.0266 & 0.0828 & 0.3054 \\ -0.0410 & -0.1670 & -0.2593 & -0.1737 \\ -0.0127 & 0.0409 & -0.2042 & 0.5369 \\ 0.1152 & 0.1439 & 0.3008 & -0.1143 \\ 0.2462 & 0.1537 & 0.1045 & 0.0440 \\ -0.2489 & 0.3393 & 0.1863 & -0.2953 \\ 0.2854 & -0.0881 & 0.1734 & 0.0876 \\ -0.0574 & 0.3536 & -0.1006 & -0.0638 \end{bmatrix} \tag{A16}$$

where $\mathbf{v}_{diag}$ contains 24 values on its main diagonal of the rectangular matrix $\mathbf{V}$, arranged in descending order, and $\mathbf{W}_4$ comprises the last four columns of $\mathbf{W}$. The last four entries of $\mathbf{v}_{diag}$ are approximately zero in comparison with others, indicating that $\mathbf{M}^{II}$ is rank-deficient with nullity of four.

$\mathbf{W}_4$ contains four orthonormal column vectors. A general infinitesimal displacement mode, $\mathbf{p}$, can be described as the linear combination of these four vectors, i.e.,

$$\mathbf{p} = \mathbf{W}_4\mathbf{c} \tag{A17}$$

where $\mathbf{c}$ is a vector containing four arbitrary coefficients.

Now we try to isolate the motion in which all elements possess the same form, i.e.,

$$\theta_{A1} = \theta_{A3} = -\theta_{A5} = -\theta_{A7},\ \theta_{A2} = \theta_{A4} = -\theta_{A6} = -\theta_{A8}$$
$$\theta_{Ai} = \theta_{Hi} = \theta_{Fi} = \theta_{Gi}\ (i = 1,\ 2,\ ...,\ 8) \tag{A18}$$

We choose

$\mathbf{p}$ = [-0.0934, 0.2731, -0.0934, 0.2731, 0.0934, -0.2731, 0.0934, -0.2731, 0.2731, -0.0934, 0.2731, 0.0934, -0.2731, 0.0934, -0.2731, 0.0934, 0.2731, -0.0934, 0.2731, -0.0934, -0.0934, -0.2731, 0.0934, -0.2731]^{T}

with $\mathbf{c} = \left[-0.2689,\ -0.5987,\ 0.3357,\ 0.6757\right]^{T}$.

We then re-orthogonalise the subspace that was described by $\mathbf{W}_4$ by the Gram-Schmidt orthogonalisation (Chen, 2021) with $\mathbf{p}$ as a basis, four orthonormal column vectors can be obtained as

$$\mathbf{W}_{4,re} = \begin{bmatrix} -0.0934 & 0.2211 & 0.1362 & 0.0663 \\ 0.2731 & -0.3224 & 0.1198 & 0.2671 \\ -0.0934 & -0.0661 & -0.2344 & -0.1387 \\ 0.2731 & -0.1308 & 0.1674 & -0.0553 \\ 0.0934 & -0.1556 & -0.1199 & -0.1766 \\ -0.2731 & 0.0350 & -0.1912 & 0.2165 \\ 0.0934 & 0.0661 & 0.2344 & 0.1387 \\ -0.2731 & 0.2266 & -0.1436 & -0.1059 \\ 0.2731 & 0.2266 & -0.1436 & -0.1059 \\ -0.0934 & -0.3106 & -0.0217 & -0.1041 \\ 0.2731 & 0.0350 & -0.1912 & 0.2165 \\ 0.0934 & -0.2866 & -0.1524 & 0.0440 \\ -0.2731 & 0.0607 & 0.2150 & -0.3777 \\ 0.0934 & 0.3106 & 0.0217 & 0.1041 \\ -0.2731 & -0.1308 & 0.1674 & -0.0553 \\ 0.0934 & -0.1556 & -0.1199 & -0.1766 \\ 0.2731 & -0.1308 & 0.1674 & -0.0553 \\ -0.0934 & -0.0661 & -0.2344 & -0.1387 \\ 0.2731 & 0.0607 & 0.2150 & -0.3777 \\ -0.0934 & 0.0901 & 0.1036 & 0.2868 \\ -0.0934 & 0.2211 & 0.1362 & 0.0663 \\ -0.2731 & -0.3224 & 0.1198 & 0.2671 \\ 0.0934 & 0.3106 & 0.0217 & 0.1041 \\ -0.2731 & -0.1308 & 0.1674 & -0.0553 \end{bmatrix} \quad \text{(A19)}$$

Next, we carried out the corrector step for each possible motion, and it is apparent that only the motion along **p**, which is the first column of $\mathbf{W}_{4,re}$, leads to a finite mechanism.

We then deploy unit II with an angle increment of 0.01 rad. The Jacobian matrix $\mathbf{M}^{II}$ is constructed for subsequent configurations. It is found that *r*, the rank of the Jacobian matrix $\mathbf{M}^{II}$, is 23, indicating that unit II is a single-DoF mechanism. This enables us to plot the motion curve in Figure 5.6 of the main paper.

At the fully deployed state, the Jacobian matrix $\mathbf{M}^{II}$ is again rank-deficient with nullity of four. Using the same approach, we find that only one motion is finite, whereas the other three are infinitesimal.

REFERENCES

Adhikari, S. & Phani, A. S., 2007. Rayleigh's classical damping revisited, In *International Conference on Civil Engineering in the New Millennium: Opportunities and Challenges*.

Afrati, F., 1994. The Hamilton circuit problem on grids. *RAIRO-Theoretical Informatics and Applications*, 28(6), pp. 567-582.

Altmann, S. L., 1986. *Rotations, quaternions, and double groups*. Oxford: Oxford University Press.

Armstrong, M. A., 2013. *Basic topology*. Springer Science & Business Media.

Arya, M., Lee, N. & Pellegrino, S., 2015. Wrapping thick membranes with slipping folds. In *2nd AIAA Spacecraft Structures Conference*, Kissimmee, FL.

Ball, R. S., 1876. The theory of screws: A study in the dynamics of a rigid body *Mathematische Annalen*, 9(4), pp. 541-553.

Beggs, J. S., 1966. *Advanced mechanism*. New York: Macmillan Company.

Blackwell, W., Allen, G., Galbraith, C., Hancock, T., Leslie, R., Osaretin, I., ... & Erickson, N., 2012. Nanosatellites for earth environmental monitoring: The MicroMAS project. In *2012 12th Specialist Meeting on Microwave Radiometry and Remote Sensing of the Environment (MicroRad)*, IEEE, pp. 1-4.

Bogacki, P. & Shampine, L. F., 1989. A 3(2) pair of Runge-Kutta formulas. *Appied. Mathematics Letters*, 2(4), pp. 321–325.

Calladine, C. R. & Pellegrino, S., 1991. First-order infinitesimal mechanisms. *International Journal of Solids and Structures*, 27(4), pp. 505-515.

Cara, F. J., Juan, J., Alarcón, E., Reynders, E., & De Roeck, G., 2013. Modal contribution and state space order selection in operational modal analysis. *Mechanical Systems and Signal Processing*, 38(2), pp. 276-298.

Chen, M., 2021. "Gram-Schmidt orthogonalization", *MATLAB Central File Exchange*. [Online] Available at: https://www.mathworks.com/matlabcentral/fileexchange/55881-gram-schmidt-orthogonalization [Accessed 26 12 2021].

Chen, Y., Peng, R. & You, Z., 2015. Origami of thick panels. *Science*, 349(6246), pp. 396-400.

Coleman, T. F. & Li, Y., 1994. On the convergence of interior-reflective Newton methods for nonlinear minimization subject to bounds. *Mathematical Programming*, 67(1), pp. 189–224.

Conway, J. H., Burgiel, H. & Goodman-Strauss, C., 2016. *The symmetries of things*. CRC Press.

Coxeter, H. S. M., 1973. *Regular Polytopes*. New York: Dover Publications.

Craig, J. J., 1986. *Introduction to Robotics: Mechanics and Control*. Boston: Addison-Wesley Longman Publishing Co., Inc.

Danielson, G. H., 1968. On finding simple paths and circuits in a graph. *IEEE transactions on circuit theory*, 15(3), pp. 294-295.

Davies, T. H., 1981. Kirchhoff's circulation law applied to multi-loop kinematic chains. *Mechanism and Machine Theory*, 16(3), pp. 171–183.

Dawson, S., Stella, P., McAlpine, W. & Smith, B., 2012. JUNO Photovoltaic Power at Jupiter. In *10th International Energy Conversion Engineering Conference* Atlanta, Georgi, pp. 3833.

De Temmerman, N., Mollaert, M., Van Mele, T. & De Laet, L., 2007. Design and analysis of a foldable mobile shelter system. *International Journal of Space Structures*, 22(3), pp. 161–168.

Hartenberg, R. S., & Denavit, J., 1964. *Kinematic Synthesis of Linkages*. New York: McGraw-Hill.

Edmondson, B. Lang, R. J., Morgan, M. R., Magleby, S. P., & Howell, L. L. 2015. Thick rigidly foldable structures realized by an offset panel technique. *Origami6: I. Mathematics*, 149. Tokyo, Japan.

Ericson, C., 2004. *Real-time collision detection*. CRC Press.

Featherstone, R., 2008. *Rigid body dynamics algorithms*. Canberra, Australia: Springer.

Fowler, P. W., Guest, S. D., & Schulze, B., 2016. Mobility of a class of perforated polyhedra. *International Journal of Solids and Structures,* 85, 105-113.

Fuehrer, C. & Leimkuhler, B. J., 1991. Numerical solution of differential-algebraic equations for constrained mechanical motion. *Numerische Mathematik*, 59(1), pp. 55–69.

Gan, W. W. & Pellegrino, S., 2006. A numerical approach to the kinematic analysis of deployable structures forming a closed loop. *Proceedings of the Institution of Mechanical Engineers, Part C: Journal of Mechanical Engineering Science*, 220(7), pp. 1045-1056.

Garey, M. R. & Johnson, D. S., 1979. *Computers and intractability: a guide to the theory of NP-completeness*. New York: W.H. Freeman.

Gartung, N. I., 2018. Approaches for the calculation Of Rayleigh damping coefficients for a time-history analysis. In *Structures Under Shock and Impact XV*, Vol. 180, pp. 227-237.

Gdoutos, E., Truong, A., Pedivellano, A., Royer, F., & Pellegrino, S., 2020. Ultralight deployable space structure prototype. In *AIAA Scitech Forum*, pp. 0692.

Gilbert, E. G., Johnson, D. W. & Keerthi, S. S., 1988. A fast procedure for computing the distance between complex objects in three-dimensional space. *IEEE Journal of Robotics and Automation*, 4(2).

Goldstein, H., 1951. *Classical mechanics*. Addison-Wesley.

Gordon, V. S., Orlovich, Y. L. & Werner, F., 2008. Hamiltonian properties of triangular grid graphs. *Discrete Mathematics*, 308(24), pp. 6166-6188.

Greene, C., 2021. “Butterworth Filters”, *MATLAB Central File Exchange*. [Online] Available at: https://www.mathworks.com/matlabcentral/fileexchange/38584-butterworth-filters [Accessed 14 12 2021].

Grünbaum, B. & Shephard, G. C., 1986. *Tilings and patterns*. WH Freeman & Co.

Guest, S. G. & Pellegrino, S., 1996. A new concept for solid surface deployable antennas. *Acta Astronautica*, 38(2), pp. 103-113.

Guest, S. & Pellegrino, S., 1992. Inextensional wrapping of flat membranes. In *Proceedings of the first international seminar on structural morphology*, Montpellie, pp. 203–215.

Hamilton, W. R., 1856. Letter to John T. Graves on the Icosian. In *The Mathematical Papers of Sir William Rowan Hamilton.* Cambridge University Press, 1931, H. Halberstam and R.E. Ingram, Vol. 3 (Algebra).

Hoberman, C., 2010. Folding structures made of thick hinged sheets. *US, Patent No. 7,794,019.*

Hoberman, C. S., 1988. Reversibly expandable three-dimensional structure. United States, *Patent No. US4780344A.*

Howell, L. L., 2001. *Compliant mechanisms*. New York: Wiley-Interscience Publication.

Hunt, K. H., 1978. *Kinematic geometry of mechanisms*. Oxford: Oxford University Press.

Ionescu, T. G., Antonescu, P., Biro, I., Bögelsack, G., & Klein Breteler, AJ., 2003. Terminology for mechanisms and machine science. *Mechanism and Machine Theory*, 38(7), pp. 597-901.

Islam, K., Meijer, H., Rodríguez, Y. N., Rappaport, D., & Xiao, H., 2007. Hamilton circuits in hexagonal grid graphs. In *CCCG*, Ottawa, pp. 85-88.

Itai, A., Christos, H. P. & Jayme, L. S., 1982. Hamilton paths in grid graphs. *SIAM Journal on Computing*, 11(4), pp. 676-686.

Ku, J. S. & Demaine, E. D., 2016. Folding flat crease patterns with thick materials. *Journal of Mechanisms and Robotics*, 8(3).

Kumar, P. & Pellegrino, S., 2000. Computation of kinematic paths and bifurcation points. *International Journal of Solids and Structures*, Vol. 37, pp. 7003-7027.

Kwak, M. K., Heo, S. & Kim, H. B., 2008. Dynamics of satellite with deployable rigid solar arrays. *Multibody System Dynamics*, pp. 271–286.

Lang, R. J., Nelson, T. G., Magleby, S. P. & Howell, L. L., 2016. Thick rigidly foldable origami mechanisms based on synchronized offset rolling contact elements. In *International Design Engineering Technical Conferences and Computers and Information in Engineering Conference*.

Lang, R. J., Tolman, K. A., Crampton, E. B., Magleby, S. P., & Howell, L. L., 2018. A Review of Thickness-accommodation techniques in origami-inspired engineering. *Applied Mechanics Reviews*, 70(1).

Li, J., Yan, S., Guo, F. & P, G., 2013. Effects of damping, friction, gravity, and flexibility on the dynamic performance of a deployable mechanism with clearance. *Proceedings of the Institution of Mechanical Engineers, Part C: Journal of Mechanical Engineering Science*, 227(8), pp. 1791-1803.

Li, Y., 2020. Motion paths finding for multi-degree-of-freedom mechanisms. *International Journal of Mechanical Sciences*, Vol. 185.

Li, Y. et al., 2021. Parameter optimization for torsion spring of deployable solar array system with multiple clearance joints considering rigid-flexible coupling dynamics. *Chinese Journal of Aeronautics*, 35(3), pp. 509-524.

Ljung, L., 1988. "System identification toolbox", *The MATLAB User's Guide*.

MathWorks, R2019b. MATLAB optimization toolbox - fmincon. [Online] Available at: https://uk.mathworks.com/help/optim/ug/fmincon.html#Reference
[Accessed 15 Feb 2020].

MathWorks, R2019b. Simscape - MATLAB & Simulink. [Online] Available at: https://uk.mathworks.com/products/simscape.html [Accessed 06 Mar 2020].

McCarthy, J. M., 1990. *An introduction to theoretical kinematics*. Cambridge, MA, MIT Press.

McGill, D. J. & King, W. W., 1995. *Engineering mechanics, an introduction to dynamics*. 3rd ed., PWS Publishing Company.

McMaster-Carr, 1994. *McMaster-Carr torsion springs.* [Online] Available at: https://www1.mcmaster.com/torsion-springs/ [Accessed 8 May 2021].

Miller, S., 2020. Simscape multibody multiphysics library. [Online] Available at: https://www.mathworks.com/matlabcentral/fileexchange/37636-simscape-multibody-multiphysics-library [Accessed 10 01 2020].

Morgan, J., Magleby, S. P., & Howell, L. L., 2016. An approach to designing origami-adapted aerospace mechanisms. *Journal of Mechanical Design*, 138(5).

Müller, A., 2018. Kinematic topology and constraints of multi-loop linkages. *Robotica*, Vol. 36, pp. 1641–1663.

Murphy, D., 2012. Megaflex - the scaling potential of ultraflex technology. In *53rd AIAA/ASME/ASCE/AHS/ASC Structures, Structural Dynamics and Materials Conference* Honolulu, Hawaii, pp. 1581.

Nikravesh, P. E., 2008. Newtonian-based methodologies in multi-body dynamics. *Proceedings of the Institution of Mechanical Engineers, Part K: Journal of Multi-Body Dynamics*, 222(4), pp. 277–288.

Nishiyama, Y., 2012. Miura folding: applying origami to space exploration. *International Journal of Pure and Applied Mathematics*, 79(2), pp. 269-279.

Overschee, P. V. & Moor, B. D., 1994. N4SID: Subspace algorithms for the identification of combined deterministic-stochastic systems. *Automatica*, 30(1), pp. 75-93.

Pellegrino, S., 1986. *Mechanics of kinematically indeterminate structures*. Doctoral dissertation, University of Cambridge.

Pellegrino, S. & Calladane, C. R., 1986. Matrix analysis of statically and kinematically indeterminate frameworks. *International Journal of Solids Structures*, 22(4), pp. 409 - 428.

Polishchuk, V., Arkin, E. & Mitchel, J., 2006. Hamiltonian cycles in triangular grids. In *CCCG*, Ontario, p. 63–66.

Reynders, E., 2012. System identification methods for (operational) modal analysis: review and comparison. *Archives of Computational Methods in Engineering*, 19(1), pp. 51-124.

Rubin, F., 1974. A search procedure for Hamilton paths and circuits. *Journal of the ACM*, 21(4), pp. 576-580.

Santoni, F., 2015. Dynamics of spring-deployed solar panels for agile nanospacecraft. *Journal of Aerospace Engineering*, 28(5).

Santoni, F. et al., 2014. An innovative deployable solar panel system for CubeSats. *Acta Astronautica*, Vol. 95, pp. 210-217.

Sareh, P., & Guest, S. D., 2015. Design of isomorphic symmetric descendants of the Miura-ori. *Smart Materials and Structures*, 24(8), pp. 085001.

Schenk, M., Viquerat, A. D., Seffen, K. A., & Guest, S. D., 2014. Review of inflatable booms for deployable space structures: packing and rigidization. *Journal of Spacecraft and Rockets*, 51(3), pp. 762-778.

Seffen, K. A. & Pellegrino, S., 1999. Deployment dynamics of tape springs. *Proceedings of the Royal Society of London. Series A: Mathematical, Physical and Engineering Sciences*, 455(1983), pp. 1003-1048.

Shabana, A., 2013. *Dynamics of multibody systems*. Cambridge: Cambridge University Press.

Shampine, L. F. & Reichelt, M. W., 1997. The MATLAB ODE Suite. *SIAM Journal on Scientific Computing*, Vol. 18, pp. 1–22.

Sharma, M., 2021. "Print all Hamiltonian cycles in an undirected Graph", *GeeksforGeeks*. [Online] Available at: https://www.geeksforgeeks.org/print-all-hamiltonian-cycles-in-an-undirected-graph/ [Accessed 25 02 2022].

Spong, M. W., Hutchinson, S. & Vidyasagar, M., 2004. *Robot dynamics and contro*l, Wiley.

Wall, M., 2018. Scientific American. [Online] Available at: https://www.scientificamerican.com/article/nasas-insight-mars-lander-snaps-selfie-surveys-workspace/ [Accessed 15 January 2021].

Wang, C., Li, J. & You, Z., 2018. A Kirigami-inspired foldable model for thick panels, *The 7th international meeting on origami in science, mathematics and education (7OSME),* Oxford

Wang, J., Gosselin, C. M. & Cheng, L., 2002. Modeling and simulation of robotic systems with closed kinematic chains using the virtual spring approach. *Multibody System Dynamics*, Vol. 7, pp. 145–170.

Watt, A. M. & Pellegrino, S., 2004. *Rigid deployable solar array*, Cambridge: University of Cambridge.

Yang, J., 2022. Measurement of spring stiffness and damping. Mendeley Data.

Yang, J. & You, Z., 2019. Compactly folding rigid panels with uniform thickness through origami and kirigami. In *International Design Engineering Technical Conferences and Computers and Information in Engineering Conference,* Anaheim, CA., Vol. 59247, pp. V05BT07A042.

Yang, J., Zhang, X., Chen, Y. & You, Z., 2022a. Folding arrays of uniform-thickness panels to compact bundles with a single degree of freedom. *Proceedings of the Royal Society A*, 478(2261).

Yang, J., Zhang, Y., Chatzis, M. N. & You, Z., 2022b. Folding and deploying identical thick panels with spring-loaded hinges. *Extreme Mechanics Letters*, Vol. 52, pp. 101637.

Yang, J., Zhang, Y., Chatzis, M. N., and You, Z., 2022c. Data for "folding and deploying identical thick panels with spring-loaded hinges". *Data in Brief*, p.108388.

Yoshimura, Y., 1955. On the mechanism of buckling of a circular cylindrical shell under axial compression, Washington, DC, United States: National Advisory Committee for Aeronautics.

You, Z. & Chen, Y., 2011. *Motion structures: deployable structural assemblies of mechanisms*. Oxford: CRC Press.

Zhang, X. & Chen, Y., 2018. The diamond thick-panel origami and the corresponding mobile assemblies of plane-symmetric Bricard linkages. *Mechanism and Machine Theory*, Vol. 130, pp. 585-604.

Zirbel, S. A. et al., 2013. Accommodating thickness in origami-based deployable arrays. *Journal of Mechanical Design*, 135(11), pp. 111005.